UNIVERSITY OF OKLAHOMA

GRADUATE COLLEGE

MOISTURE SURGES OVER THE GULF OF CALIFORNIA AND RELATIONSHIPS WITH CONVECTIVE ACTIVITY

A DISSERTATION
SUBMITTED TO THE GRADUATE FACULTY
in partial fulfillment of the requirements for the
Degree of
DOCTOR OF PHILOSOPHY

By
JOHN FREDY MEJIA-VALENCIA
Norman, Oklahoma
2008

MOISTURE SURGES OVER THE GULF OF CALIFORNIA AND RELATIONSHIPS WITH CONVECTIVE ACTIVITY

A DISSERTATION APPROVED FOR THE
SCHOOL OF METEOROLOGY

BY

Dr. Peter Lamb, Chair

Dr. Michael Douglas

Dr. Lance Leslie

Dr. Michael Richman

Dr. Randall Kolar

Acknowledgement

This research and the North American Monsoon Experiment-2004 was sponsored by the NOAA/Climate Program Office.

I would like to thank my advisors, Michael Douglas and Peter Lamb, for their guidance and help on any aspects of this work. Their support and encouragement, and time investment are very much appreciated.

I also thank my committee members Lance Leslie, Michael Richman, and Randall Kolar for their insightful comments and suggestions. Many people provided technical advice and support throughout this project. Useful discussions with Joseph Zehnder of Creighton University and David Gochis of National Center for Atmospheric Resaearch also are greatly appreciated.

Most North American Monsoon Experiment data sets used in this study were provided by NCAR/EOL. Analysis products from FNL and some upper-air and surface data were made available by NCAR/Scientific Computing Division, through a project for data access. Some of the computing for this research was performed at the OU Supercomputing Center for Education & Research (OSCER), a division of University of Oklahoma Information Technology Center. We gratefully acknowledge the assistance of the WRF help desk and OSCER staff, which made part of this research possible. Ken Knapp of NESDIS made the historical GOES imagery available for this work.

Finally, I am most thankful and deeply indebted to my family for their constant and patient support and for instilling in me this love and appreciation of learning. I would also like to thank Diana Vargas and all my friends for their constant encouragement and emotional support. You were always there to help me along during difficult moments. You all encouraged me to complete this work and many others I have endeavored.

Table of Content

List of Acronyms

ADV:	Advection term
ARW:	Advance Research WRF
ASL:	Above sea level
AZ:	Arizona
C1, C2:	Convective schemes
CAPE:	Convective Available Potential Energy
CB:	Cold Bubble
CHI200:	Velocity Potential at 200 hPa
CO:	Coriolis term
CP:	GoC Coastal Plains
CPC:	Climate Prediction Center
CTD:	Coastal Trapped Disturbances
EEOF:	Extended Empirical Orthogonal Funcion
ENSO:	El Nino-Southern Oscillation
EOP:	Extended Observation Period
EPAC:	Eastern Pacific
FNL:	NCEP Final Analyses
GCLLJ:	Gulf of California Low-level Jet
GE:	Gulf of California Entrance
GoC:	Gulf of California
GOES:	Geostationary Operational Environmental Satellites
GoM:	Gulf of Mexico
IOP:	Intensive Observation Period
ISCCP:	International Satellite Cloud Climatology Project
LKW:	Linear Kelvin Wave
LLJ:	Low-level Jet
LSM:	Land-Surface Model
LT:	Local Time
LTC:	Local Time Derivative
LW:	Longwave Radiation Model
MBL:	Marine Boundary Layer
MCS:	Mesoscale Convective System
MJO:	Madden-Julian Oscillation
MM5:	NCAR/ Pennsylvania State University Mesoscale Model 5
NAM:	North American Monsoon
NAMAP:	North American Modeling Assessment Project
NAME:	North American Monsoon Experiment
NAMS:	North American Monsoon System
NARR:	North American Regional Reanalysis
NASA:	National Aeronautics and Space Administration
NCDC:	National Climatic Data Center
NCEP:	National Centers for Environmental Prediction
NCAR:	National Center for Atmospheric Research

NERN:	NAME Event Raingage Network
NM:	New Mexico
NOAA:	National Oceanic and Atmospheric Administration
NPO:	North Pacific Oscillation
OLR:	Outgoing Longwave Radiation
PBL:	Planetary Boundary Layer
PC:	Principal Component
PGF:	Pressure Gradient Force
Qflux:	Moisture Flux
QuikSCAT:	Microwave scatterometer SeaWind data
RAOBS:	Radiosonde Observations
RK:	Runge-Kutta
SKW:	Solitary Kelvin Wave
SL:	Surface Layer Model
SLPA:	Sea Level Pressure Anomaly
SMO:	Sierra Madre Occidental
SW:	Short Wave Radiation Model
SWAMP:	Southwest Area Monsoon Project
TA:	Temperature Anomaly
TC:	Tropical Cyclone
TdA:	Dew Point Temperature Anomaly
TEW:	Tropical Easterly Wave
TRMM:	Tropical Rainfall Measurement Mission
TS:	Tropical Storm
UTC:	Coordinated Universal Time
WP-3D:	NOAA Weather Patrol – 3D research aircraft
WRF:	Weather Research and Forecasting Model

List of Figures

List of Tables

Abstract

The North American Monsoon (NAM) is characterized by widespread convective activity and rainfall that is tied to key synoptic and sub-synoptic atmospheric circulation features during summer - from mid-June to September. The core monsoon region, particularly over southwestern United States and around the Gulf of California (GoC), often experiences atmospheric phenomena recognized in the literature as "moisture surges". These moisture surges represent one of the most important sources of rainfall variability in the NAM core region with important implications in the hydroclimate and the water resources management in this semiarid region. Although there are a number of studies relating NAM synoptic-scale conditions with moisture surges and regional rainfall patterns, the interactions between atmospheric phenomena of differing scales still remains under-investigated.

The overall objective of this research is to improve the understanding of how smaller-spatial scale atmospheric processes modify the evolution of larger-scale atmospheric conditions over the NAM domain. More specifically, this study aims to determine the relationship between organized mesoscale convective systems (MCSs) and moisture surges, and their associated synoptic forcings in the form of Tropical Easterly Waves (TEW), and eastern Pacific Tropical Storms (TS)/Tropical Cyclones (TC). Similarly, relationships were determined between MCSs and GoC low-level jet (GCLLJ).

The present research uses three approaches to determine the links between MCSs and moisture surges. A first component of the research consisted of a detailed analyses of a well-observed moisture surge event that occurred during the North American Monsoon Experiment (NAME-2004). Analyses of aircraft flight-level data, together with other special and routine observations are used to describe the four-dimensional structure of this surge event. Theory and observations indicate that this surge's leading edge resembles a solitary Kelvin wave during its initial stages. MCS convective outflows in the central-GoC were observed to modify northern GoC surge variability and the GCLLJ

intensity. The observations highlighted the role of convective activity in modulating the surge and its subsequent evolution.

The second component of this research consists of a comprehensive climatological study using historical satellite-estimated MCSs, a multiyear set of surge events, the North American Regional Reanalysis (NARR) products, and microwave scatterometer SeaWinds (QuikSCAT) data. Climatological composites are created based on synoptic timescales features (such as TEWs and TSs/TCs) and intraseasonal variations (30-60 -day Madden-Julian Oscillation (MJO) variability), and are further stratified with respect to mesoscale rainfall variability in the NAMS core region. These results provided new insights into the nature of the GoC moisture flux variability and describe the influence of MCSs in modulating the intensity of moisture surges and the GCLLJ. Further, results revealed the role of MCSs in modulating the diurnal cycle of the GoC low-level circulation during “major surge”, “minor surge”, and “non-surge” environments.

In the third and final component of this research, numerical simulation experiments were performed using the Advance Research Weather and Research Forecasting (ARW V3.0) model to investigate the sensitivity of the model to those physical representations associated with convective processes in surge and non-surge synoptic-scale environments. The approach consisted of simulating features associated with mesoscale convective processes on different synoptic-scale background flows (e.g. during moisture surge and non-surge conditions). In the interest of simplicity, convective outflows, typically resulting from MCS events, were replaced by Cold Bubbles (CBs). Although several assumptions were made to replace the effect of convective activity by those of the CBs, this model configuration permitted evaluating the impact that CBs have on the regional flow during surge and non-surge conditions. The influence of CBs over the central-GoC coastal plains was found to be more pronounced for non-surge than for surge synoptic conditions. In particular, the GCLLJ variability and its intensity were larger when CBs were inserted. However, significant southeasterly low-level flow over the northern-GoC was mainly associated with those CBs inserted during the daytime.

Taken together, this research shows important associations between MCSs and moisture surges. Surges appear to modify the diurnal circulations along the GoC coastal plain, partly through MCS activity, which in turn enhances the offshore flow along the eastern GoC coast, which then enhances the nocturnal low-level jet over the northern GoC. Furthermore, the occurrence of MCSs over the southern GoC immediately before surge onset produces more intense moisture surges, regardless of the type of tropical synoptic-scale disturbance that is forcing the surge. Therefore, the correct simulation of MCSs (their timing and intensity) in the NAM core region has an upscale effect on the correct simulation of the GoC low-level flow with significant impact on the transient components of the NAMS.

1 INTRODUCTION

1.1 Overview and Problem Statement

1.1.1 Background

The North American Monsoon (NAM) is characterized by large-scale convective activity and rainfall that is tied to key synoptic and sub-synoptic atmospheric circulation features during summer from mid-June to September. The NAM is smaller in scale than monsoons in other regions of the world (e.g., Indian Monsoon or the West African Monsoon) and is perhaps the least understood large-scale circulation pattern during the North America warm season, hence its limited climate prediction skill (Gutzler et al., 2005). The NAM accounts for as much as 70% of the annual rainfall in northwestern Mexico (Douglas et al., 1993) and nearly 50% in some parts of the southwestern United States (Adams and Comrie, 1997). These rainfall amounts, typically starting in mid-June and lasting until mid-September (Figure 1), are accompanied by a seasonal reversal of low-level winds over the northern Gulf of California (GoC), where the wind reverses from northwesterly to southeasterly after the monsoon onset, and at mid-levels over Mexico, where the wind reverses from westerly to easterly. Although this circulation does not meet Ramage's (1971) monsoon definition, they have been considered as a monsoonal region by many other authors (Krishnamurti, 1971; Tang, and Reiter, 1984; Douglas et al., 1993). The challenge of forecasting rainfall and wind fields from seasonal to intraseasonal time scales inside the North American Monsoon System (NAMS) domain relies on the correct simulation not only on the continental-to-synoptic scales but also of the associated mesoscale atmospheric circulation features (Gutzler et al., 2005). This is especially difficult in the "core monsoon" region (see Figure 2) including the southwestern United States and northwestern Mexico, where relatively few observations, large diurnal cycles, complex orography, and coastal geometry restrict the depiction of the monsoon evolution and make its simulation difficult. This special geography configuration (Figure 2), which includes the Sierra Madre Occidental oriented NW-SE, the relatively shorter mountains in the Baja California peninsula and the narrow channel of relatively warmer sea surface temperatures of the GoC, creates interesting mesoscale

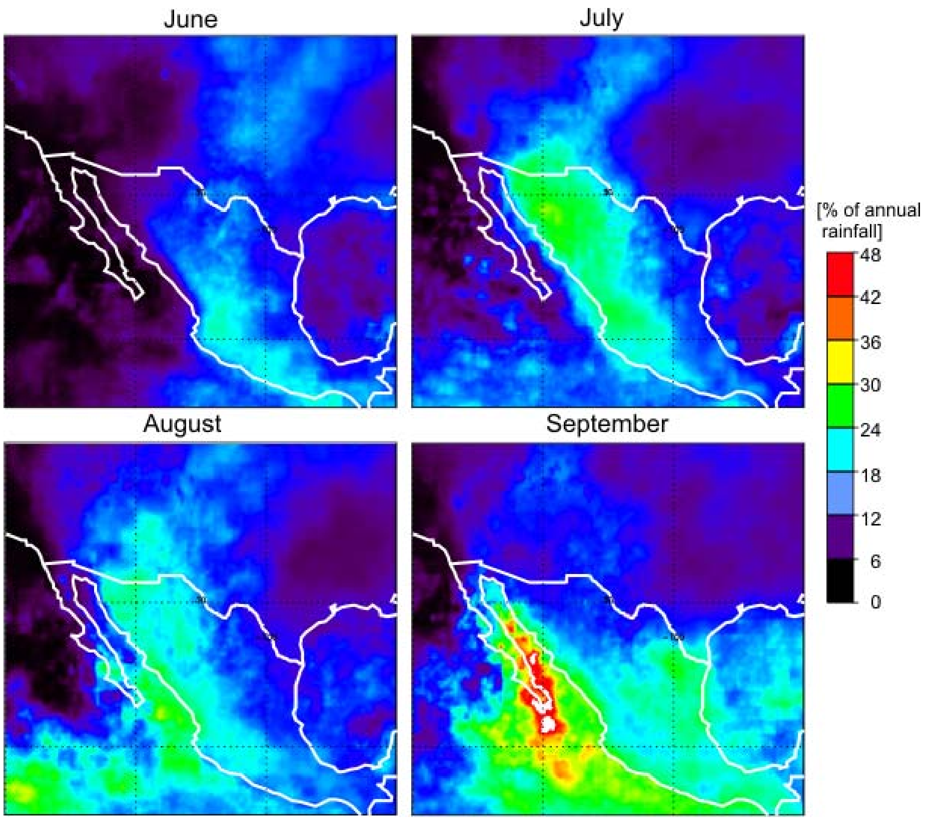

Figure 1. 3B43 TRMM monthly mean rainfall as a percentage of annual mean rainfall for June-September (1998-2007). 0.25° × 0.25° longitude – latitude grid.

structures in the low-level flow and rainfall patterns that limits a clear-cut relationship between the various atmospheric circulation scales associated with the NAM.

The core monsoon region, particularly within the GoC basin, often experiences an atmospheric phenomenon recognized in the literature as the "Gulf Surge" or a "Moisture Surge." Moisture surges are mainly characterized as synoptic timescale variations in the low-level flow within the GoC, often spanning from 2-3 days, with a pronounced increase of southeasterly winds, a temperature drop, and moisture and sea level pressure rise. For example, Figure 3 shows these synoptic timescale variations associated with the moisture surge that occurred during July 2004, from Yuma, AZ, surface station observations. Normally, pre-surge conditions are characterized by relatively warm and dry low-level environments also associated with weak southeasterly winds or northerly wind anomalies. As shown in Figure 3, these pre-surge conditions could be suddenly interrupted by the onset of stronger southeasterly winds and cooler, moister conditions. These surges represent an important component of the transient variability of the atmospheric circulation and convection of the NAMS (Hales, 1972; Brenner, 1974; Adams and Comrie, 1998; Higgins et al., 2004). Furthermore, mesoscale simulations suggest that the role of transient flow in transporting moisture into the NAMS core region is as important as the time mean flow (Berbery, 2001). These considerations imply that a better understanding of the rainfall variability of the NAMS and its correct simulation requires improved documentation and knowledge of moisture surges. Thus, there is a need for understanding the key processes tied to surges such as their synoptic forcing, propagation mechanism(s), diurnal variability, and the possible interaction of these processes. Although a reasonable amount of research has been carried out on each of these topics, some areas are not well-understood; the remainder of this introduction documents and summarizes current understanding and the remaining under-investigated topics.

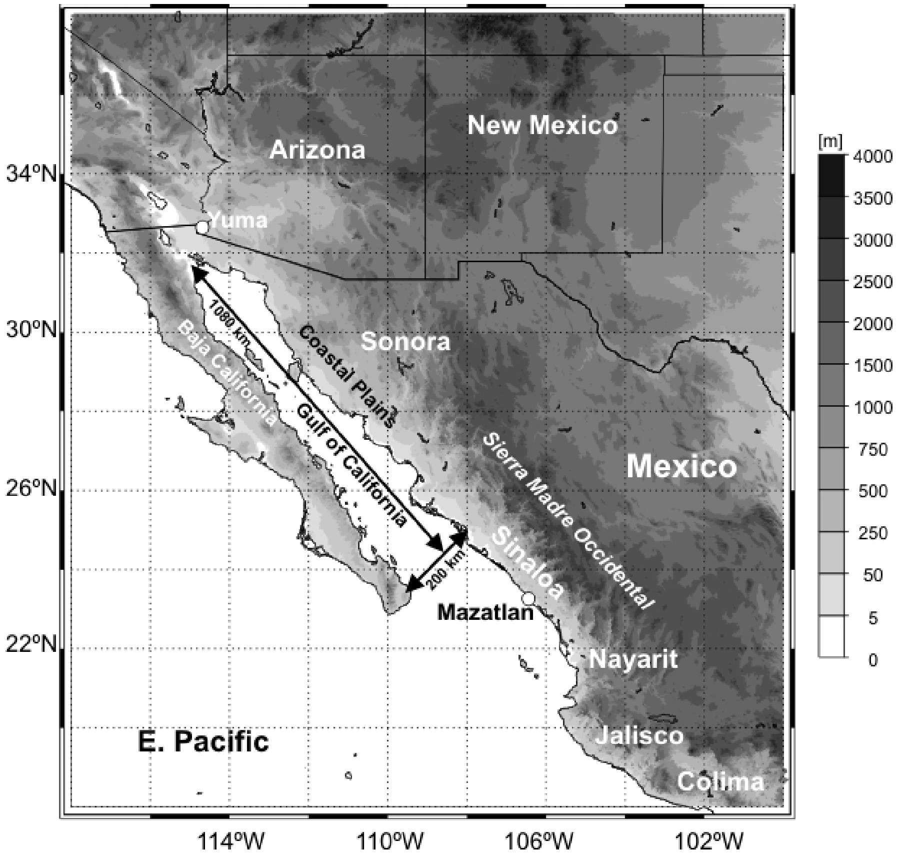

Figure 2. NAMS Core domain and topography. Darker colors represent higher elevations. Sierra Madre Occidental (SMO) averages 3000 m above sea level.

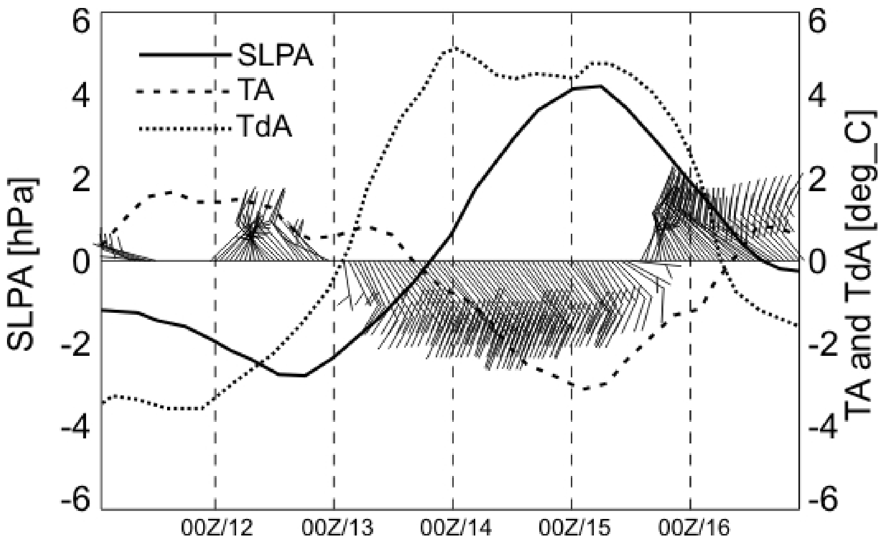

Figure 3. Example of moisture surge event at the Yuma, AZ surface station (32.65ºN, 114.6ºW, 63 m ASL) in July 2004. Anomaly traces are shown for sea-level pressure (SLPA, solid line, left ordinate), temperature (TA, dashed line, right ordinate), dew point temperature (TdA, dotted line, right ordinate), and wind vector (half a barb indicates an anomaly wind speed of 1 knot, while the staff shows anomaly wind direction) with hourly sampling frequency. Anomalies are calculated with respect to mean quantities for July 7 to 18 after filtering high frequency variability using a running 24-hr mean average. Abscissa is labeled in hour/day. Surge onset occurred on July 12 1500UTC.

Because of the sparseness of upper air data in NW Mexico and the low-level nature of the moisture surge phenomenon, such surges have often been defined by their signature at the surface meteorological stations that provide the most reliable and high-frequency observations in the GoC region. For example, several studies (Stensrud at al., 1997; Fuller and Stensrud, 2000; Higgins et al., 2004; Higgins and Shi, 2005) used observations from Yuma, AZ, to identify surges affecting the SW United States. On the other hand, Douglas and Leal (2003) stratified moisture surges into composites using historical 12-hourly rawinsonde data (1980-88) from Empalme, Mexico (SMN-CNA station, located on the central Gulf coastal plain, Figure 1) to document the surge's evolution and vertical structure. Although their surge identification procedure involved some complications, such as the coarse time resolution, possible local effects associated with convective outflows, and relatively strong diurnal changes in the boundary layer, their index proved adequate to discriminate well-marked long lasting surges, typically those associated with tropical synoptic disturbances. Recently, Bordoni and Stevens (2006) created a surge index based on the leading Principal Component of daily QuikSCAT wind observations (0.25º latitude/longitude grid scale ocean surface winds at

10m height), which accounted for about 50% of the seasonal variability, for 6 monsoon seasons. This data set only permits a day-to-day variability analysis; however, it constitutes a source of independent observations over the Gulf with the diurnal cycle eliminated. In general, Bordoni and Stevens's surge index represent reasonable well some of the major characteristic of moisture surges. However, their methodology relies on the selection of the unrotated leading PC to compose their index. Although their leading PC seems to represent well the original variable, the use of a relatively smaller size of the domain for PC determination, centered in the surge onset region, and also implementing a rotated PC approach as proposed by Richman (1986), might be preferred to seek a much stronger simple structure and facilitate the interpretation of modes of variability of the surge phenomenon.

1.1.2 Sources of Rainfall Variability in the NAMS

Different studies have linked moisture surges with enhanced rainfall in the NAMS region. Over the SW United States and NW Mexico, much of the intraseasonal rainfall variability seems to be related to the moisture surge phenomenon initially described by Hales (1972) and Brenner (1974) and more recently confirmed by many other studies (e.g., Reyes et al, 1990; Stensrud et al., 1997; Berg et al, 2000; Douglas and Leal, 2003; Higgins et al., 2004; Adams and Stensrud, 2007). The rainfall variability also may be related to westward moving tropical perturbations such as Tropical Easterly Waves (TEWs; Stensrud et al., 1997; Fuller and Stensrud, 2002; Adams and Stensrud, 2007), Tropical Storms (TSs; Higgins and Shi, 2004; Robert and Johnson, 2004), Tropical Cyclones (TCs; Douglas and Leal, 2003; Higgins and Shi, 2004), mid- to upper-level inverted troughs, and some other cyclonic disturbances that may often originate over the eastern coast of Mexico and Gulf of Mexico (Adams and Comrie, 1997). The development of the GoC Low-Level Jet (GCLLJ) (Douglas, 1995; Fawcett et al. 2002; Mo and Berbery, 2004) also influences the NAMS core region rainfall amounts. The GCLLJ is a characteristic feature of the time-mean southeasterly flow over the northern

GoC region and its intensification is closely associated with surge events (Schmitz and Mullen, 1996; Stensrud et al., 1997; Anderson at al., 2000b; Higgins et al., 2004).

Other known phenomena that influence the variability of the summer convective activity in the NAMS region are: passing upper-level troughs in the extratropical westerlies; the northward (southward) displacement of the subtropical ridge and formation of a cutoff "four-corners high-pressure system", which also results in an increase (decrease) in convective activity; and lower frequency (30-70 day) variations such as the Madden-Julian Oscillation (MJO; Higgins et al. 1998; Higgins and Shi, 2001; Lorenz and Hartmann, 2006). In particular, Lorenz and Hartmann (2006) suggested that westerly wind anomalies associated with the MJO active phase may increase rainfall in the NAMS core region through moisture surge events by either increasing the number of TCs in the eastern Pacific (Maloney and Hartmann, 2000), or by amplifying TEWs. They also suggested that the active phase of the MJO might favor an environment that would increase the Mesoscale Convective Systems (MCSs) activity. Consequently, the intraseasonal rainfall variability often seems to be physically connected through moisture surges, which possess intricate multi-scale characteristics.

There are other phenomena affecting the rainfall variability over the NAMS region on the intraseasonal to interannual timescales. For example, antecedent land surface conditions seem to play an important role in the onset and intensity of the monsoonal rainfall (Hawkins et al., 2000; Lo et al., 2002; Matsui et al., 2003; Zhu et al. 2005). Although these relationships appear to have a relatively large spatial and temporal variability, most results suggest that a wetter (drier) northern hemisphere winter/spring tends to delay (advance) the monsoon cycle and decrease (increase) monsoon rainfall amounts. However, Zhu et al. (2005) suggest that the intensity of the monsoon may depend more on large-scale forcings than on local antecedent soil moisture conditions. On the other hand, the interannual variability modes that tend to dominate the regional variations in air temperature and rainfall are those associated El Nino-Southern Oscillation (ENSO) (e.g., Adams and Comrie, 1997; Higgins and Shi 2001; Castro et al., 2001) and the North Pacific Oscillation (NPO) (e.g., Castro et al., 2001). In particular, the Castro et al. (2001) results, based on NCEP/NCAR reanalysis data, suggest that warm (cold) ENSO phases and high (low) NPO phases favor drier (wetter) and late (earlier) monsoon onsets.

Other atmospheric circulation patterns with a potential influence on NAM rainfall include the Pacific-North American (PNA) teleconnection pattern (Carleton, et al., 1990; Leathers and Palecki, 1992; Livezey and Smith, 1999), the North Atlantic Oscillation (NAO; Barnston and Livezey, 1987; Livezey and Smith, 1999; Fedstein, 200), the Subtropical Zonal pattern (Barnston and Livezey, 1987), and the Asian summer pattern (Barnston and Livezey, 1987; Lau and Weng, 2002). The behavior of quasi-stationary planetary-scale circulations also are tied to short term climate fluctuations. This is the case with the NAM, where numerous studies have suggested that the above-mentioned intraseasonal to interannual atmospheric circulation patterns have an effect on the intensity and meridional displacement of the subtropical ridge, which in turn affects the monsoonal moisture flux. For example, Fedstein (2007) showed that a positive NAO phase, with life cycles of about two weeks, is associated with deepening of mid-latitude synoptic-scale waves over western North America. A thorough analysis of the influence of these and other teleconnection patterns lies beyond the scope of this research. However, they constitute a source of potential predictability of the summer hydroclimate. Thus, future efforts should be oriented towards the identification of physical links that characterize the observed teleconnections with the NAM variability.

1.1.3 Moisture Surges and their Forcing Mechanisms

There are a number of phenomena that can initiate/control moisture surges, usually in association with enhanced convective activity. Depending on the forcing mechanism, some "major surges" originate to the south of the Baja California peninsula as a result of enhanced convective activity induced by westward-propagating disturbances, such as TSs/TCs or TEWs. The surface pressure gradient associated with the thermal contrast between the cold environment in the storm region (GoC entrance, GoC coastal plains, Sierra Madre Occidental (SMO) western foothills, Figure 2) and the warm environment in the low deserts (AZ and northwestern Sonora, Figure 2) enhances southeasterly flow along the GoC (see Figure 4), supporting the persistence of the flow. Surges also can be enhanced when TSs/TCs or TEWs interact with the SMO (Zehnder, 2004). Other less intense surges may originate within the GoC, even in the northern Gulf and over the coastal plains of Sonora, Mexico, as gravity currents induced by convective outflows produced by MCSs (Stensrud at al, 1997; Douglas and Leal, 2003). The outflows are channeled northward along the GoC and often are capable of producing short-lived (6-24 hour) moisture surge-related signals or "minor surges" (Hales, 1972).

Major surges (long-lived, spanning 2 to 3 days) are mainly associated with large-scale forcing mechanisms, such as tropical cyclones that pass south of the GoC (Stensrud et al. 1997; Douglas and Leal, 2003; Higgins and Shi, 2005). A recent compositing study by Higgins and Shi (2005) revealed that on average nearly half of the major surge events are associated with the passage of TSs/TCs to the south of the Baja California peninsula. The special topographic configuration provided by the SMO (which is located to the right of the surge motion and provides Coriolis trapping) and the vertical confinement resulting from strong stability, makes this type of surge similar to other Coastal Trapped Disturbances (CDTs; Gill, 1977) often observed elsewhere in the world. Well-known examples of other CTDs are the southerly buster in southeastern Australia (Raid and Leslie, 1999) and the coastal California southerly wind events (Mass and Albright, 1987; Reason and Steyn, 1992). Using numerical simulations, Anderson et al. (2000b) associated the persistence of major GoC surges with a geostrophic response induced by a TS/TC modified by the presence of the SMO. The mechanisms by which these TSs/TCs may be related to the initiation and evolution of surges is discussed theoretically by Zehnder (2004), where he proposed that a tropical cyclone that propagates along the coast may induce a Kelvin or Rossby edge wave that in some cases steepens into a nonlinear wave or bore. The different dynamical mechanisms proposed by Zehnder (2004) for surge propagation will be reviewed in Chapter 3. Other synoptic factors seem to have an impact on modulating the surge intensity, as found by Stensrud et al. (1997) who associated some strong moisture surges to the passage over western US of mid-latitude waves propagating eastward a day or two before the surge onset.

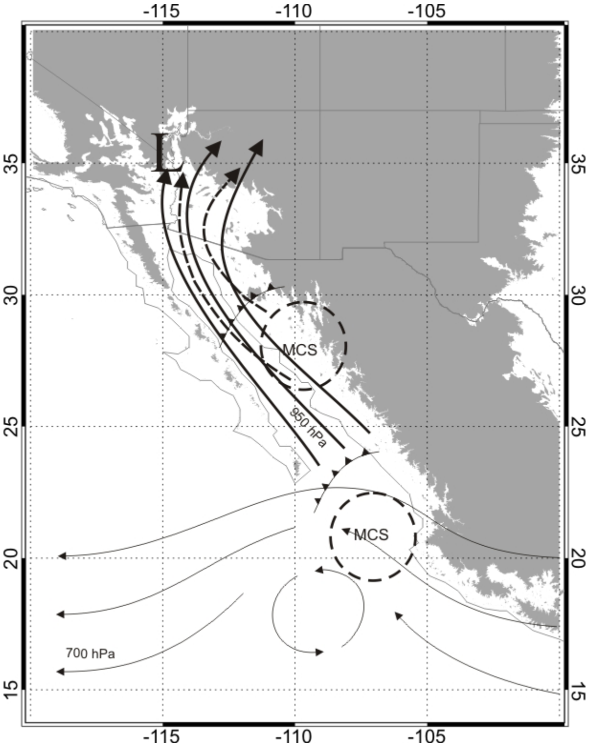

Figure 4. Conceptual model of major moisture surges (duration spanning from 2 to 3 days, thick solid streamlines) triggered by enhanced convective environment (MCS) south of the entrance to the GoC, favored or sustained by tropical cyclones (thin solid stream lines). Minor surges (usually short-lived, within a day, solid dashed streamlines) may develop due to enhanced convective activity in the central to northern GoC coastal plains. Shaded areas show topography below 750 m. This figure is adapted from Adams and Comrie (1998).

1.1.4 Numerical simulation of atmospheric processes within the NAMS region

Seasonal and intraseasonal rainfall forecast skill in the NAMS region is very limited (Gutzler et al., 2005). This limited skill is likely produced by unrealistic representations of some of the local-to-mesoscale atmospheric processes, such as the diurnal cycle of rainfall, proper representation of the GCLLJ and moisture surges, and the interaction of synoptic-scale processes with smaller (time and space) scales (Higgins and Gochis, 2006). A number of studies have evaluated the skill of mesoscale and regional models for the NAMS (Stensrud 1995, Stensrud et al. 1997; Anderson et al., 2000a, b; Fawcett et al., 2002; Gochis et al., 2002; Gutzler et al., 2005; Li et al., 2005; Adams and Stensrud, 2007). In particular, Gochis et al. (2002) found that the NCAR/ Pennsylvania State University Mesoscale Model 5 (MM5, 12km horizontal grid spacing) simulations of the low-level circulation and resulting rainfall field for the NAMS core domain were sensitive to changes in the convective parameterization schemes when comparing day-to-day results with observations. Similarly, the physical parameterizations in the models are grid-scale dependent which affects the representation of organized convection frequencies and intensity. For example, Li et al. (2005) performed a sensitivity analysis using the MM5 with explicit microphysics over the NAMS domain with different horizontal grid spacing (27, 9, and 3 km), which indicated that rainfall variations from monthly-to-hourly scales were better represented by using the finer grid-space (3 km).

Problems in forecasting diurnal and day-to-day rainfall variability in the NAMS domain, as well as its frequency and intensity, highlight the poor performance of mesoscale models when representing the effect of transient disturbances. Comparisons between observations and global model simulations differ particularly in the phase and amplitude of the diurnal cycle of rainfall (Gutzler et al., 2005). For the case of the NAMS core region, the simulated afternoon rainfall maxima occurs about 3 hours earlier compared to the observations, indicating the importance of convection schemes in the models to represent atmospheric circulations and thermodynamic effects. On the other hand, numerical simulations using mesoscale and regional models (Stensrud 1995, Stensrud et al. 1997; Anderson 2001; Fawcett et al., 2002) tend to locate the GCLLJ over the western foothills of the SMO as a result of the thermal contrast in the region, while observational studies (Douglas, 1995 and Douglas et al., 1998) tend to locate the GCLLJ along the eastern margin of the northern GoC. Anderson et al. (2000a) studied the diurnal cycle of the low-level winds and their spatial distribution in the GoC region by separating GoC surge days from non-surge days. They used numerical simulation data in periods when two field campaigns (Southwest Area Monsoon Project (SWAMP) 90, 95) permitted the intercomparison between observations and model output. They analyzed two months of simulations, one month during each summer season (Anderson et al. 2000b) and reported that model output corresponded well with the available observations). Their main result describe the important structure of the Gulf low-level atmospheric circulations under the influence of synoptically forced surge events and highlight the importance of the GCLLJ as a physical linkage between the moisture surges and tropical perturbations that may have initiated them. Anderson et al. (2001) also showed that during surge conditions, the low-level diurnal cycle is modified by the large-scale surge pressure gradient which weakens the upslope flow during the daytime and strengthens the nocturnal GCLLJ. Stensrud et al.'s (1997) simulations further support this idea, since they found that the surge (leading edge) appeared to slow down during the late afternoon.

While theoretical studies of moisture surges (e.g., Zehnder, 2004) can indicate the basic features of idealized surge events and are useful to examine the roles of particular processes, it is necessary to use high-resolution mesoscale models to analyze in more detail the real-world influences of topography, surface fluxes, planetary boundary layer processes, and background synoptic conditions. Such model simulations also are needed to investigate the sensitivity of moisture surges to varying synoptic conditions (Adams and Stensrud, 2007) and the effect of convective and diabatically-induced phenomena, such as convective outflows and GoC sea- and landbreezes. For example, Adams and Stensrud (2007) determined the impact of TEW by removing its associated variability from the MM5 model boundary conditions. Their simulation results suggested that TEWs partially modulate the intensity and spatial distribution of the NAM core region through their connection with moisture surges. On the other hand, improved simulation and understanding of the diurnal cycle and its variability during a surge's lifetime also are important, since the diurnal cycle influences internal processes such as the GCLLJ intensity and timing and modulates the development of MCSs which, in turn, affect the low-level flow and moisture transport.

1.2 Physical Hypotheses

External synoptic forcing plays an important role in determining whether surge events develop along the GoC. However, important prerequisites for improved rainfall predictions over the NAMS are a better understanding of the relationships between moisture surges and rainfall, and dependence of the moisture surge characteristics on different synoptic-scale disturbances. Identifying and understanding processes that interact locally with the surge through its lifetime also are essential for assessing the surge response and ensuring its correct simulation. The following hypotheses accordingly were investigated:

1) *Regarding the surge onset and the convective activity*: The presence of MCSs in the southern GoC immediately before an MCS-related surge onset can modulate the intensity of the moisture surge, regardless of the type of tropical synoptic-scale disturbance associated with the surge.

2) *Regarding the surge intensity, low-level jet strength and convective activity*: The surges modify the diurnal circulations along the GoC coastal plain, partly through enhanced convective activity, which enhances the offshore flow along the eastern coast and which further enhances the nocturnal low-level jet in the northern GoC.

3) *Regarding the evolution of convective activity during surges*: Enhanced convective activity during surges propagates northward along the GoC coast as a response to different factors. At lower levels, the surge induces moist convective instability that is superimposed on the prevailing orographic forcing. At upper levels, the synoptic forcing induced by the westward propagating disturbances maintains long-lasting organized convection (MCSs) and is responsible for the northwestward migration of the enhanced convective activity.

Concerning the first hypothesis, the moisture surge initiation has been related to the presence of MCSs in the lower GoC and eastern Pacific for many years. The original explanations of Hales (1972) and Brenner (1974) saw moisture surges as the response of the lower troposphere to the thermal contrast produced by organized convection that develops in the lower GoC region, disrupting the thermal equilibrium between the lower GoC and the low-deserts of Sonora and Arizona. Recently, the impacts of TSs/TCs and TEWs on long lasting surges also have been documented (Stensrud et al. 1997, Douglas and Leal, 2003, Higgins and Shi, 2005), concluding that there is a strong relationship between TEWs and moisture surge occurrence. However, the effects of enhanced convective activity associated with a synoptic-scale disturbance, prior the surge onset, have not been explored. Rather than focusing on the combined effects of the TEW (and TS/TC) and enhanced convective environments, this hypothesis focuses on separating the contributions to the surges by the larger-scale cyclonic disturbances and more local MCSs. If the effect of pre-surge MCSs on the moisture surge is substantial, either by increasing the moisture transported by the surge or by increasing the wind speed, then the correct prediction of pre-surge MCSs will impact the overall prediction of the intensity of the surge event.

In considering the second hypothesis, it is important to recognize that the GCLLJ apparently is a response to the thermal contrast between the GoC, its eastern coast, and the western slopes of the SMO. The northward along-GoC pressure gradient, associated with the SW United States low-desert and central-GoC region thermal gradient, also supports the formation of the GCLLJ. This GCLLJ is observed on most summer days, with maximum altitude averaging 500 m (Douglas, 1995), but its intensity is variable in time. The mean conditions seem to be modified by enhanced convective activity that in turn is related to moisture surges. As this modification occurs, strong MCSs in the northern GoC coastal plains will result in enhanced offshore convective outflow that will directly accelerate the LLJ by advection of momentum and by increasing the offshore pressure gradient when the GoC coastal plains hydrostatically adjusts to low-level cooling associated with the MCS episodes. Mature and decaying MCSs are capable of producing mesoscale pressure areas regions term “mesohighs” (Johnson et al., 1989; Johnson, 2001). Weakening of the afternoon sea breeze also is expected, since increased soil moisture and cooler surface temperatures due to MCS’s rainfall and cloud cover will reduce the thermal contrast that drives the sea breeze. In general, this hypothesis will show whether there is a relationship between the surge and the enhanced convective activity and its effect on the local circulations. The first and second hypotheses are incorporated in this research to improve the understanding of the two principal modes of transient variability of moisture transport over the NAMS core region.

The third hypothesis seeks to clarify the dynamics and thermodynamics involved in the surge-synoptic disturbance-rainfall relationship. Today, it is well accepted that convective activity in the NAMS core region and moisture surges are closely tied to the passage of westward propagating disturbances over the NAMS region (Stensrud et al., 1997; Fuller and Stensrud, 2000; Higgins at al., 2004; Adams and Stensrud, 2007). In general, these studies have found a westward propagation of the enhanced rainfall anomalies over Central Mexico that later move over the NAMS core region, suggesting a strong relationship with the westward propagating disturbances. None of these studies, however, has addressed the dynamical and thermodynamic evolution associated with surge events and the enhanced convective activity in the monsoon core domain.

It is clear that the large-scale synoptic pattern and terrain-induced circulations play an important role in determining whether MCSs will occur (McCollum et al., 1995). Given that vertical motion in the monsoon core region is triggered primarily by orographic forcing, we suggest this combination also is important in assessing the third hypothesis. For example, Higgins at al. (2004) suggested that the occurrence of a southeast-northwest propagation of positive rainfall anomalies is related to the surge progression along the GoC. They speculated that the low-level forcing of moisture surges is associated with an increase of the boundary layer Convective Available Potential Energy (CAPE), despite an increase of static stability observed at low-levels close to the central GoC coast after the surge passage (Douglas and Leal, 2003). Higgins et al. (2006) recalled that the presence of moist low-level southeasterly flow often is associated with large-scale environments that control the amount of convective activity such as the passage of easterly wave troughs over western Mexico and the location of the upper-level anticyclonic circulation associated with the monsoon. If an increase of lower-troposphere moisture creates a potentially and convectively unstable layer, the presence of surges in the GoC region enhances the likelihood of convective development (by changing static instability). As this occurs, the presence of easterly wave troughs provides enhanced relative cyclonic vorticity resulting in regions with large-scale upward motions. Despite these findings, the physical mechanisms responsible for the relationship between the synoptic-scale disturbances over the NAMS core region and its effect over moisture surges and rainfall anomalies are still unclear and deserve further research.

1.3 Structure of this research

A major field campaign, the North American Monsoon Experiment (NAME), was carried out from June to September 2004 to stimulate progress in the predictive capability for warm season rainfall over the region on the diurnal to intraseasonal time-scales (Higgins et al., 2006). NAME focused on enhancing observations in the NAMS core region (Figure 2) for the experiment period. The observational platforms deployed during this field campaign were designed to better observe and document the major processes that contribute to the NAMS rainfall variability. They provided intensive monitoring of the diurnal wind field and rainfall cycles, multi-day moisture surge events, and day-to-day GCLLJ variability, among others. A TS/TC-related moisture surge and two other surges related to westward propagating wave disturbances occurred during NAME, providing high-resolution data that can be used to address questions related to surge initiation and evolution. The TS/TC-triggered moisture surge of July 12-15, 2004, is considered a good example of such a phenomenon (Rogers and Johnson, 2006). The enhanced observations obtained during NAME and their intensive diagnosic analyses, some of which are uniquely documented in this research, made it possible to test the above hypotheses (Section 1.2) on the general structure of the moisture surges.

Although there are several studies relating NAMS synoptic-scale conditions and their linkage with regional rainfall patterns, the specific connections among different scales still remain under-investigated. For example, the physical description of moisture surges and the possible role of mesoscale convective activity have not been addressed yet. The present research addresses these needs and describes the physical connection between the relative roles of the synoptic-scale forcing and MCSs in the development and intensity of GoC moisture surges. This research is divided into four sections, beginning with a description of the data and the general methodology used throughout (Chapter 2).

The subsequent section (Chapter 3) contains a comprehensive description of the TS-triggered surge event of July12-15, 2004, that was sampled by the NAME observational systems. The next section (Chapter 4) compares the major moisture surge features identified in Chapter 3 against the characteristics of a set of surge events extracted from 17-year (1983-2006) satellite and surface station data sets. Here, moisture surges are composited using NCEP North American Regional Reanalysis (NARR; Mesinger et al., 2006) and QuikSCAT products to highlight further their triggering mechanisms and some associations with convective variability observed at different scales. This helps address the relative impact of convective activity associated with different special-temporal scale patterns on major surge events. Additionally, this research includes relationships between MCSs, day-to-day variability of the GCLLJ, and occurrence of minor surges. A final section (Chapter 5) investigates the ability of the Weather and Research Forecasting (WRF) model developed by the National Center for Atmospheric Research (NCAR) (the Advanced Research WRF, ARW) to reproduce key findings in preceding chapters. This section also uses idealized simulations designed to explore the relative roles of processes within the GoC (e.g., sea breeze circulation, convective activity, etc.) for moisture surge propagation characteristics, like intensity and timing. In addition, the potential effects on surge genesis of different ARW physical parameterization schemes are explored.

1.4 Relevance

The research summarized above helped advance the conceptual understanding of the relative impact of MCSs during different stages of GoC moisture surges using the observations obtained during NAME, NARR products, and historical satellite imagery. The findings extracted from these data sets have the potential to improve the understanding of the multi-scale processes occurring during surge events (Higgins and Gochis, 2006), including their diurnal variability and the association with enhanced convective activity in the NAMS region. These results contribute to the identification and classification of intense convective processes associated with GoC moisture surges, which is valuable in the broader context of tropical weather system behavior and variability.

Additionally, the research includes testing the efficacy of limited area numerical simulations to reproduce surge evolutions. Improving mesoscale forecasting and regional models provides immense benefits in regions with limited water resources, such as the NAMS domain. To achieve this goal for the NAMS, many of the problems involved already have been identified in the NAME Model Assessment Project NAMAP (Gutzler et al., 2005), which has assessed the understanding of basic processes that may potentially increase the seasonal prediction skill. Some of the problems in the existing models are summarized in Higgins and Gochis (2006), and include improper representation of coastal effects, ineffective generation of rainfall systems over complex terrain, and weak coupling between the diurnal cycle, propagating convection, and synoptic-scale disturbances. Since these and other model limitations can have an impact on moisture surge representation, this situation was reflected in the formulation of the hypotheses for this study.

2 DATA AND METHODOLOGY

This section discusses the data used in this study and the principal analysis procedures employed. The first subsection describes the 2004 North American Monsoon Experiment (NAME) observations, the analysis of which will be presented in Chapter 3. The second subsection describes the use of NARR and satellite imagery products in the compositing presented in Chapter 4. The last subsection describes the numerical simulations with the ARW model that constitutes the basis of Chapter 5.

2.1 NAME Observations

Routine and special observations were collected during the 2004 NAME (Higgins et al., 2006). The overall NAME activity aimed to improve understanding of the summer monsoonal circulation at different spatial scales over the southwestern United States and northwestern Mexico, with the objective of improving predictions on intraseasonal-to-interannual time scales. As northwestern Mexico lacks sufficiently dense routine meteorological observations, it is only through intense field campaigns, e.g. SWAMP-90 (Meitin, 2001; Douglas, 1995), SWAMP-95 (Douglas et al., 1998), and NAME-04 (Higgins et al., 2006), that it has been possible to address questions regarding mesoscale phenomena and their links to large-scale monsoonal patterns, and to evaluate numerical simulations of those phenomena. NAME measurement platforms included rawinsondes, research aircraft, research vessels, wind profilers, raingauges, radar, and buoys. Within the NAME extended period (1 July to 15 August), Intensive Observation Periods (IOPs) were called by the NAME scientists with specific emphasis on key synoptic and mesoscale features including: monsoon onset, moisture surges, GCLLJ, tropical waves, and MCSs. Table 1 lists the type of IOPs and their specific mission. Every IOP consisted mainly of an increased frequency of atmospheric soundings, from 1-2 observations per day during routine operations to 4-6 observations per day during IOPs depending on the station and the type of IOP, and also included some special aircraft missions (~8 hours per flight). Specifically, this study focuses on the second IOP called to sample a moisture surge event and periods of enhanced GCLLJ. Table 2 contains a list of the observational platforms available throughout the NAME period. Figure 5 shows the spatial distribution of the instruments during NAME.

Table 1. General description of IOPs during NAME from July 1 to August 14, 2004. Qflux refers to special aircraft missions designed to observed low-level vertical and horizontal distribution of moisture flux over the GoC and surrounding areas.

IOP #	Type	Date	Description
IOP-1	Qflux/Monsoon Onset	July 8-10	Examine the low-level moisture fluxes.
IOP-2	Moisture surge/ GCLLJ	July 12-15	Well-observed surge events. TS-related surge event
IOP-3	Qflux /GCLLJ	July 20-24	There was a TEW trough crossing over GoC entrance on the 25. However, there are different late night MCSs associated with a GCLLJ even.
IOP-4	Qflux	July 28-30	Examine the low-level moisture fluxes.
IOP-5	Moisture Surge	Aug 2	Moderate surge events. MCS developed early on Aug 2 (The flow exhibits a surge-related structure with southeasterly winds lasting less than 24hours) “minor surge”.
IOP-6	Qflux	Aug 4	During the Aug 3 there is a break in southeasterly flow, and an associated dryness. The TEW is there and together with an MCS convective outflow, the Yuma surge “minor-to-medium size” starts again around Aug 4 at 12UTC.
IOP-7	Qflux	Aug 6-9	Examine the low-level moisture fluxes.
IOP-8	Qflux	Aug 10-12	Examine the low-level moisture fluxes.
IOP-9	Qflux	Aug 13-14	Examine the low-level moisture fluxes.

Table 2. General description of field instruments during NAME. See list of acronyms at the bottom of the table.

Type of Platform	Institution	Number of Stations	Sampling frequency	Comments
Surface Meteorological Station	MXNWS	30	1-hrly, 3-hrly, 6hrly	Permanent
	CICESE	1	20 min	Permanent
	NCAR/ISS	4	10 min	NAME/EOP
	SEMAR	8	30 min	Permanent
	AgroMetSon	13	10 min	Permanent
	USNWS	50	1 min	Permanent
Rawinsonde Station	MXNWS	10	~4 hrly (IOPs)	Permanent, normally 1-2 per day
	USNWS	10	~4 hrly (IOPs)	Permanent, normally 2 per day
	NCAR/ISS	4	~4 hrly (IOPs)	NAME
	NOAA/ETL	1	~4 hrly (IOPs)	NAME, Onboard ship system
Pibals	NSSL	25	~2-3 daily	NAME, AM and PM wind measurements.
Wind profilers	NCAR/ISS	4	30 min	NAME; 0-3 km of vertical range
Radar	MXNWS	2	15 min	Radar systems over the lower GoC region
	NCAR/SPol	1	15min	
Rain gauges	NERN	80	10 min	Available for NAME since May 2002, (Gochis et al., 2004)
NOAA WP-3D	NOAA/AOC	10 Flights 2 Surge genesis missions.	1 second	300-3000 Km, vertically (Porposing pattern); cross-Gulf Zigzag legs, horizontally (Mejia and Douglas, 2005)

Acronym list: **AgroMetSon**: Sonora (Mexico) Agrometeorological network; **AOC**: Aircraft Operations Center; **CICESE**: Centro de Investigación Científica y de Educación Superior de Ensenada, Mexico; **EOP** Enhanced observation Period; **ETL**: Environmental Technology Laboratory; **IOP**: Intensive Observation Period; **ISS**: Integrated Sounding System; **MXNWS**: Mexican National Weather Service; **NCAR**: National Center for Atmospheric Research; **NERN**: Northwest Mexico NAME Event Raingage Network; **NOAA**: National Oceanic and Atmospheric Administration ; **NSSL**: National Severe Storms Laboratory; **SEMAR**: Secretaría de Marina, Mexico (Mexican Navy); **SPol**: ground-based dual-polarimetric 10 cm wavelength (S-band) weather radar deploided during NAME; **USNWS**: United Stated National Weather Service; **WP-3D**: refers to the Lockheed WP-3D Orion research aircraft.

Rogers and Johnson (2006) analyzed a specific surge event that occurred during NAME IOP-2, with emphasis on the observational aspects based on the NCAR/ISS wind profiler array and objectively analyzed rawinsonde observations. In contrast, the present study emphasizes analysis of the aircraft observations that provide both over-Gulf and vertical structure perspectives of this surge event. Surface stations and upper-air observations also are used to help provide the spatial and time continuity to support interpretation of the observed structures. Comparisons with the results of Rogers and Johnson (2006) are discussed throughout and additional findings are highlighted.

The goal in the analysis of surface stations to evaluate the propagation properties of the surge main signal was to obtain the surge signal nearly independent of smaller-scale local circulations. Since the diurnal cycle may be modified as the surge progresses (Anderson et al, 2000b), it was decided to apply a 24-hour running mean which preserves the non-stationary trends for frequencies lower than this time window. Some other higher frequency signals, e.g., produced by convective outflow or other mesoscale phenomena, will be dampened by this technique. A more sophisticated technique using Wavelet filtering also was tested but the remaining signal was over-smoothed, and obscured the surge initiation and other features needed to track the surge.

Some surface stations, like the MXNWS stations, did not report sea-level pressure, but rather the surface pressure. Thus, sea-level pressure (SLP) was reduced based on the station elevation and the backward 12-hour mean temperature at the station (Chu, 1994). Finally, the anomalies of surface temperature, dew point, SLP, and surface winds were used to identify different aspects of the surge; for the analysis of IOP-2 the anomalies were obtained by subtracting the quantity's average over the interval from July 7 to 18. This time interval, somewhat arbitrary, was selected in order to cover at least a whole wavelength in the synoptic timescale driving the surge event (~10 days).

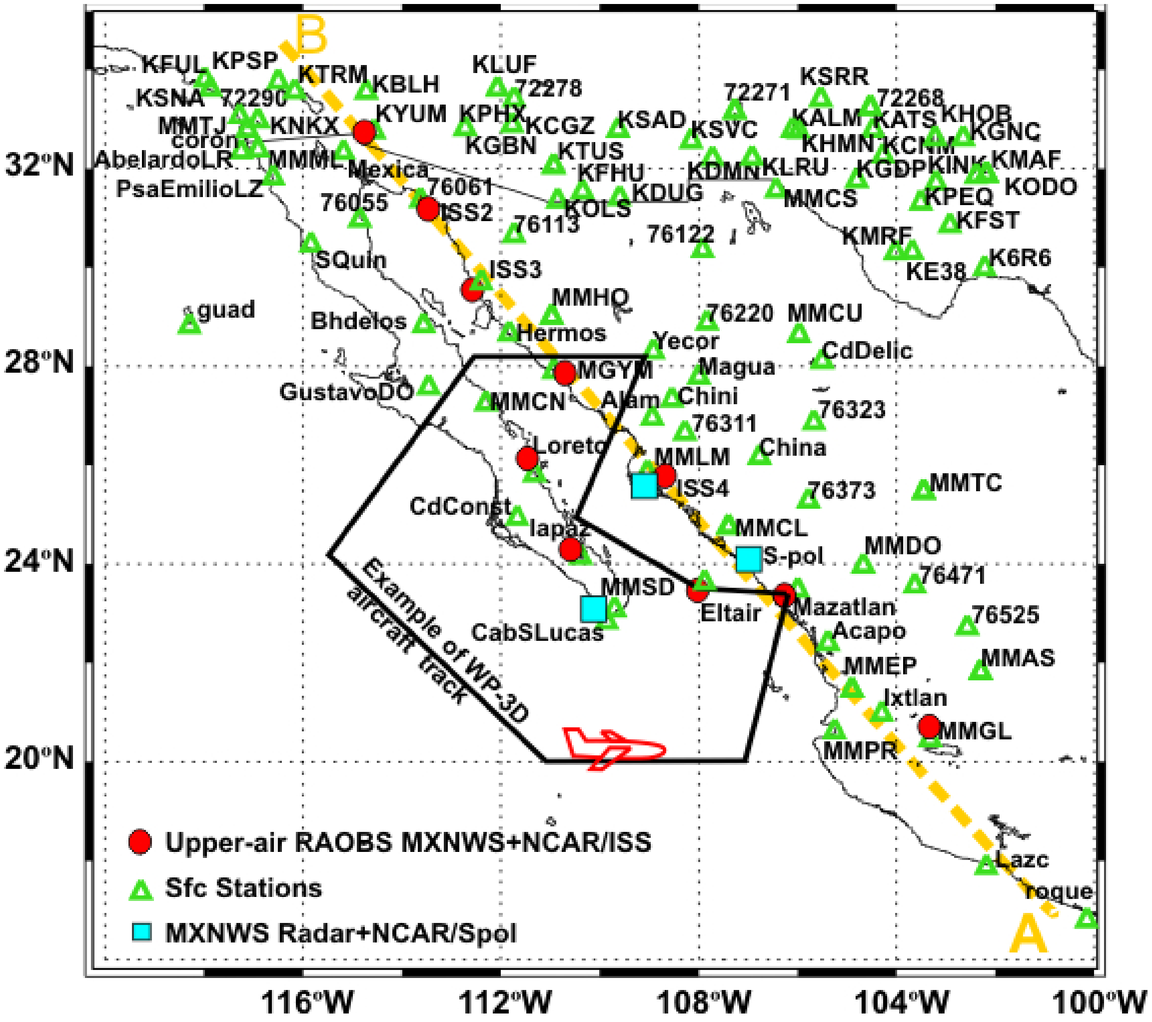

Figure 5. Distribution of key field instrument platforms during NAME. See Table 2 for institutions responsible and some general descriptions of the NAME network. Also shown is the alongshore transect A-B (dashed line) used for some analyses, including an example of a typical WP-3D flight track (solid line).

1.1 NARR and Satellite Products

2.1.1 NARR

The NCEP North American Regional Reanalysis (NARR, Mesinger et al., 2006) wind, temperature, geopotential height, and specific humidity are used to examine the mean surge atmospheric environment associated with different convective situations and in the presence of different westward propagating synoptic and convective activity (e.g., TSs/TCs, TEWs, inverted troughs, MCSs). NARR is a high-resolution climate dataset for North America providing significant improvements over earlier global reanalyses (e.g., National Centers for Environmental Prediction (NCEP)/ National Center for Atmospheric Research (NCAR) Global Reanalysis). Additionally, NARR uses a regional scale model (Eta Model), and assimilates hourly rainfall from various sources (e.g. raingauges over Continental US, Mexico, and Canada, and Climate Prediction Center (CPC) Merged Analysis of Precipitation (CMAP; Xie and Arkin, 1997) over the oceans), and all other observations used in the NCEP/NCAR Global Reanalysis. Available from 1979 to the present, the NARR data have 3-hourly time resolution, 32 km spatial resolution, and 29 vertical levels with half below 700 hPa. Compared to global reanalysis data sets, NARR includes a major increase in resolution and associated improvements in the accuracy of temperatures and winds (Mesinger et al., 2006). Consequently, it is expected that the NARR data can help identify the mean characteristics of moisture surges for a multiyear set of surge events. Furthermore, systematic comparisons of the NARR wind, temperature, and moisture fields are performed against observations obtained during NAME and various configurations of simulation outputs.

NARR products have been used for prior diagnostic studies over the NAMS region. Higgins and Shi (2005) composited a set of surge events based only on their relationship with eastern Pacific TSs/TCs events, and were able to estimate an average surge propagation speed (10 m s-1). This average propagation speed was less than those from numerical (Stensrud et al., 1997) and observational (Robert and Johnson, 2006) studies. Mo et al. (2005) found that NARR overestimates the meridional wind over the northern GoC, affecting the GCLLJ diagnosis, and also relatively poorly represents the PBL and daily processes in the region. Two direct contributions of the present research compared to these previous studies involve the improved separation of mechanisms that may trigger moisture surges, such as using different type of westward moving synoptic-scale disturbances, and capturing the specific role of the MCS for surge onset. It still is expected that these analyses using the NARR have limitations and the reasons for the differences are still being investigated and need further assessment. Given the poor density of observations in Mexico and over the eastern Pacific Ocean, the NARR constitute the best source of atmospheric information in the region and an essential multi-year diagnostic analysis tool.

2.1.2 GOES products

A part of the satellite imagery used in this research (Chapter 3) is a Geostationary Operational Environmental Satellite (GOES-12) product (4 km spatial resolution, 30 minute temporal resolution) that was employed to display the convective activity during the NAME IOPs. The additional satellite imagery analyzed in Chapter 4 is a GOES-7, -9, and -10 product obtained from the International Satellite Cloud Climatology Project (ISCCP) (Knapp, 2008; ISCCP B1U http://www.ncdc.noaa.gov/oa/rsad/gibbs/gibbs.html). The temporal resolution of the GOES-7, -9, and -10 radiance data is 3-hourly available since 1983, and the spatial resolution is ~10km at nadir. These ISCCP B1U historical data are used here to facilitate the identification of enhanced maritime and continental convective activity in the region, especially for MCSs in the core NAMS region. The procedure for the retrieval of significant convective events, e.g. to objectively identify individual MCS events, is explained in Chapter 4. The evolution of cloudiness associated with the moisture surges also is developed from the GOES-7, -9, and -10 data as a function of the synoptic-scale precursors.

2.1.3 QuikSCAT

The SeaWinds in the QuikSCAT Level 3 gridded ocean winds data set (QuikSCAT winds) are used in this research to evaluate the consistency of NARR surface winds for capturing the main temporal and spatial oceanic surface wind structures associated with moisture surges (Chapter 4). This QuikSCAT data set, obtained from the National Aeronautics and Space Administration –Jet Propulsion Laboratory (NASA-JPL ftp://podaac.jpl.nasa.gov /pub/ocean_wind/seawinds/L3/), is available from July 19, 1999, to the present and is provided on a 0.25° grid size. The comparison of NARR surface winds against the QuikSCAT winds was carried out by averaging the ascent and descent satellite passes (~6 LT and 18 LT, respectively) for each day. The advantages and problems of the QuickSCAT winds have been discussed in different studies (Hoffman and Leidner, 2005; Chelton et al, 2006). In general, this data set is valuable to locate significant surface meteorological features over the ocean except where the data are contaminated by moderate to heavy rain events. However, this may produce a significant disadvantage since we mainly are interested in the wind disturbances associated with convectively active systems, such as TEW and TS/TC.

2.1.4 MJO indices

MJO events can be identified using two different MJO indices. These are described below.

2.1.4.1 MJO CHI200-based index

The NOAA Climate Prediction Center (CPC) MJO composite index (Xue et al., 2002) is based on the 200 hPa velocity potential (CHI200); the normalized indices can be downloaded from the CDC website at http://www.cpc.ncep.noaa.gov/products/precip/CWlink/daily_mjo_index/pentad.shtml). This MJO index (hereafter referred as MJO CHI200-based) was obtained by regressing a bandpass filtered (30-90 day) CHI200 fields using non-overlapping pentads (obtained from NCEP/NCAR reanalysis data) of the first extended empirical orthogonal function (EEOF) of ten spatial patterns centered at different longitudes around the globe (80°E, 100°E, 120°E, 140°E, 160°E, 120°W, 40°W, 10°W, 20°E, and 70°E). Specifically, the MJO CHI200-based index associated with the 120°W spatial pattern was selected for use here.

2.1.4.2 MJO OLR-based index

The second MJO index is based on outgoing longwave radiation (OLR) averaged over the eastern Pacific using a technique (Wheeler and Weickmann 2001) as in Barlow and Salstein (2006). This MJO index (hereafter referred to as MJO OLR-based) is obtained from daily Fourier bandpass-filtered OLR, which was set to retain eastward propagating zonal wavenumbers (1-5) and later averaged over the eastern Pacific

[100°W-80°W, 10°N-15°N]. Daily-averaged OLR data (Liebmann and Smith, 1996) available at 2.5° resolution is used to produce this MJO index.

The MJO CHI200 is based on large-scale upper level circulation anomaly patterns and the MJO OLR index is based on satellite-derived tropical convective cloud anomalies. Hence, we expect to obtain more robust results when working with both indices. Although each index provides different samples of MJO events, there is significant overlapping due to the dynamical processes that connect them. For example, large-scale upper-air divergence (convergence) is associated with negative (positive) velocity potential anomalies, and usually is connected to the low-level convergence (divergence), which in turn provides enhanced (suppressed) large-scale rising motion, hence, enhanced (suppressed) convective activity. Therefore, the active (inactive) phase of the MJO is associated with negative (positive) anomalies of CHI200 or OLR. Here, we assumed that positive (negative) OLR anomalies were associated with suppressed (enhanced) convective activity. The use of both MJO indices was justified because not every MJO event is convectively active over the eastern Pacific (EPAC) region and, similarly, not all variations in the convective field on the intraseasonal timescales are associated with MJO events. It might be noted that cloudiness variations associated with local ocean-atmosphere processes may influence the MJO OLR-based classification procedures. One such local processes could be the intraseasonal variations induced by the mid-summer drought. The mid-summer drought is a climatological decrease in the mean summer rainfall amounts during July-August with a strong signal over Central American and southern Mexico (Magaña et al., 1999), which in turn could be externally modulated by non-local effects such as the MJO (Barlow and Salstein (2006).

2.2 Numerical Simulations

The ARW is a mesoscale model developed by a community of scientists at different research centers (Skamarock et al., 2005). The ARW model employs flexible code that is efficient in a parallel computing environment, offers numerous physics options, and is suitable for use in a broad spectrum of applications across space scales ranging from meters to thousands of kilometers. Specifically, this research uses Version 3 of the ARW mass dynamical core. The dynamical core is a fully compressible, three-dimensional, non-hydrostatic (with option of run-time hydrostatic) model with governing equations written in flux form. This model was used to carry out different experiments that focus on the moisture surge representations for real and more-idealized runs. Real cases were run for NAME surge events, the outputs of which are compared in Chapter 5 with observational analyses presented previously in Chapter 3. Associated sensitivity analyses were performed by changing the spatial resolution of the model and modifying pertinent physical parameterization schemes, such as those associated with rainfall and PBL processes.

Also in Chapter 5, a series of experiments were undertaken to study moisture surges for different synoptic-scale forcing mechanisms, as prescribed in the boundary and initial conditions. All these experiments provided understanding of the model limitations when simulating moisture surges under different triggering mechanisms. They also highlighted some striking associations with enhanced mesoscale convective activity in the region. In some experiments, a cold bubble was inserted over the GoC entrance at different points (different times of the day) during the surge's initial stages. This approach mimiced the effect of this "convective environment" during the surge genesis, and whether or not surge genesis and its intensity is phase-locked with the diurnal processes within the GoC. In other experiments, using the same cold bubble approach, convective outflows were inserted over the GoC coastal plains to study whether this can significantly modulate the GCLLJ intensity. More details of the model description and experimental procedures employed appear in Chapter 5.

3 DETAILED STRUCTURE OF 12-15 JULY SURGE EVENT DURING NAME-2004 FIELD PROGRAM

This chapter describes observational aspects of a moisture surge event observed during NAME. These observations constitute a unique opportunity to diagnose moisture surge lifecycles with a reasonable level of detail. In particular, the focus is on the IOP-2 event (12-15 July), which has been categorized as a "major" moisture surge associated with TS Blas. The fundamental objective of this observational analysis is to document the propagation and evolution, from genesis to decay, of these uniquely measured surges during NAME. Additional aspects for which an explanation is sought include: (1) the propagation mechanism of the surge leading edge; (2) the dynamical and thermodynamical processes maintaining the surge during its evolution; (3) for IOP-2, exploration of the mechanisms by which surge initiation and evolution are related to Tropical Storm Blas; and (4) the role of convection in the surge initiation and modulation. This case study contrast strongly with previous compositing results (Stensrud et al., 1997; Douglas and Leal, 2003; Higgins and Shi, 2005), since particular processes can better be identified based on case study observations, especially those associated with the surge onset.

The emphasis in this chapter is on describing the dynamical properties of the surge and assessing the role of convective activity during a surge life cycle. Initially, a brief summary (Section 3.1) of the moisture surge events that occurred during NAME is presented, followed by a more detailed description of the mesoscale and synoptic environments associated with the surge. Surface observations are analyzed first to follow the evolution of the surge and to estimate their phase velocities (Section 3.2). Flight-level aircraft observations provide the spatial structure of the surge's leading edge during IOP-2, which in turn is compared with several proposed theoretical propagation modes (Section 3.3). At this stage, no attempt is made to identify the origin of the surge, however, some hints of the possible triggering mechanisms leading to this surge are discussed. The interaction of the surge with local circulations and its relationship with enhanced convective activity then is assessed (Section 3.4). The vertical structure of the surge is described from rawinsonde data and aircraft data (Section 3.5). Finally, some preliminary conclusions and remarks are presented (Section 3.6).

3.1 Synoptic and Mesoscale environments

Nine IOP's were carried out during NAME to observe different features related to the moisture flux field over and adjacent to the NAMS core domain (Table 1). Figure 6 shows a longitudinal Hovmoller diagram of the meridional wind at 700 hPa that depicts the synoptic variability that occurred during the entire NAME, as well as the WP-3D aircraft mission called during different IOPs. The surge event of July 12-15 during IOP-2, was a strong TS-related surge. This research shows results from IOP-2.

The large-scale environment during IOP-2 consisted of a well-marked mid-tropospheric TEW that propagated westward across Central Mexico on 11 July. This feature can be tracked over Mexico and then over the eastern Pacific (Figure 6). By 12 July at 15UTC, it was declared a Tropical Depression by the National Hurricane Center at (14.8ºN, 105.8ºW), which later became TS Blas from 13 July at 00UTC (16.4ºN, 107.9ºW) to 14 July (22.10ºN, 116.6ºW), when it was downgraded to a Tropical Depression (Figure 7). TS Blas predominantly moved WNW at about 10 ms^{-1}. Additionally, this surge event coincides with an active MJO event (Figure 8). Some discussion regarding this association are presented in Chapter 4.

Organized convective systems developed over northwestern Mexico, with two MCSs apparently being associated with the surge (Figure 7). The first MCS developed over the Nayarit/Sinaloa coast 350 km to the south of the GoC entrance (Figure 2) on 12 July 07UTC and moved offshore and dissipated by 14UTC. A second MCS developed over the central GoC coastal plain around 13 July 05UTC, dissipating 6 hours later. The sections that follow will refer to these two features and their role during the surge genesis and its evolution.

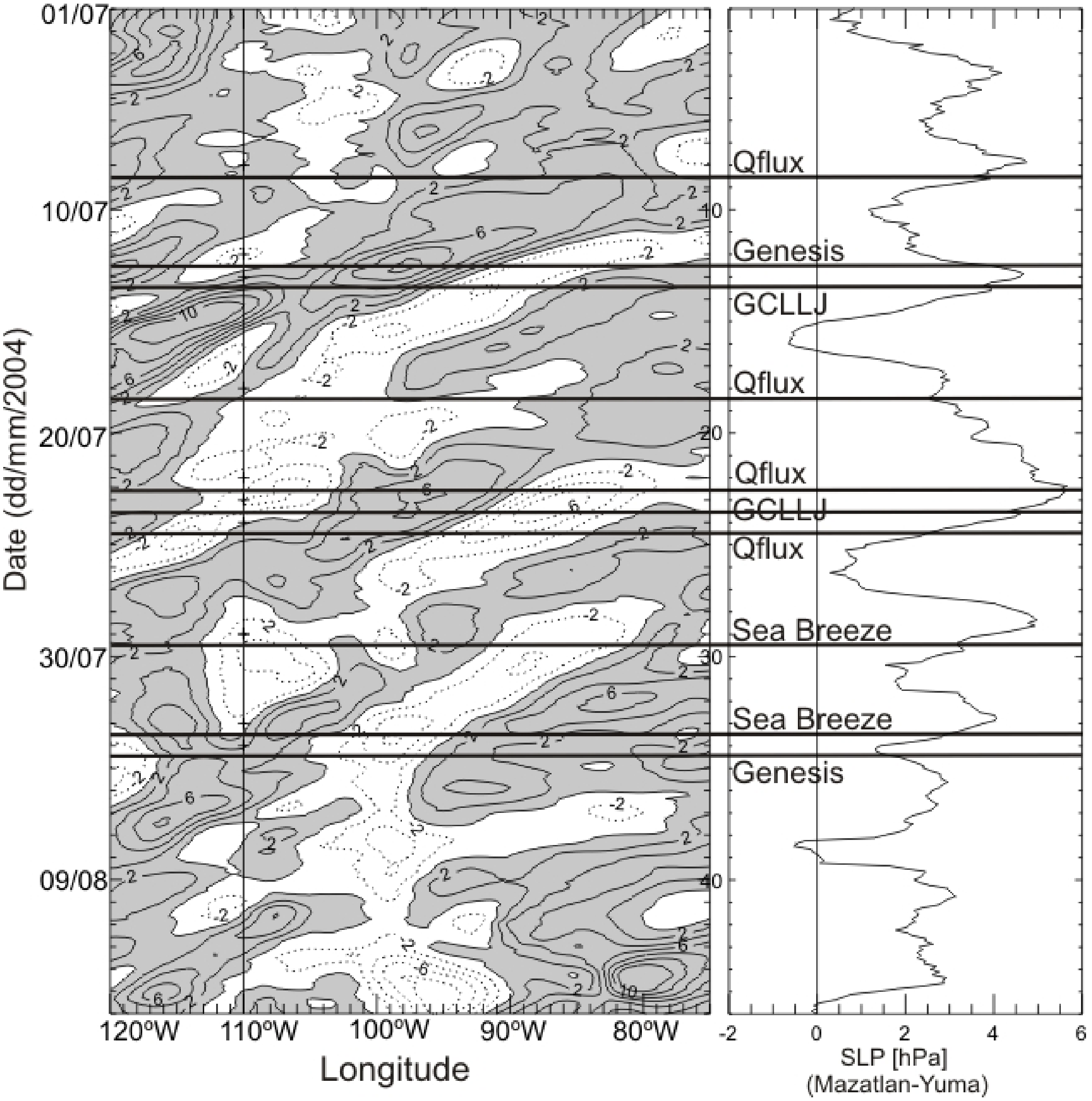

Figure 6. Longitude-time (Hovmoller) diagram (left) of mean daily 700 hPa meridional wind (m s^{-1}) along 22.5°N from NARR data (shading indicates southerly winds) and time series of sea-level pressure difference (right) between Mazatlan, Mexico (Mazatlan; Figure 5) and Yuma, AZ (KYUM; Figure 5). Horizontal lines show the date when the NOAA WP-3D aircraft missions were staged. Labels indicate the mission main objective: *Qflux* as previously defined; *Genesis* refers to moisture surge initiation; *GCLLJ* refers to missions designed to observed the LLJ with special legs in the northern GoC; *Sea Breeze* refers to missions with emphasis in observing the thermal circulations in the GoC eastern border and coastal plains.

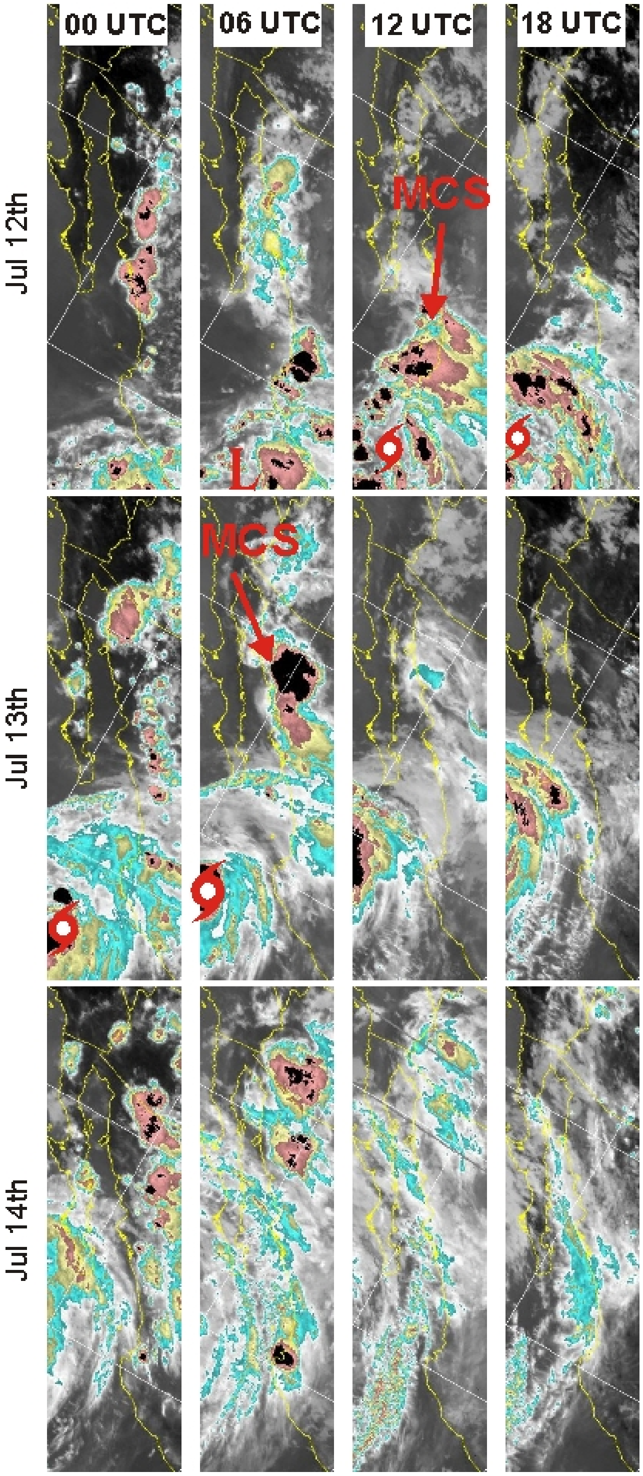

Figure 7. Infrared satellite imagery sequence from July 12 00UTC to 14 18UTC (From Earth Observation Laboratory data server http://data.eol.ucar.edu/). Tropical depression low center ("L") that later became TC Blas (marked with the Tropical Storm symbol) moved WNW right to the south of the GoC. Also notice the organized convection developing along the GoC during the night and early morning (00–12UTC) of each day, especially the MCSs that developed around July 12 at 12UTC and 13 at 06UTC.

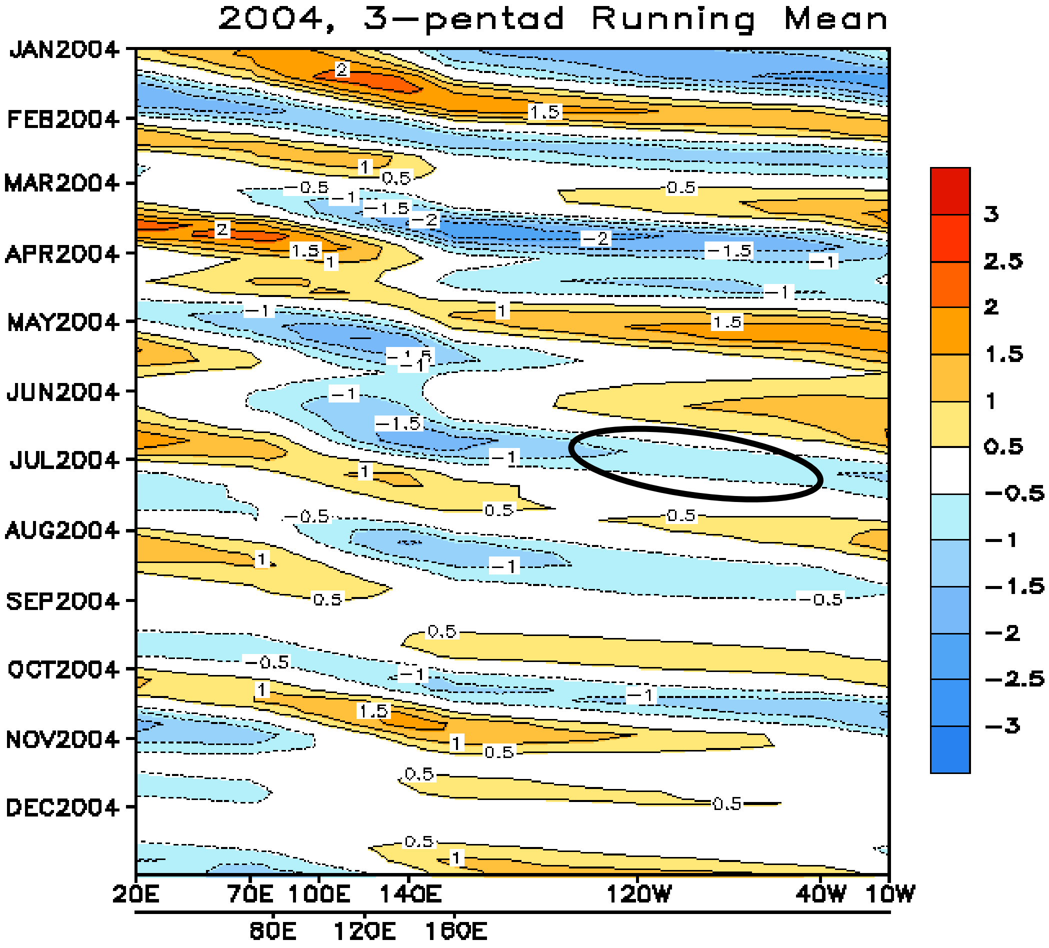

Figure 8. 200 hPa potential velocity CHI200 EEOF patterns during year 2004. Note July 12-15 surge occurred during an active phase of a moderate MJO-like feature. Figure adapted from the CPC weather and climate monitoring web site http://www.cpc.ncep.noaa.gov/products/precip/CWlink/daily_mjo_index/)

3.2 Analysis of Surface Stations for Surge of July 12-15

3.2.1 Overview

This section describes general propagation features for the surge of July 12-15, 2004 as observed from surface stations. The objectives are to document the propagation and spatial extent of the moisture surge and provide a basis for evaluating (in Section 3.3) the consistency of the surge's structure and propagating features using measurements from other observational platforms and theoretical approaches.

The surge analysis was based on the operational array of automatic surface stations shown in Figure 5 and Table 2.Most surface meteorological stations were installed in the last decade, with the exception of three stations from the NCAR Integrated Sounding System (ISS) array at Los Mochis (ISS4), Kino Bay (ISS3), and Puerto Peñasco (ISS2). These NCAR/ISS stations were implemented especially for NAME. Surface observations from Yuma (KYUM) clearly show the moisture surge event during IOP-2 (Figure 9a). They also show that the typical diurnal variation of surface quantities often is as large as the variability induced by the surge. Therefore, it is convenient to remove the diurnal cycle by using a 24-hr running mean. Furthermore, each station's mean for the period July 10–17 also was removed to facilitate comparison with other stations. The anomaly values for the surface temperature thus were calculated as $T' = T - \overline{T}$, where T is the surface temperature time series after removing the diurnal cycle and $\overline{T}$ indicates the average surface temperature during the period mentioned above. Figure 9b illustrates the effect of applying this procedure to the sea-level pressure (*SLP*), surface temperature (*T*), dew point temperature (*Td*), and the across-GoC and along-GoC surface wind components (*Urot*, *Vrot*) obtained after rotating the geographic coordinate systems 35° counterclockwise. We considered this axis rotation to facilitate the analysis, so that the zonal axis traverses the GoC perpendicularly (cross-GoC component), and the meridional axis coincides with the larger GoC axis (along-GoC component). The week-long changes in *SLP'* (~7hPa), *Td'* (~9 K), *T'* (~4 K), and *Vrot*' (NWly to SEly) indicate the persistence (~3 days) and magnitude of this surge event. However, observations from surface stations located along the GoC (e.g., Los Mochis, Figure 9c-d) can differ from the common surge characteristics illustrated by Yuma. Although the Los Mochis *SLP'* amplitude is nearly the same as at Yuma, the changes in *T'*, *Td'*, *Urot'*, and *Vrot'* are smaller. A critical issue is whether these differences are due to regional variations of the surge, or a response to dynamical processes that took place as the surge progressed northward.

An array of meteorological surface stations was selected along the Mexican Pacific coast and along the GoC coastal plain (see transect Figure 5) to document further the propagation and characteristics of the surge signature. The results are shown in

Figure 10. These stations were selected for their proximity to the coast and the absence of large topographic features nearby and lie close to transect A-B in Figure 5. To the south of the GoC entrance, this selection was relaxed since the SMO approaches the coast, including the relatively sharp coastal bend near Puerto Vallarta, (Jalisco, Mexico). Inspection of the airflow in this region indicated complicated variations that are mainly associated with the local orographic effects along the contorted coastline. The anomalies of the surface quantities shown in Figure 10 are calculated in the same manner as those shown in Figure 9.

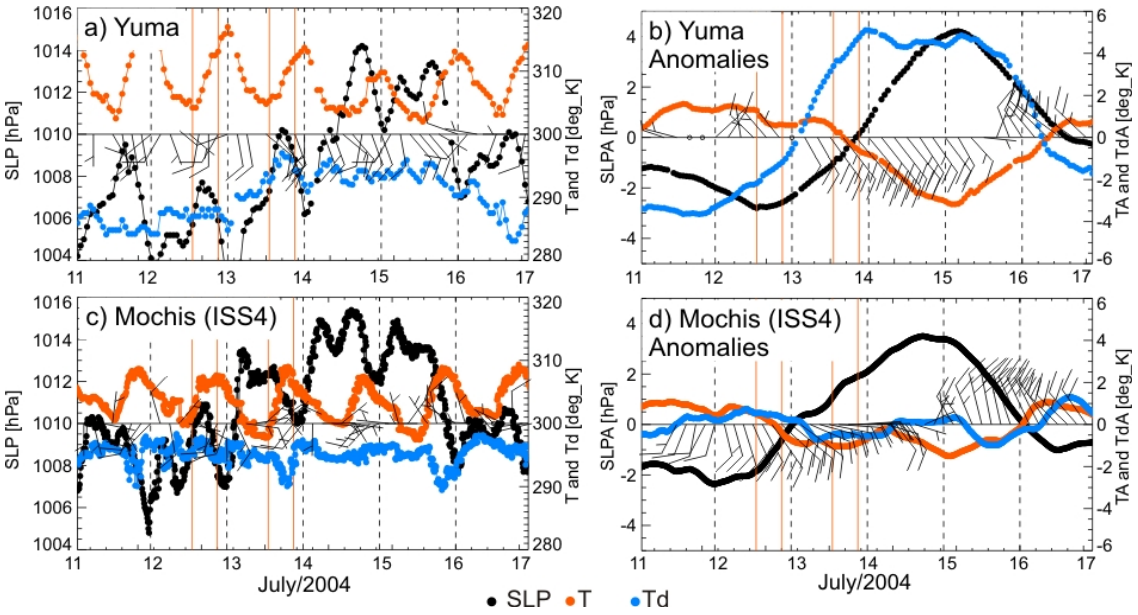

Figure 9. Meteogram (a) and anomaly values (b) for Yuma (KYUM), AZ, for July 10-17, 2004, with hourly sampling frequency. Panels (c) and (d) are the same as (a) and (b) but for Los Mochis (ISS4), Mexico, with 10-min sampling frequency. Anomalies are calculated with respect to the mean quantities observed for July 10-17 after removing diurnal cycles using 24-hr means (see text). Black circles indicate sea-level pressure, orange corresponds to surface temperature, and blue to dew point temperature. Wind barbs are plotted every 3 hours to avoid cluttering and follow the standard convention (half a barb indicates an actual/anomaly wind speed of 5 knots, a full barb 10 knots, while the staff shows anomaly wind direction), while wind anomalies are amplified by a factor of five. Pairs of solid orange vertical lines enclose the NOAA WP-3D missions for time reference. Dashed vertical lines indicate 00UTC for each day.

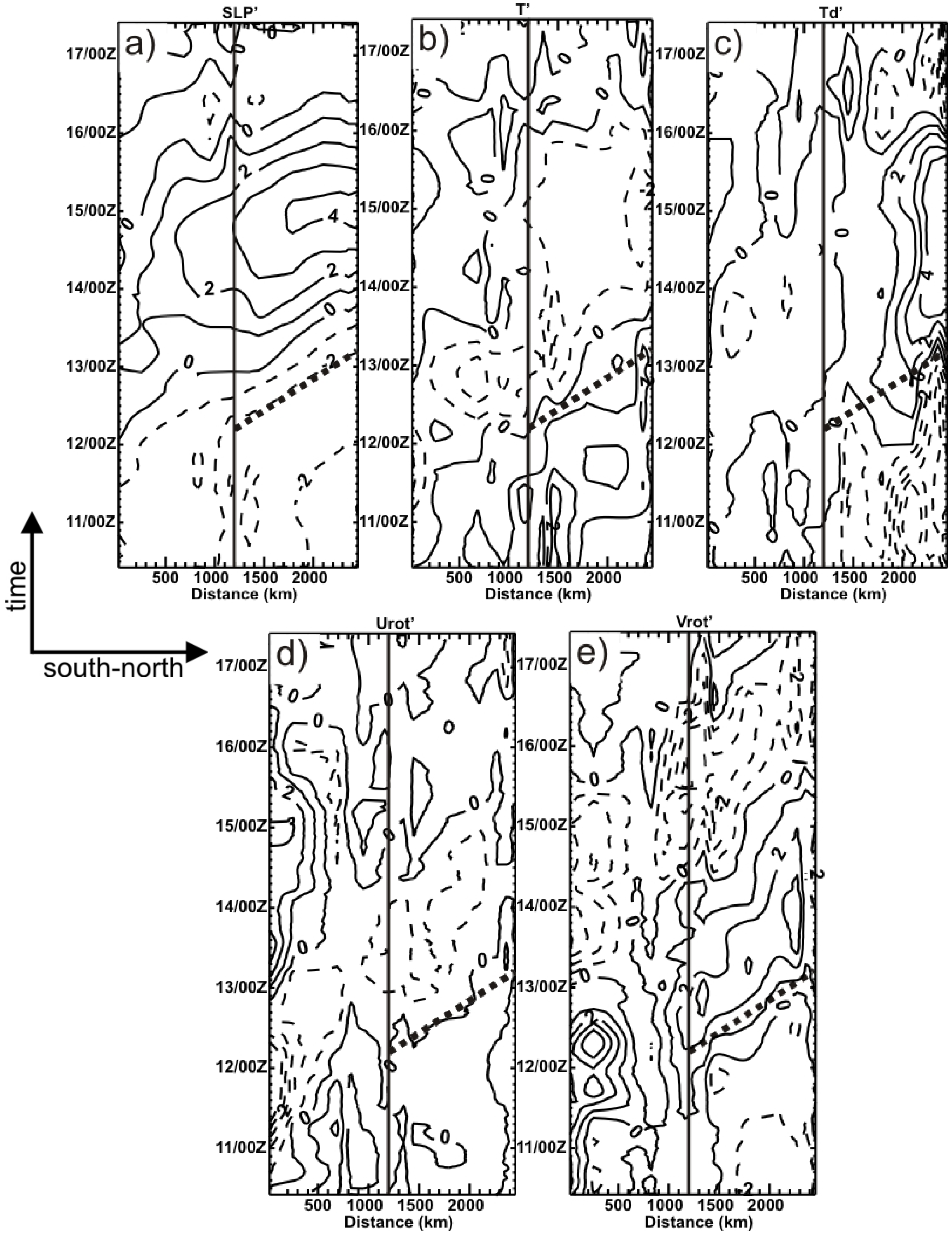

Figure 10. Time sequence (10-17July, 2004) versus south-to-north distance alongshore (transect A-B shown in Figure 5) for anomalies of: a) sea level pressure (hPa), b) temperature (ºK), c) dew point temperature (ºK), d) cross-Gulf surface wind (ms^{-1}), and e) along-Gulf surface wind (ms^{-1}). Solid (dashed) contours are indicate positive (negative) perturbations. Heavy dotted line shows the surge initiation based on its pressure signal as it progresses northward along the Gulf coastal plains. Vertical solid line shows position of GoC entrance.

3.2.2 Pre-surge conditions (10-12 July)

The pre-surge conditions show negative *SLP'* along the southern GoC and southwestern Mexico with larger negative anomalies over the northern GoC and SW USA (Figure 10a). Relatively warm ($T'>0$) and dry ($Td'<0$) surface environments prevailed over the GoC coastal plains before the surge onset in the northern Gulf (July 13) (Figure 10b), conditions that also were associated with weak northwesterly wind anomalies ($Vrot'<0$) (Figure 10b-d). To the south of the GoC, the pre-surge conditions are similar, with the main difference being that the dew points are about 1ºK higher than after the surge onset. The pre-surge pattern along the GoC agrees well with those climatological pre-surge conditions found in the surge compositing studies of Douglas and Leal (2003) and Higgins and Shi (2005).

3.2.3 Moisture Surge Evolution (13-15 July)

The most important feature observed in Figure 10 is the northward along-Gulf progression of the surge. This pattern suggests that *SLP'* changes occur in a rather smooth fashion compared to the sudden changes usually observed in gravity current-like disturbances (Koch et al., 1991; Haertel et al., 2001). In general, the phase changes occurring among *SLP'*, *T'*, and *Td'* (Figure 10a-c) also suggest that hydrostatic adjustment induced by the relatively cold air incursion, assuming a linear response of the lower atmosphere, is taking place as the surge progresses. A more thorough analysis of the cause and effect of these changes will be discussed later in this chapter. In contrast to this phase progression, *Vrot'* (Figure 10d) inside the GoC shows that southerly winds began about 6-8 hrs earlier than the surge characterisitic observed for SLP'.

A number of important aspects of Figure 10 now are discussed in more detail:

a) <u>Sea level pressure anomaly</u> (*SLP*'): The *SLP*' time sequence shows a relatively smooth along-Gulf northeastward progression of the surge (Figure 10a). The *SLP*' amplitude increases as the surge progresses northward. Over the northern GoC and southern Arizona, the pressure increases by nearly 7.5hPa (from -3hPa before the surge onset to +4.5hPa around 00UTC on July 15) compared to just 5hPa amplitude observed at the GoC entrance. At the GoC entrance, *SLP'* started increasing at 10UTC on July 12, reaching the northern end of the GoC at 02UTC on July 13, which implies a propagation speed of 17.7 m s^{-1}. Two different aspects suggest that this moisture surge was indeed a propagating phenomenon: first, during the surge leading edge passage, low-level winds remained below 17.7 m s^{-1} (Rogers and Johnson, 2006); and secondly, the propagation speed of the surge was unrelated to the motion of TS Blas, whose translation averaged only 10 m s^{-1}. Using high time resolution wind profiler data gathered during this event, Rogers and Johnson (2006) inferred the propagation speed of the surge by following the wind gust signature of the surge leading edge. They estimated that from Los Mochis to Kino Bay and from Kino Bay to Puerto Peñasco (Figure 5) the surge accelerated from 17 m s^{-1} to 22 m s^{-1}, respectively. Different processes have been identify to contribute to the alongshore acceleration of a moisture surge and will be discussed in Section 3.3.

b) Surface temperature anomaly (*T'*): During the surge passage, *T'* indicates relatively cool conditions (Figure 10b) that are noisier than those for *SLP'* (Figure 10a). Some dynamical modes that propagate along the stable layer above the marine boundary layer (MBL), such as linear Kelvin waves, often show slight temperature changes at the surface (Ralph et al., 2000; Zehnder, 2004). However, regardless of the surge dynamics, inland anomalous temperatures should be detected due to heat and momentum mixing within the boundary layer. At the GoC entrance, relatively abrupt cooling is observed just before the surge initiation (10UTC on July 12), probably associated with convective outflows from previous storms as observed from IR images (see Figure 7). This feature will be analyzed in much more detail in Section 3.3. Strong cooling also is observed between Puerto Peñasco and Yuma during the surge passage, with a minimum anomaly (~ -3ºK) around 00UTC on July 15, associated with enhanced southeasterly winds shown in Figure 10e.

c) Surface dew point anomalies (*Td'*): positive *Td'* are observed in the central GoC before the surge passage (18UTC on July 11, Figure 10c). The origin of these spikes in *Td'*, associated with a decrease in *T'*, still is to be determined; convective activity taking place along the western flank of the SMO and the coastal plains also are associated with this relatively sudden increase in dew point before the surge initiation. In contrast with *T'* and *SLP'*, the northern gulf and low desert experiances impressive changes of *Td'*, varying from anomalies of -3ºK during the pre-surge condition to around 8ºK maximum near 00UTC on July 15. This increase in *Td'* occurs within a 24-hour period. The amplitude of *Td'* during the surge passage decreases southward from about 3ºK over the central GoC to near zero at the GoC entrance.

d) Surface wind anomalies (*Urot'* and *Vrot'*): The alongshore progression of the disturbance shows larger changes in the along-shore wind component (*Vrot'*) compared to the cross-shore wind component (*Urot'*) (Figure 10d, e). Variation in *Vrot'* occurred about 6-8 hrs before the pressure and temperature changes took place. The enhanced southeasterly winds also show two distinctive local patterns (Figure 10e). The first, located at the lower GoC (starting at 08UTC on July 12) probably was induced by the strong organized convection that shows maximum reflectivity and development between 06-10UTC on July 12 offshore of Puerto Vallarta, Mexico (Figure 7). A second alongshore maximum, over Puerto Peñasco extending from 08UTC on July 13 to 00UTC on July 14, was associated with the enhancement of the low-level jet also observed by the NOAA WP-3D aircraft (Higgins at al., 2006) and ISS wind profiler (Rogers and Johnson, 2006). Figure 10d shows enhanced offshore surface flow anomalies during the surge lifetime. Anderson at al.'s (2001) numerical simulations have shown that the surges affect diurnal circulations along the GoC coastal plains. Specifically, they showed that under surge forcing conditions (with a superimposed alongshore pressure gradient) the onshore and upslope winds are expected to be weaker during the daylight, while stronger downslope and offshore flow is expected at night. Although these changes in the diurnal circulation may produce the enhanced offshore flow shown in Figure 10d, some other factors may also contribute to this circulation response, such as those associated with synoptic changes or enhanced convective activity over the SMO foothills.

Sections 3.4 and 3.5 will present some evidence of the changes in the diurnal circulations associated with the surge passage.

3.3 Nature of the Moisture Surge Leading Edge indicated by Aircraft Observations for Surge of July 12-15

The NOAA WP-3D aircraft data reveal the horizontal and vertical structure of the initiation of the July 12-15 surge, which is believed to be associated with the TS Blas circulation and convective activity to the south of the GoC entrance. Aircraft data analyses (Figure 11, 10) bring an offshore perspective that complements, with much higher spatial detail, the above analysis that was based on surface stations and data obtained from other platforms such as wind profilers (Rogers and Johnson, 2006). The aircraft also provides observations relatively far from local effects due to surface processes along the coast or inland, but with the limitation that the data offer only snapshots of the surge propagation.

Figure 11 shows the 950 hPa level analysis using flight-level aircraft observations, while Figure 12 shows the along-GoC cross-section for the transect shown in Figure 11. Two distinctive features are observed, presumably associated with the moisture surge leading edge. The first feature consists of strong potential temperature and wind speed gradients near the GoC entrance below 900hPa (captured by S1 line in Figure 12) that resemble a gravity current (GC) (Simpson, 1987; Haertel et al., 2001). The second structure consists of a much and deeper (750-950 hPa) potential temperature and mixing ratio decreases downwind of the former feature (S2 line in Figure 12). The upward vertical displacements of the isentropes within the MBL inversion, and co-located wind shift and enhanced southeasterly wind, suggest that this feature resembles a wave propagating above the MBL such an Linear Kelvin Wave (LKW), Solitary Kelvin Wave (SKW), or an internal atmospheric bore (Ralph et al., 2000). Some interesting questions that arise include: to what extent are these features part of the leading edge of the moisture surge signal analyzed in previous sections? What is the best dynamical theory to explain surges and what are their triggering mechanisms? Although it is not intended to be an exhaustive analysis in fluid dynamics, the focus next is to elucidate the main characteristics of the moisture surge leading edge (in relation to S1 and S2) to the extent possible, using the mix of observations obtained during this event.

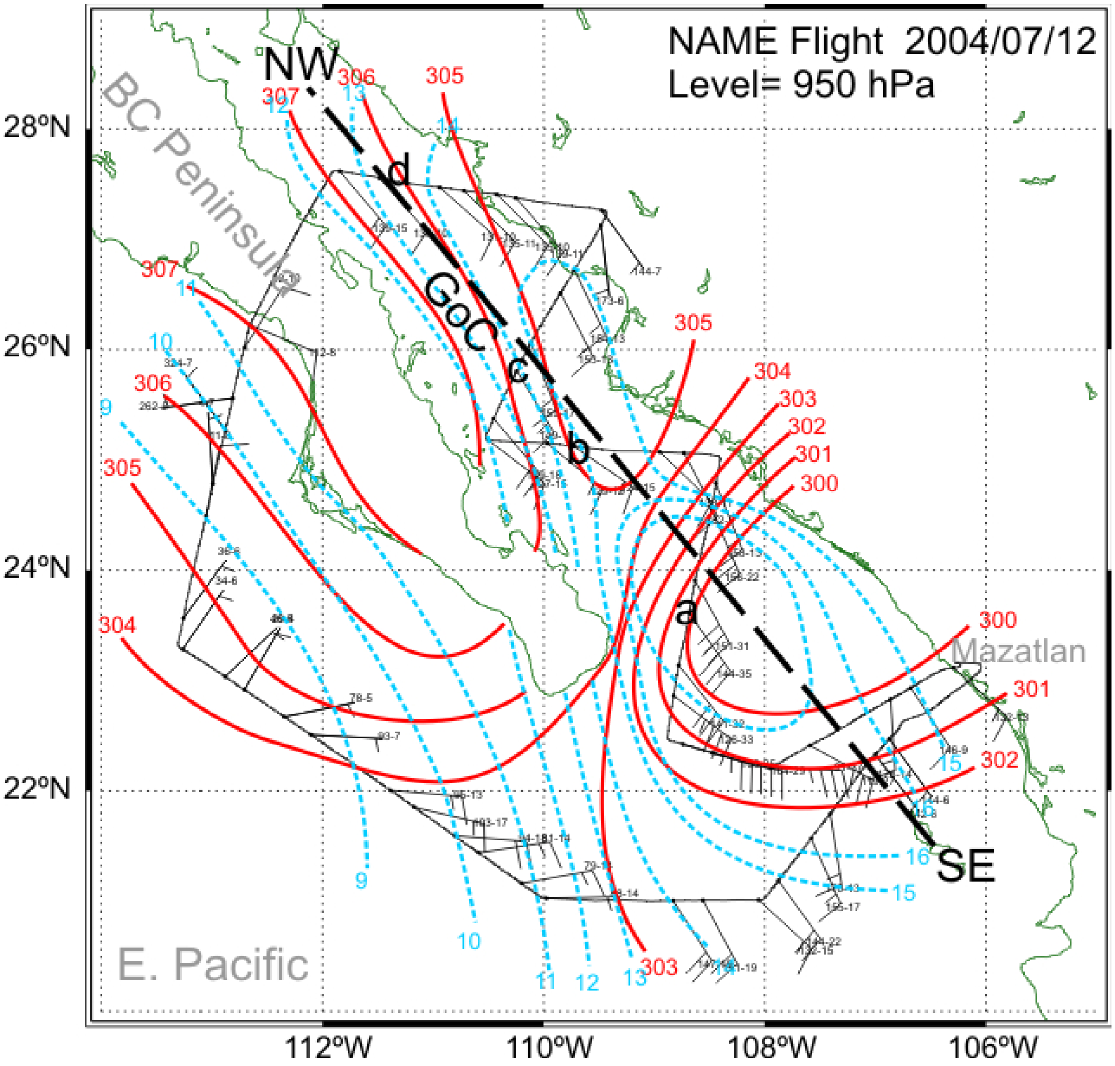

Figure 11. Temperature, mixing ratio, and wind analyses at 950 hPa level for NOAA WP-3D flight (1330-2000 UTC) on July 12. Isentropes (red solid lines) are plotted every 1°K and lines of equal mixing ratio (blue dashed lines) are plotted every 1 g Kg^{-1}. Wind barbs (full barb 10 kt and half barb 5kt) are plotted along the flight track (thin solid line) every time the aircraft crossed the 950hPa level (within +/-3hPa). Thick dashed line shows the location for the vertical cross-section analysis shown in Figure 12. Letters a, b, c, and d show the location of soundings shown in Figure 14b. The flight started from Mazatlan, Mexico, at 1330UTC flying the across-GoC legs and ended after the Pacific Ocean transects at 2000UTC. Notice the relatively strong southeasterly wind associated with relatively moist and cool air over the GoC entrance.

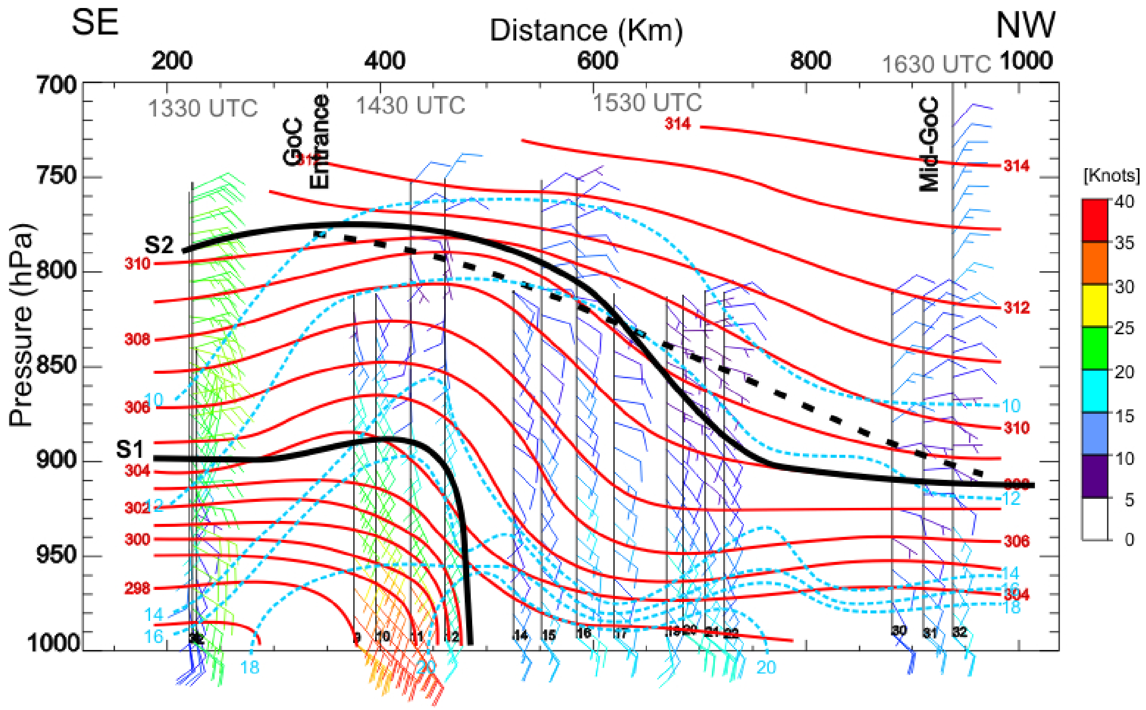

Figure 12. NOAA WP-3D July 12 along-GoC vertical cross-section for transect in Figure 11. The soundings included are those located within 20km of this transect line. From beginning to end the transect was covered in about 3 hours (1330UTC to 1630UTC). Isentropes (red solid lines) are plotted every 1°K and lines of equal mixing ratio (blue dashed lines) are plotted every 2 g Kg^{-1}. Wind barbs (full barb 10kt and half a barb 5kt) are colored coded to indicate the relative wind magnitude (speed increases from blue to red). Thick black solid lines show S1 (convective outflow) and S2 (Kelvin wave, solitary wave, or bore) mentioned in the text. Black dashed line delineates the level of directional wind shear associated with S1.

Structure 1 at the Gulf Entrance (S1)

Some convective outflows have been characterized as GCs (Klemp et al, 1994; Haertel et al., 2001), which consist primarily of airflow generated by density gradients and involve the advection of dense, colder air through mass transport. In this case, thunderstorms observed on July 12 between 06-12UTC offshore of Nayarit, Mexico (Figure 7), could have produced such an outflow. Convective storms detected by the NAME Radar network (Figure 13) are co-located with the leading edge of the S1. Figure 11 and 10 show evidence of an abrupt temperature drop and a sharp increase of wind speed that coincides with the location of the convection at 1415UTC/July 12 (Figure 13). Sustained winds of 18-20 m s^{-1} were observed at the S1 front with observed mean background flow ahead of the S1 between 5-6 m s^{-1} (at 500m), which suggests a propagation speed of 13-14 m s^{-1}. By following the convective activity using the radar reflectivity in Figure 13, a coherent signal can be tracked for about 5 hours (from 0915-1415UTC). For concise display purposes, Figure 13 shows hourly radar imagery. However, an animation of the radar imagery's full time resolution (data every 15 minutes) was used in order to track the high reflectivity features (not shown). If the convective activity is assumed to be produced at the leading edge of the S1 then its propagation speed is 14.1 m s^{-1}. Analytically, if S1 is indeed a GC, assuming steady-state GC theory, the phase speed can be estimated using (Heartel at al., 2001)

$$C_{gc} = \kappa\sqrt{gh\left(\frac{\rho_c - \rho_w}{\rho_w}\right)} \qquad (3.1),$$

where ρ_c and ρ_w are respectively the air densities of the cold and warm side (treated as constant in each layer), g is the acceleration due to gravity, h is the depth of the cold flow, and κ is a proportionality constant. Atmospheric gravity current theory indicates a $\kappa = (2)^{1/2}$ (Von Karman, 1940), while observational studies, as reviewed by Heartel at al. (2001), show empirical values of κ ranging from 0.4 to 1.25. Some of the differences between theory and observational studies may be due to treatment of frictional and mixing processes. It is assumed as 1 for practical purposes. From the aircraft observations we find θ_c = 299.5 ºK and θ_w = 305ºK at 550 m (~950hPa), which can be used to estimate the density, and h = 850 m. This yields a phase speed of 12.4 m s^{-1}, which is consistent with those measured using aircraft and radar reflectivity observations. Thus, the evidence clearly suggests that was indeed a GC.

There are several problems with assuming that a GC (S1) was the main dynamical mechanism of this moisture surge along the GoC. As mentioned by Zehnder (2004), the horizontal extent of such features is constrained by geostrophic adjustment with time scales $1/f_o$ ~ 4 hrs, where f_o is the Coriolis parameter. The horizontal extent of this feature (see Figure 11) already shows weakening of the wind and temperature features by the time of the aircraft's return legs 6.5 hr later. Furthermore, the expected hydrostatic pressure perturbation associated with this type of disturbance can be estimated as

$\Delta P \approx \rho_w C_{gc}^2$ (Zehnder, 2004), leading to a 1.6 hPa sea level pressure rise. The total pressure change (synoptic- and surged-induced) registered from surface stations along the coastal plain was about 7 hPa (over a 48 hour period), which indicates that a GC would not alone account for such a perturbation pressure amplitude. This GC feature also is about 100hPa deep, rather shallow compared to the depth of the perturbed signals according to the upper-air composites shown below (Section 3.5). Thus, the GC structure (S1) by itself is not capable of producing the surge signal as observed along the GoC and extending into the SW United States (Figure 10). In addition, the filtered surge signal, as observed from stations in Figure 9, shows that the overall surge changes in wind, temperature, and pressure are relatively gradual and propagating too fast (about 17.7 m s^{-1}, Section 3.2) to be considered as resulting from a GC.

Structure 2 at the Gulf Entrance (S2)

Details of the aircraft observations reveal a second feature (S2, Figure 12) that extends about 200 km downwind of the GC (S1, Figure 12). We now compare the theory for different dynamical mechanisms that possibly are relevant for S2, such as an LKW, SKW, or internal bore (Zehnder, 2004; Rogers and Johnson, 2007). To more quantitatively illustrate the vertical structure of the surge leading edge, the similarities and differences between the observations and these possible dynamical mechanisms are described.

The existence of TS Blas to the south of the Gulf entrance suggests the possible evolution of a LKW due to an unbalanced gradient wind produced when the low-level cyclonic flow interacts with the topography (Gill, 1982; Zehnder, 2004). Zehnder (2004) performed numerical simulations for simplified two-layer flow that explain, with some limitations, the evolution of an LKW along an idealized topographic barrier that emulates the effect of the SMO and the Baja California peninsula. He concluded that some features are not in qualitative agreement and only the transformation from a

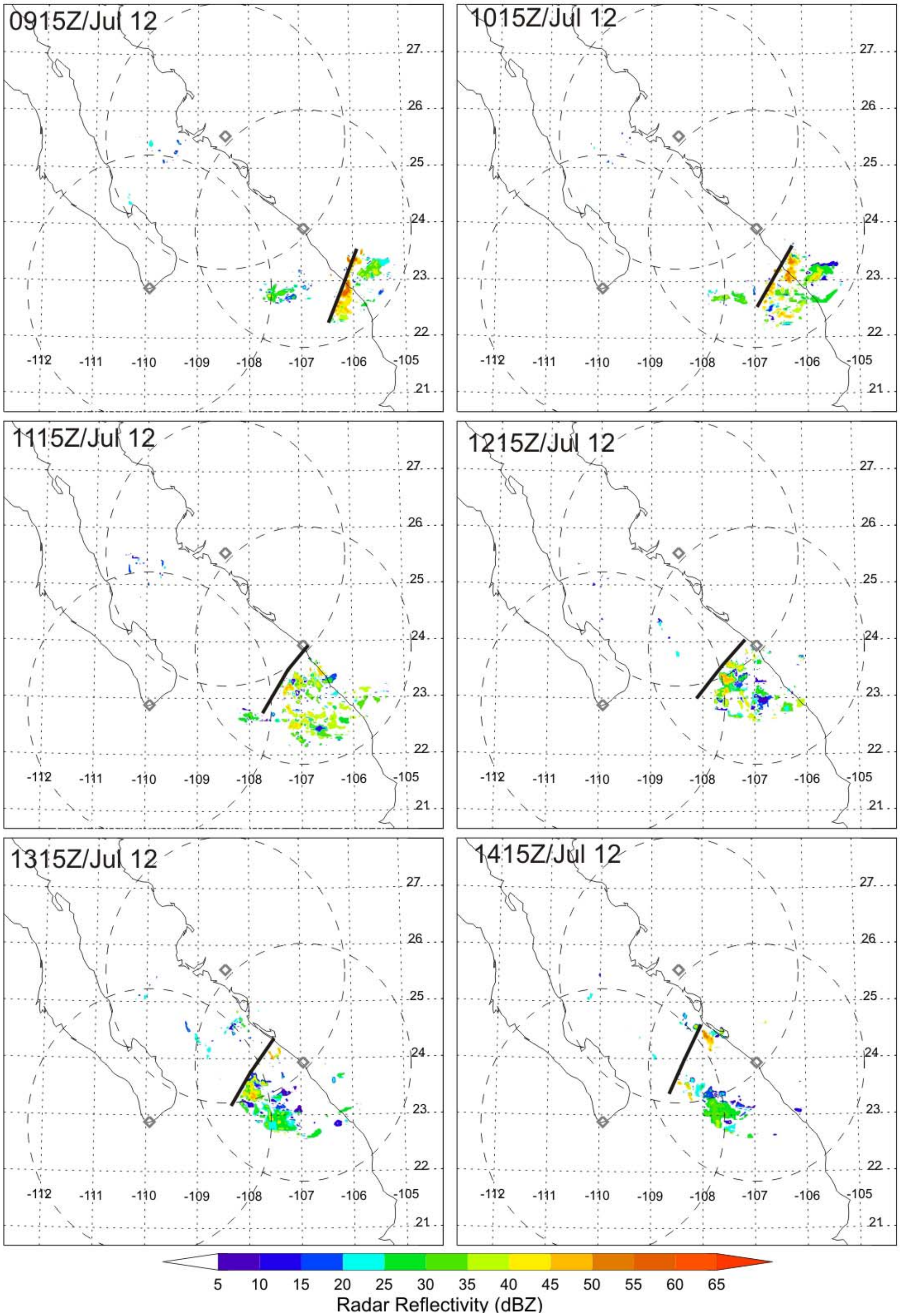

Figure 13. Gridded (2 Km) composite of near-surface radar reflectivity (dBz) from NAME radar network. The solid line in each panel shows the hourly propagation of the leading edge of the convection associated with what was concluded to be a gravity current.

LKW to a nonlinear Kelvin wave or internal bore, changes induced by nonlinear processes over the MBL, may produce the expected transport of moisture that typically characterizes the moisture surges. Internal bores can be formed from GCs when the static stability is high near the surface and the gust front forces the stable air upwards. Knupp (2006) and other studies have observed internal bore disturbances that evolved from GCs produced by thunderstorm outflows when propagating over a suitably stable surface layer. Evidence of long lifetime and large amplitude bores that travel hundreds of kilometers also has been found in observational studies (Koch et al. 1991) and is supported by fluid dynamics theory (Klemp et al., 1997).

Figure 14a, b show the cooling above the MBL from soundings at Los Mochis, Sinaloa, and from aircraft soundings (c and d in Figure 11), respectively. The Los Mochis (ISS4) sounding shows low-level warming (from 11UTC to 18UTC July 12) due to radiative heating and mixing, while the GoC aircraft soundings (obtained around 15 UTC July 12) show unperturbed conditions below the MBL capping inversion layer. Figure 14a, b shows that the perturbed flow, which experiences abrupt cooling, propagates above the stable MBL, at least over the GoC, with a maximum depth that extends up to 2500 m ASL (750 hPa). The average height of the SMO (~700 hPa) may control the maximum extent of trapped wave disturbances. Ahead of S2, the winds have an easterly-northeasterly component (nearly calm, 1-2 m s^{-1}), whereas beneath S2, the winds have a southeasterly component with a modest increase in wind speed (see Figure 12). At 850 hPa, ahead (behind) of this feature, the mixing ratio is 10 g kg^{-1} (14 g kg^{-1}) and potential temperature of 311 ºK (307 ºK).

The intrinsic phase speed relationships for different wave forms can be obtained through the correct manipulation of the shallow-water equation (SWE) of motion, including appropriate boundary conditions, and using nonlinear semigeostrophic theory. In order to obtain these phase speed relationships, it was assumed that the hydrostatic approximation holds and that any synoptic forcing is negligible, among other minor considerations. The background synoptic forcing may be important and we acknowledge that the complexity of the GoC geometry and the overall moisture surge structure in principle may require these and some other additional considerations, such as accounting for the strong thermal variability found along the GoC coast and frictional effects. Despite these limitations, a simplified three-layer system was considered (Figure 15), similar to the one applied in Ralph et al. (2000) for coastally-trapped wind reversals along the United States Pacific coast. The three layers in Figure 15 consist of an undisturbed MBL of depth *h*, the MBL inversion of thickness h_1 through which the perturbation (of depth h_2) propagates, and the free troposphere on top. It should be mentioned that the background flow through which the present surge is propagating supports the assumptions made by the classical hydraulic theory in terms of the existence of a relatively strong MBL inversion, which exists over the GoC (Figure 14b). However, the geometry of the GoC differs from that of the US west coast. Instead of a having a vertical wall providing Coriolis trapping, the surge propagates over complex terrain around the GoC (Figure 2), including the SMO with internal valleys, a relatively wide coastal plain to the west of the SMO (~30-50 km), and the Baja California peninsula.

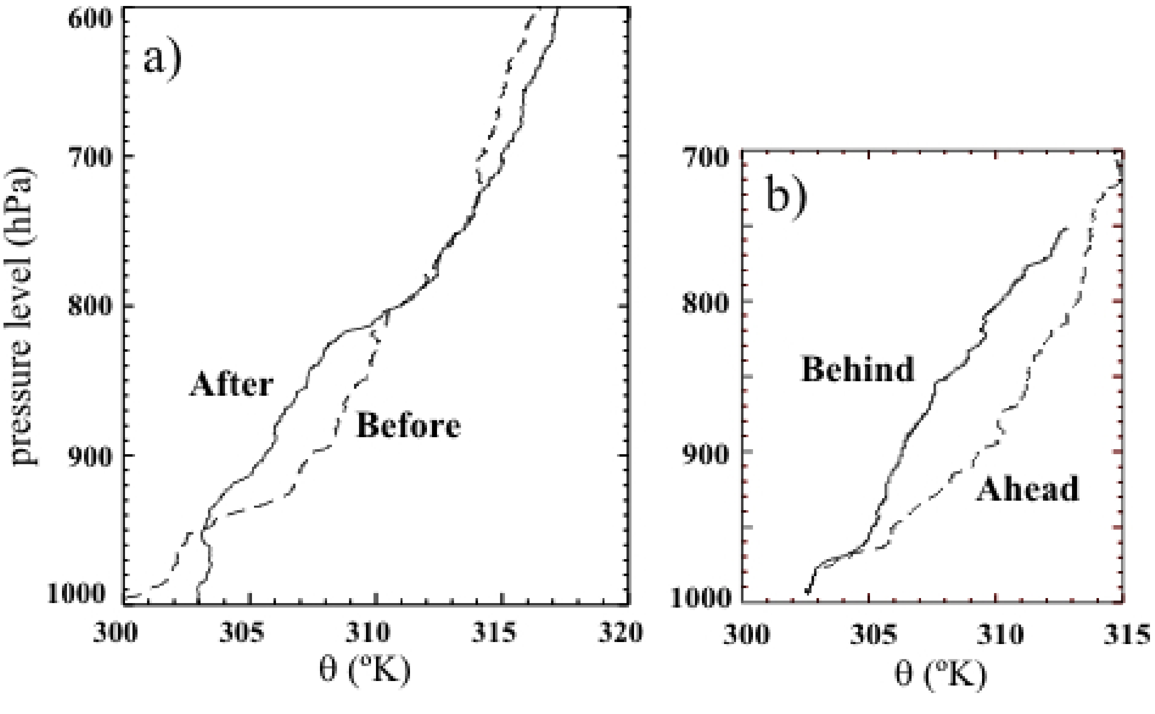

Figure 14. a) Potential temperature (θ) profiles from Los Mochis ISS4 at 11UTC July 12 before the surge passage (dashed line), and 18UTC July 12 after the surge passage (solid line). b) NOAA WP-3D flight level θ for profiles behind (solid line) and ahead (dashed line) of the perturbation leading edge, obtained around 15UTC July 12. See sounding locations in Figure 11; both aircraft soundings where obtained within an hour of each other.

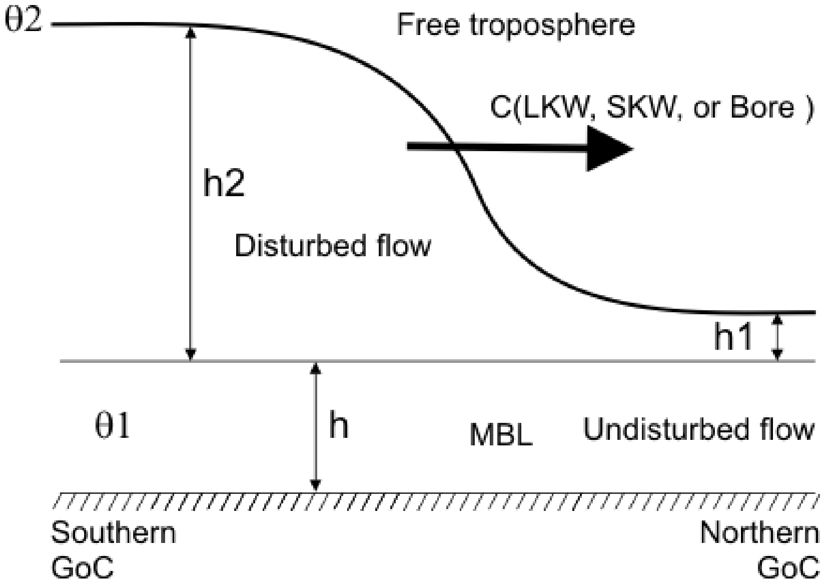

Figure 15. Idealization of the structure 2 (S2, Figure 12) observed during the NOAA WP-3D on July 12 mission. The structure is moving towards the northern end of the Gulf with a phase speed *C*. θ_1 is the average potential temperature (θ) of the MBL and θ_2 the potential temperature at the inversion top. h, h1, and h2 are the depths of the MBL, the undisturbed MBL inversion and the disturbed MBL inversion, respectively. Figure is adapted from Ralph et al. (2000).

As shown in Ralph et al. (2000), appropriate phase speed (*C*) relationships, for the given two-dimensional geometry and flow condition in Figure 15, can be expressed for LKW, SKW and bore as

$$C_{LKW} = \sqrt{g'(h + h_1)} \tag{3.2a}$$

$$C_{SKW} = \sqrt{g'(h + h_2)} \tag{3.2b}$$

$$C_{bore} = \sqrt{2g'\left(\frac{(h + h_1)^2}{2h + h_1 + h_2}\right)} \qquad \text{(3.2c)},$$

where g' is the reduced gravity defined as $g(\theta_2 - \theta_1)/\theta_2$; h, h_1 and h_2 are the depth of the MBL, the undisturbed MBL inversion, and the disturbed MBL inversion layers, respectively; θ_1 is the average potential temperature of the MBL, assumed to be well mixed; and θ_2 the temperature at the inversion top.

Selection of an adequate value of each parameter needed in (Eq. 4.2) is a difficult task and involves subjective interpretation of the isentropic analyses shown in Figure 12. However, it is believed that the aircraft observations of the disturbance's leading edge bring sufficiently high spatial resolution to provide an adequate test of the theory. The analysis shown in Figure 14 indicates that only the MBL inversion responds to the disturbance, because h disappears since MBL top acts as a rigid bottom. Furthermore, the thickness of the undisturbed flow (h_1) was considered to be from 500 to 700 m in order to include the 308K and 310K isentropes (θ_2) that better mark the top of the perturbed environment (Figure 12). The thickness of the perturbed enviroments (h_2), measured from the top of the MBL, ranges from 1700 to 2000 m.

Table 3. Predicted phase speed for S2 during July 12 surge event based on WP-3D aircraft observations. C is the phase speed of the propagating structure using linear Kelvin wave (LKW), solitary Kelvin wave (SKW), and bore model theory (Eq. 4.2a-c). C is the mean phase speed obtained after considering a range of uncertainty in adequately selecting the parameters in Eq. 4.2; the range of uncertainty of these calculations also is provided. U is the southeasterly component of the horizontal wind of the base state.

Type of disturbance	C m s^{-1}	*C range of uncertainty* m s^{-1}	C+U m s^{-1}
LKW	10.4	1.0	12.4
SKW	18.6	1.1	20.6
Bore	22.9	1.4	24.9

Table 3 shows the results of applying Eq. 2. It includes ranges of uncertainty for C that correspond to uncertainties in h (0), h_1 (500-700 m), h_2 (1700-2000 m), θ_1 (303K), and θ_2 (308-310K), due to possible error in the observational analysis, the across-gulf location of the perturbation, and measurements errors (relatively small compared to the others). The range of uncertainty in C does not include errors in the interpretation of the phenomenon and does not consider the theoretical simplifications and assumptions made to obtain Eq. 4.2. However, these uncertainties can be accounted for by assuming an uniform base state of the flow along the GoC. In this respect, the horizontal wind velocity of the basic state (*U*) can be obtained by averaging the aircraft soundings ahead of the S2 from 700 to 3000m, and then adding the results to the predicted phase speed obtained using Eq. 4.2. On average, the undisturbed flow above the MBL is characterized by weak southeasterly winds with speeds ranging from 1-2 m s^{-1}.

From Table 3, it is apparent that the calculated phase speed of the disturbance predicted by the SKW theory (20.6 m s^{-1}) compares most favorably with the moisture surge phase speed obtained above from the surface pressure disturbance traces (17.7 m s^{-1}). The latter constitutes an average phase speed after removing diurnal variability effects from the surface pressure traces. On the other hand, the LKW phase speed relationship (12.4 m s^{-1}) and bore (24.9 m s^{-1}) models under-predict and over-predict the observational estimates, respectively. The range of uncertainty in estimating the phase speed by subjectively selecting parameters for Eq. 4.2 also is shown in Table 3, and is less that 10% of the estimated phase speeds for all of the models.

Based on the NAME wind profiler array data (Los Mochis, Bahia Kino, Puerto Peñasco), Rogers and Johnson (2007) reported an increasing phase speed as this surge event progressed northward by following the surge's wind signal, ranging from 17 m s^{-1} from (Los Mochis to Bahia Kino) to 22 m s^{-1} (Bahia Kino to Puerto Peñasco) and suggested that the surge leading edge more likely resembled a borelike structure. Among other plausible mechanisms, the acceleration of the surge as it progressed northward may be explained by: (*i*) those mechanisms associated with the dynamical mode of the propagating disturbance, for example the nonlinear evolution (inertial-advection) of a linear Kelvin wave into a bore-like disturbance (Klemp et al., 1997; Ralph et al., 2000; Zenhder, 2004; Knupp, 2006); (*ii*) those mechanisms associated with the across-gulf thermal contrast producing an onshore pressure gradient force (PGF) during the day that tends to slow down the southeasterly flow, while an offshore PGF during the nighttime geostrophically accelerates it (Douglas, 1995; Stensrud et al., 1997; Anderson et al., 2000a; Fawcett at al. 2002); (*iii*) large-scale pressure changes that enhance the alongshore ageostrophic downgradient flow; or (*iv*) any combination of the above. As mentioned before, the appropiate background conditions exit to support the propagation of the solitary wave along the entire extent of the GoC. SKWs and bores could propagate for a considerable distance under background conditions that prevent vertical energy loss in the GoC system (Klemp et al., 1997). Since the amplitude of the solitary wave is large compared to the lower layer, it is plausible that explanation (*i*) operated to produce the solitary wave leading edge steepening into a bore-like leading edge. However, for this conversion to occur, we still need to assume that the nonlinear effects that tend to steepen the wave are not effectively balanced by the dispersive effects that tend to flatten the wave (Reason and Steyn, 1992).

The synthesis of these unprecedented observations reveals two propagating wave structures associated with the 12-15 July moisture surge leading edge. The GC (S1) is initiated by a convective outflow induced by the MCS system located to the south of the Gulf entrance (see Figure 7, MCS 12 UTC July 12). Although it is not plausible that this GC could propagate the entire length of the GoC, it may have initiated the SKW (S2). There are many reports of SKWs and bores being induced by existing or dissipating GC that penetrate the lower stable layer (Christie et al., 1979; Schreffler, and Binowski, 1981; Simpson, 1987; Christie, 1989; Koch et al., 1991; Haertel, et al, 2001). Once the SKW is generated by the GC it can propagate even after the GC decays (Christie 1989). The analysis presented herein indicates that the timing, phase speed, and vertical structure of the SKW resembles those of the moisture surge leading edge observed along the GoC. Thus, if the SKW is purely initiated by the GC, which in turn was generated by convective outflows, then we are able to connect the surge onset to the presence of MCSs in the southern GoC. On the other hand, synoptic forcing may be directly responsible for the SKW. The passage of the TEW and its associated low-level cyclonic disturbance, rotating about 800km to the south of the Gulf entrance at 12UTC on July 12 (section 3.1), could force a barrier wave (Zehnder, 2004) by disrupting the gradient wind balance due to the proximity of the low center to the SMO. This scenario is plausible given the timing and location of this low-level disturbance. The lack of observations in the region where the low-level disturbance occurred prevented testing of whether the unbalanced flow forced the SKW. However, we can perform this task by using numerical simulations or NARR data.

In essence, observations and theory seem to agree favorably in explaining the propagation mechanisms of the July 12-15 surge event. The data available during this NAME surge event permit us to evaluate different mechanisms that describe the dynamical behavior of the leading edge of the moisture surge. Nevertheless, the application of the phase speed relationships, derived from the nonlinear semigeostrophic theory, to this event is subject to a variety of assumptions and simplifications that are complicated by synoptic variability and diurnal circulation processes. The following section will inspect how the surge affects the diurnal cycle of the low-level flow along the GoC. To a certain degree, a more complete understanding of the dynamics of the surge and its effect on the convective activity along the GoC require the application of more sophisticated models, especially the use of mesoscale numerical models, under more complicated and realistic situations. A state-of-the-science mesoscale numerical model will be implemented in Chapter 5 for this purpose.

3.4 Diurnal circulation and Convective Development for Surge of July 12-15

Figure 16 shows afternoon (00UTC) and morning (12UTC) surface streamline analyses before (July 12) and after (July 13-14) the surge passage. The surface streamlines were subjectively analyzed using surface station data, the lowest WP-3D flight level observations (300 ft above the ocean), and the lowest level of rawinsonde and pibal observations. These analyses suggest that the early morning land breeze (July 13-14/12UTC) is enhanced over the coast of Sonora after the surge passage. Meanwhile, the northern Gulf experiences stronger southeasterly winds at all times after the surge passage. These observations agree well with Anderson et al. (2001), who stated that the superposition of the large-scale pressure gradient, that presumably forces the surge, enhances the early morning land breeze along the Gulf eastern coast. However, outflow

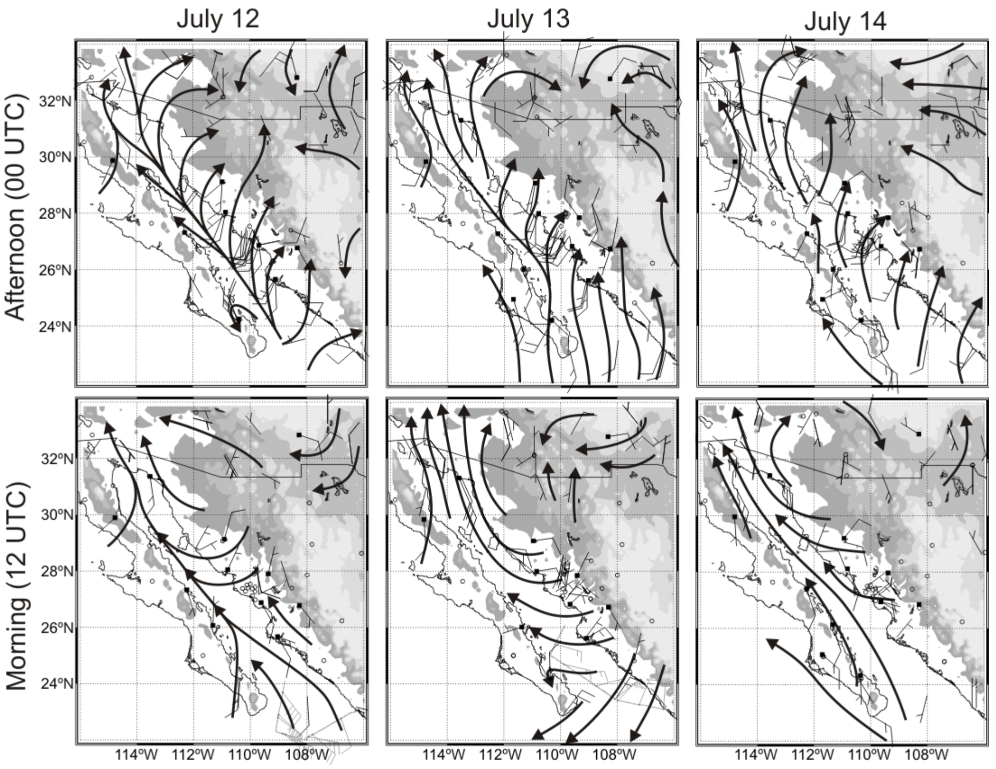

Figure 16. Afternoon (00UTC-upper panels) and morning (12UTC-lower panels) streamline analyses of surface station wind data during the July 12-15 surge lifetime. WP-3D flight level (990 hPa, light grey wind barbs), rawinsonde, and pibal observations (~100m above ground level, squared solid symbol) also were utilized in the analyses.

produced by enhanced convective activity, as observed after the surge passage (Figure 7), also supports enhanced offshore flow. Figure 17 shows the surface streamline evolution over northwestern Mexico after the surge passage (wind and pressure surge disturbance arrived at the northern end of the Gulf on July 13/03UTC). The MCS convective outflows that spread out over Sonora (July 13/09-15UTC) are superimposed upon the land breeze circulation, dominating the tendency for southerly winds associated with the surge that occured south of the MCS location. The proximity of TS Blas (Figure 7), which moved from the south of the Baja peninsula in a north-northwestward direction, may also be important in explaining the breakdown of the southeasterly flow along the Gulf. The opposite effect is observed over the northern Gulf region where the surface southerly winds are enhanced after the surge passage. The role of enhanced convective activity, due to the surge passage, in modulating the core GoC circulations and the surge variability itself constitutes part of the motivation for this research.

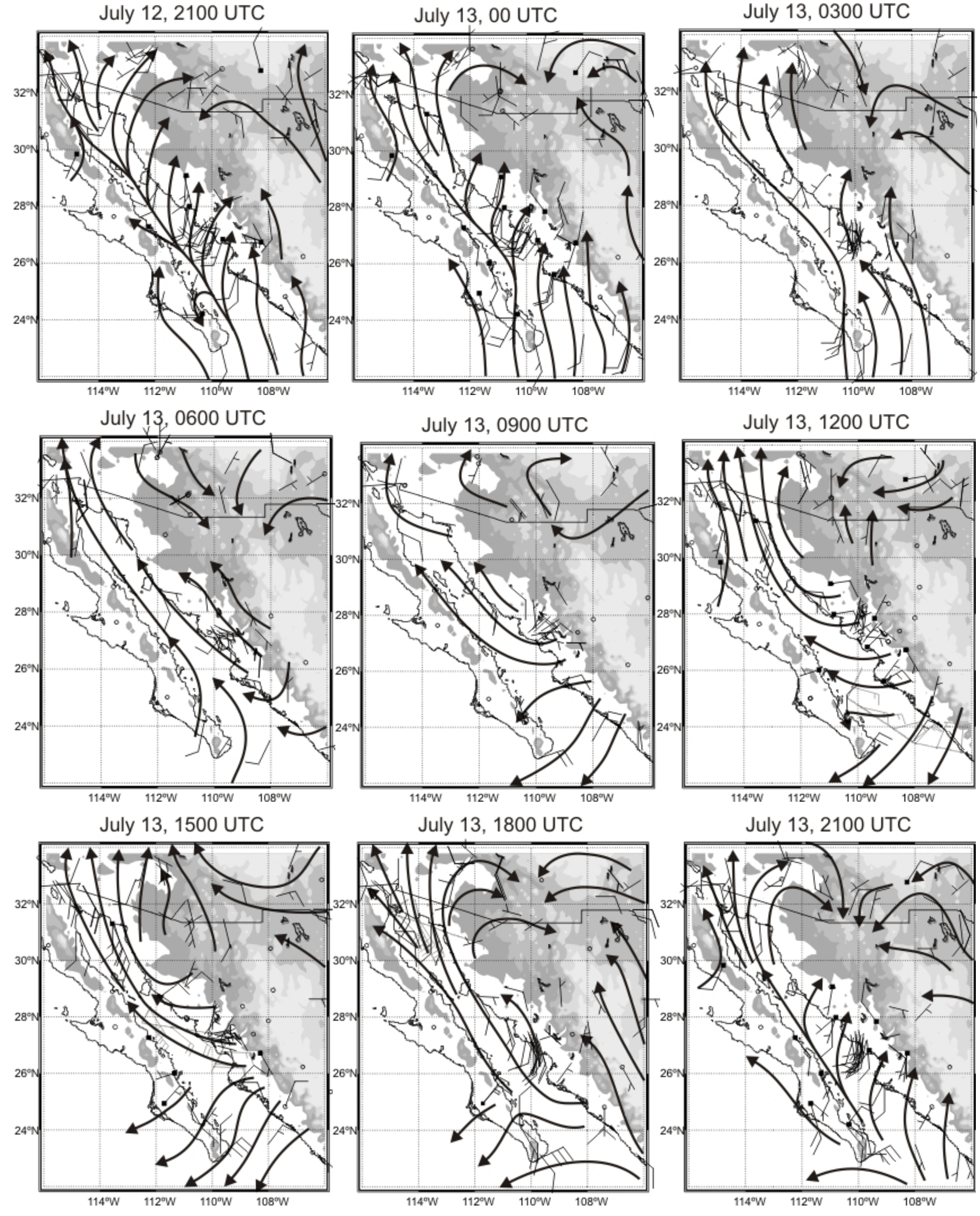

Figure 17. 3-hourly streamline analyses of surface station data from July 12 21UTC to July 13 18UTC. Analyses and observations was the same as for Figure 16. Notice the strong anticyclonic flow over the coastal plains of the central Gulf on July 13 from 0900 to 1500UTC associated with a dissipating MCS.

3.5 Vertical Structure and Diurnal Variability for Surge of July 12-15

Over the northern Gulf, a low-level jet-like structure developed during the early morning of July 13. WP-3D aircraft observations clearly show the jet structure during a transect over the far northern GoC (Figure 18). Strong winds below the 900hPa level, reaching 43 kts (22 m s^{-1}) in the 1-sec records, were observed just offshore of the eastern GoC coast. Although the LLJ in this region is a feature reflected in the climatological mean (Douglas at al., 1993), it presumably develops and is strengthened in response to surge events (Anderson et al., 2001). By compositing surge-type and non-surge-type conditions using data from numerical simulations, Anderson at al. (2001) concluded that during both conditions the LLJ is a geostrophic response to the cross-gulf pressure gradient induced by local thermal forcing, with stronger and better developed LLJ events occurring during surge-type conditions due to the superposition of the large-scale pressure gradient. However, the nature of anomalously strong LLJ events (Rogers and Johnson, 2007) still is not well-known. We hypothesize that this LLJ-like feature is partly a product of channeled gravity currents (Section 1.2, hypothesis 2) induced by thunderstorm convective outflows that are associated with strong nocturnal convective activity over the central and northern GoC coastal plain.

Comparison of the geostrophic wind and the observed wind during this LLJ event permits us to better distinguish the key forcings acting on the LLJ (Parish, 2000). Figure 19 shows profiles of meridional wind using observations from flight leg A-B shown in Figure 18b. The profile of meridional component of the geostrophic wind was calculated by using the WP-3D onboard radar altimeter and estimating the slope of the isobaric surfaces over the leg. Two important considerations in the calculation of the geostrophic wind are the steady–state assumption for observations across leg A-B (~ 1 hour spanning ~400km) and that the isobaric gradients are linear. The steady-state assumption may be important when isallobaric tendencies vary on timescales of the order of hours, which could be important for diurnal variations in the thermal contrast and even

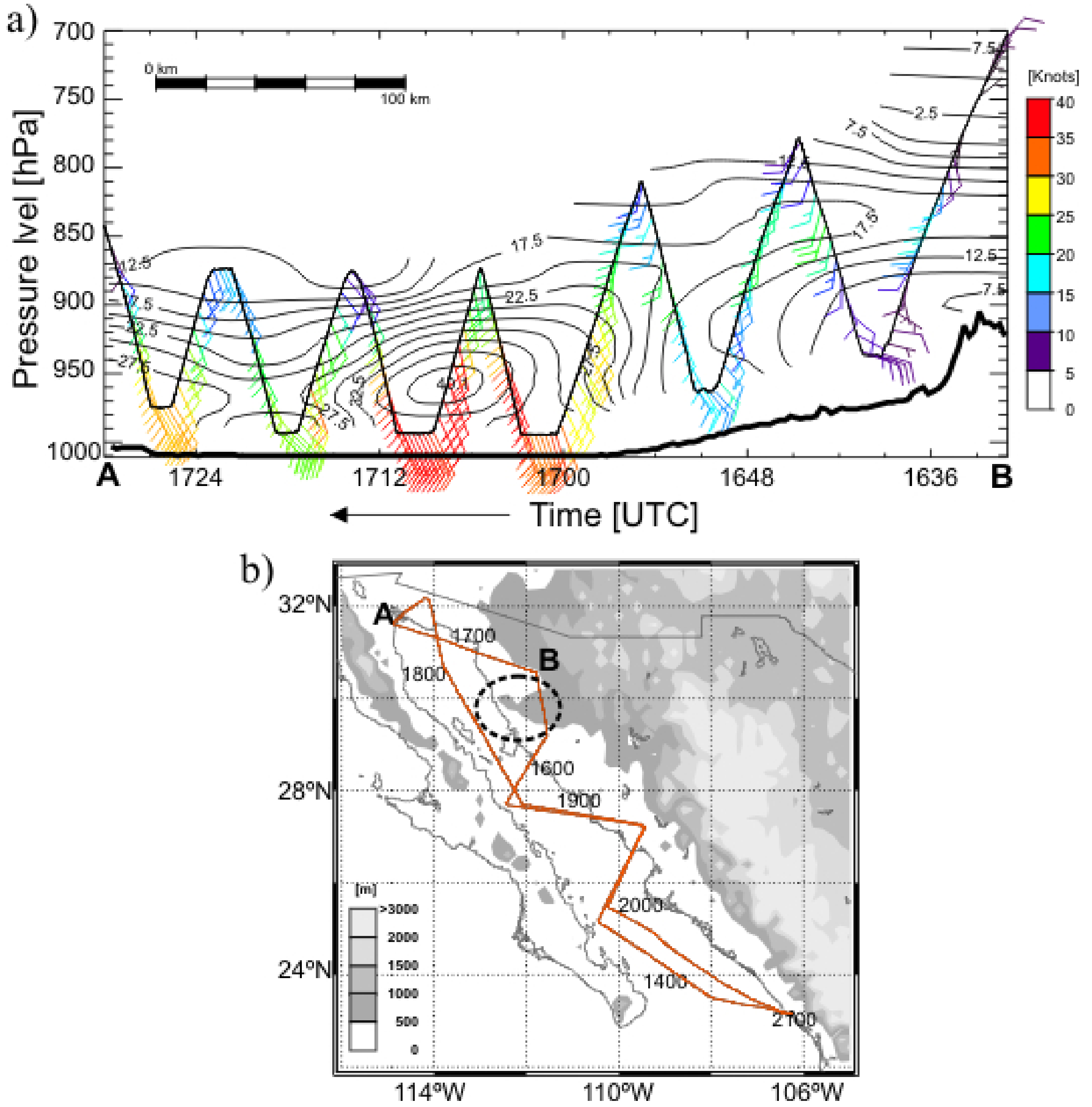

Figure 18. (a) Wind barb and isotach analysis (solid contours) for NOAA WP-3D flight across the northern GOC (horizontal transect A-B is shown in (b)) around 1700 UTC during NAME IOP-2 on July 13, 2004. Full barb is 10 knots and half barb is 5 knots with color scale indicated on right; isotachs are shown every 2.5 knots. The results are obtained by averaging 1-s data over 20-s intervals along the vertical saw-tooth flight path. Terrain is displayed with a thick solid line at the bottom of cross-section , where the GoC is drawn at 1010hPa. Notice the strong winds below the 900hPa level and located over the eastern margin of the GoC. (b) complete NOAA WP-3D horizontal flight track during NAME IOP-2 on July 13, 2004. Shaded contours indicate the elevation ASL in meters. Dashed circle highlights the location of relatively high terrain (> 500 m ASL) near the coast referred in Section 3.5.

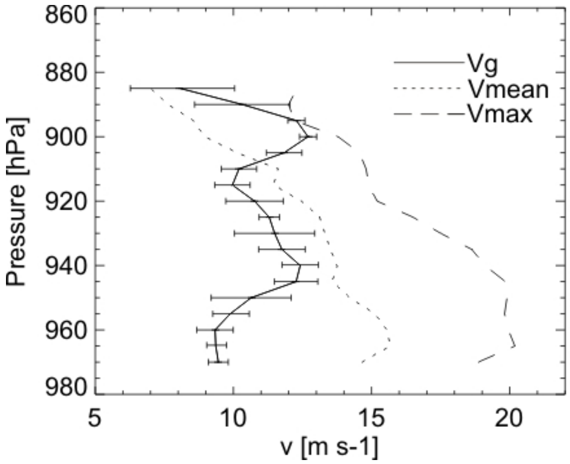

Figure 19. Vertical profile of meridional component of the geostrophic wind (solid line) estimated from aircraft observations across leg A-B shown in Figure 18b. Geostrophic wind is obtained by calculating the slope of the isobaric surfaces in the leg assuming that the isobaric gradients are linear. Error bars are obtained as +/-2 times the mean squared error in the least squares linear fit. Profiles for mean (dotted line) and maximum (dashed line) meridional wind component are also provided for the same leg.

more important for convective outflows. The impact of the second assumption was evaluated using the mean squared error of the least squares linear fit in order to calculate a range of uncertainty in the estimation of the geostrophic wind, which turned out to be relatively small (< 20%) compared to the magnitude of the geostrophic wind. Figure 19 shows that above 950 hPa the meridional geostrophic wind component is in reasonable agreement with the mean observed meridional wind. Below this level to the surface, the observed meridional wind (~14-15 m s^{-1} for the mean wind and ~20 m s^{-1} for maximum observed wind) substantially exceeds the geostrophic wind (~ 10 m s^{-1}), which disagrees with Anderson et al.'s (2001) simulations since low-level winds are not in geostrophic balance with the cross-gulf pressure gradient. In addition, the supergeostrophic wind speed may not be partially explained through synoptic forcing, for example superposition of synoptic-scale pressure gradient, since the observed wind profile would have a deeper structure. However, scaling analysis explains that isallobaric winds produced by synoptically driven pressure tendencies (e.g. TEWs, midlatitude troughs) may be of the order of ~2 m s^{-1} (Zehnder, 2004), which is still small compared to the observed winds. The presence of an MCS adjacent to the region where the LLJ was observed suggests that convective outflows may be partially responsible for the observed ageostrophic wind. We also expect some other mechanisms may be responsible of the ageostrophic components, such as the inertial advective components (frictional decoupling) and local flow enhancement due to high terrain near the coast (> 500 m ASL).

Although the evidence presented here is not conclusive about the role of the convective outflows in LLJ development and strengthening, the explanation of Anderson et al. (2001) does not readily fit this particular LLJ case. The relative importance of the role of convective activity for the surge will be further addressed in the next chapter by compositing LLJ days and surge events as a function of convective activity taking place over the Gulf region.

Figure 20-22 show the evolution of the along-gulf wind, potential temperature, and specific humidity anomalies, respectively, for different upper-air stations along the GoC coastal plain (Puerto Peñasco (ISS2), Bahia Kino (ISS3), Guaymas (MGYM), Los Mochis (ISS4)). These stations are aligned along the GoC from the northern end to the southern end; see station locations in Figure 5. The anomalies are calculated in the same way as those calculated in Section 3.2 for the surface quantities, in this case using 4-6-hourly rawinsonde IOP2 observations. Inspection of Figures 20-22 reveals a stronger and sharper surge-related signal at Puerto Peñasco. In general, all coastal stations show a single distinctive surge-related structure in the wind and temperature anomaly fields (Figures 20-21) that lasted about 3 days, extending from early July 12 to early July 15 at Los Mochis, and from early July 13 to late July 15 at Puerto Peñasco. However, the specific humidity anomalies show a noisier pattern, except at Puerto Peñasco, where positive specific humidity anomalies (Figure 22) resemble those for wind and potential temperature. The largest changes in the specify humidity field are confined to the lowest 50 hPa. Southeasterly wind anomalies seem to be stronger below the SMO average height, suggesting that the surge progresses northward as a coastal trapped disturbance (Mass and Albright, 1987). Wind maxima height decreases northward along the GoC coast, changing from around 700 hPa in the southern Gulf to 950 hPa in the far northern GoC, with southeasterly wind maxima (18 m s^{-1}, not shown) and southeasterly wind anomalies (9 m s^{-1}) at Puerto Peñasco. Climatological studies have shown that during surge events, the strongest wind anomaly during the surge day, as observed at Guaymas, has been detected around 950hPa (Douglas and Leal, 2003). In particular, the low-level wind speed maximum observed in Puerto Peñasco is associated with the LLJ-like feature observed over the far northern GoC with the WP-3D aircraft on July 13 at 17UTC (Figure **18**). Meanwhile, moderate to weak southeasterly wind anomalies also are observed at higher levels (Figure 20), which seem to be associated with a mid-tropospheric trough that is a northeastward extension of the TS Blas.

Figure 23 shows the evolution of the low-level circulation along the GoC eastern coast associated with the surge and its diurnal variability. In this figure, the average rawinsonde wind components between the 1000-900 hPa layer are shown; the morning (1000-1400UTC) and afternoon (2200-0200UTC) sounding results for along the GoC eastern coast were interpolated separately. Their difference then shows the changes in the diurnal wind variations associated with the surge passage. As mentioned earlier, the along-GoC wind component shows the northward progression of the surge, with a strong intensification of the southeasterly winds over the northern GoC region (between Kino Bay and Puerto Peñasco). Although the enhancement of the southeasterly flow is evident in both morning and afternoon composites, the morning winds are stronger. Evidence of changes in the diurnal circulation patterns also are shown in Figure 23. Morning offshore flow is observed in the southern GoC before the surge onset, while in the northern GoC onshore flow only weakens without becoming offshore. After the surge onset, the morning offshore flow is enhanced, to the point of producing offshore flow in the northern GoC. These observations agree with Anderson et al.'s (2001) evaluation of the effect of synoptically-forced surge events on the diurnal circulation patterns. However, they concluded that the local thermal forcing present during both surge and non-surge conditions are affected by superposition of the large-scale pressure gradient that acts offshore during surge conditions. This is a plausible explanation if we ignore the direct effect of enhanced rainfall taking place in the region. As mentioned earlier, convective outflows from MCSs occurring typically during the night over the SMO foothills and GoC coastal plains, and the associated low-level cooling inland, may also anomalously enhance the local thermal forcing favoring strengthen of both offshore flow in the early morning and the LLJ.

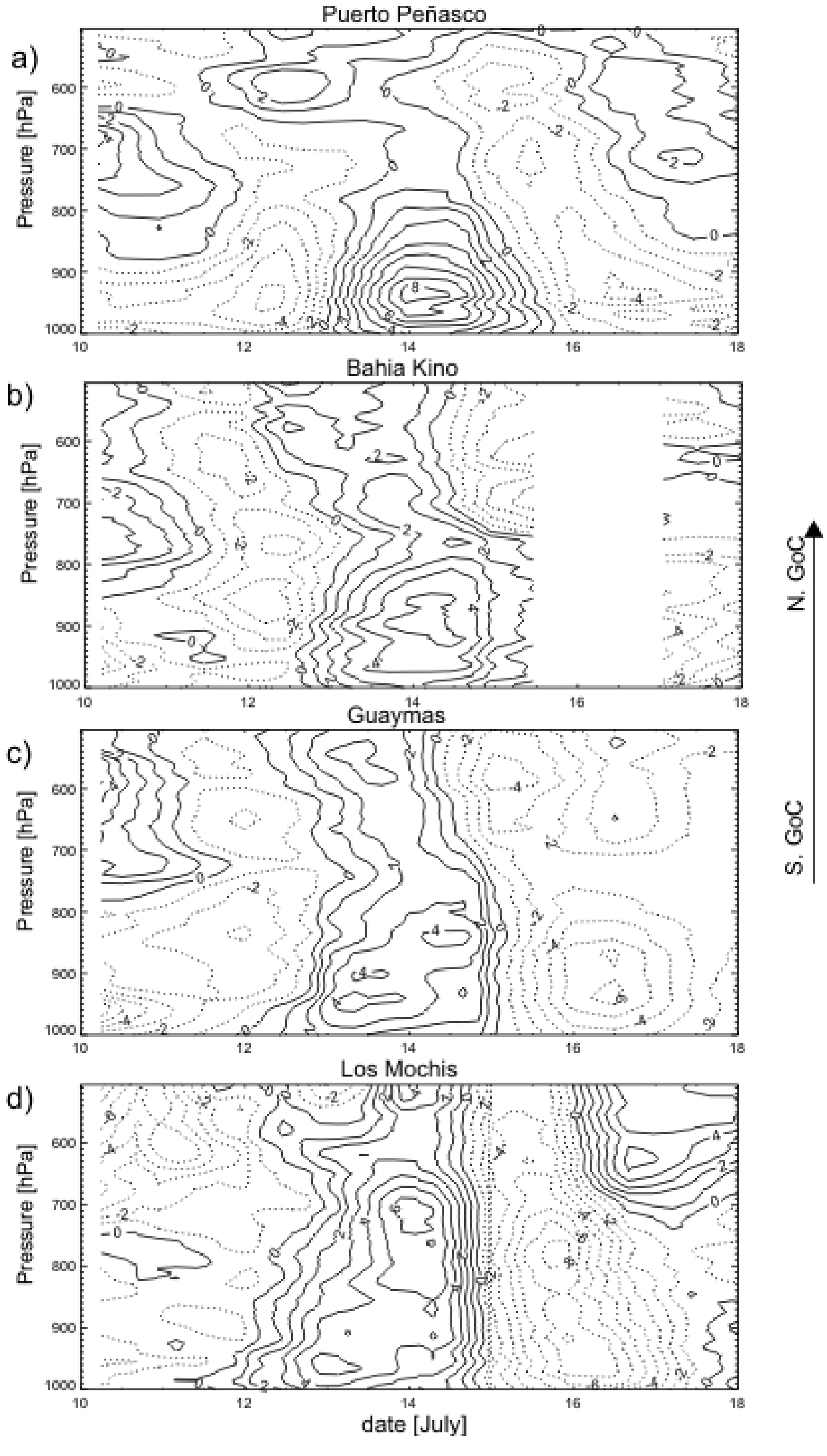

Figure 20. Along-GoC time-height wind anomalies (m s^{-1}) for a) Puerto Peñasco (ISS2), b) Bahia Kino (ISS3), c) Guaymas (MGYM), and d) Los Mochis (ISS4). See station locations in Figure 5. Diurnal variability was filtered out by retaining the 24hr running mean using 6-hourly data. Anomalies were calculated by subtracting the mean wind for July 10 to 20, at each level.

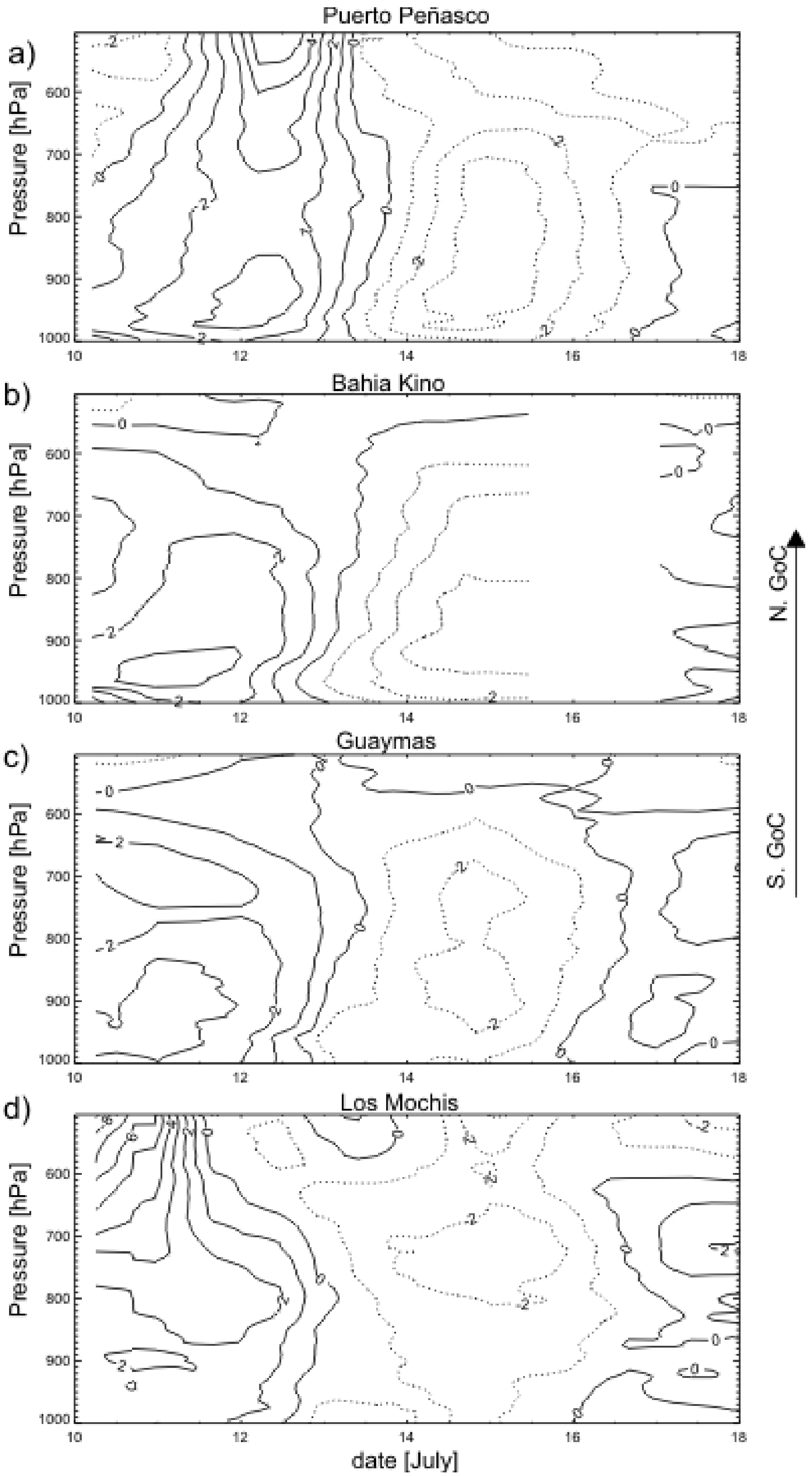

Figure 21. The same as Figure 20 but for θ anomalies (K).

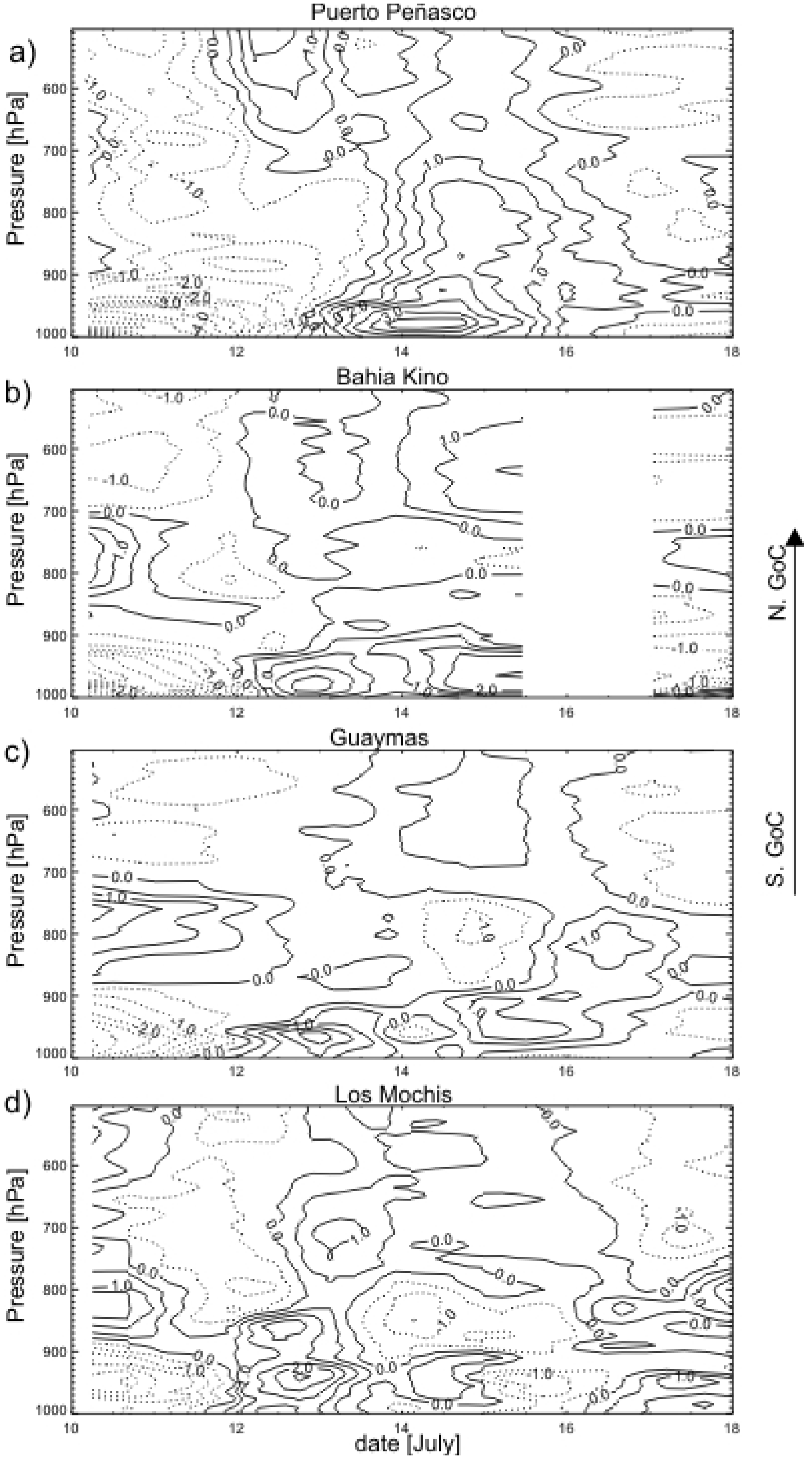

Figure 22. The same as Figure 20 but for specific humidity anomalies (g Kg^{-1}).

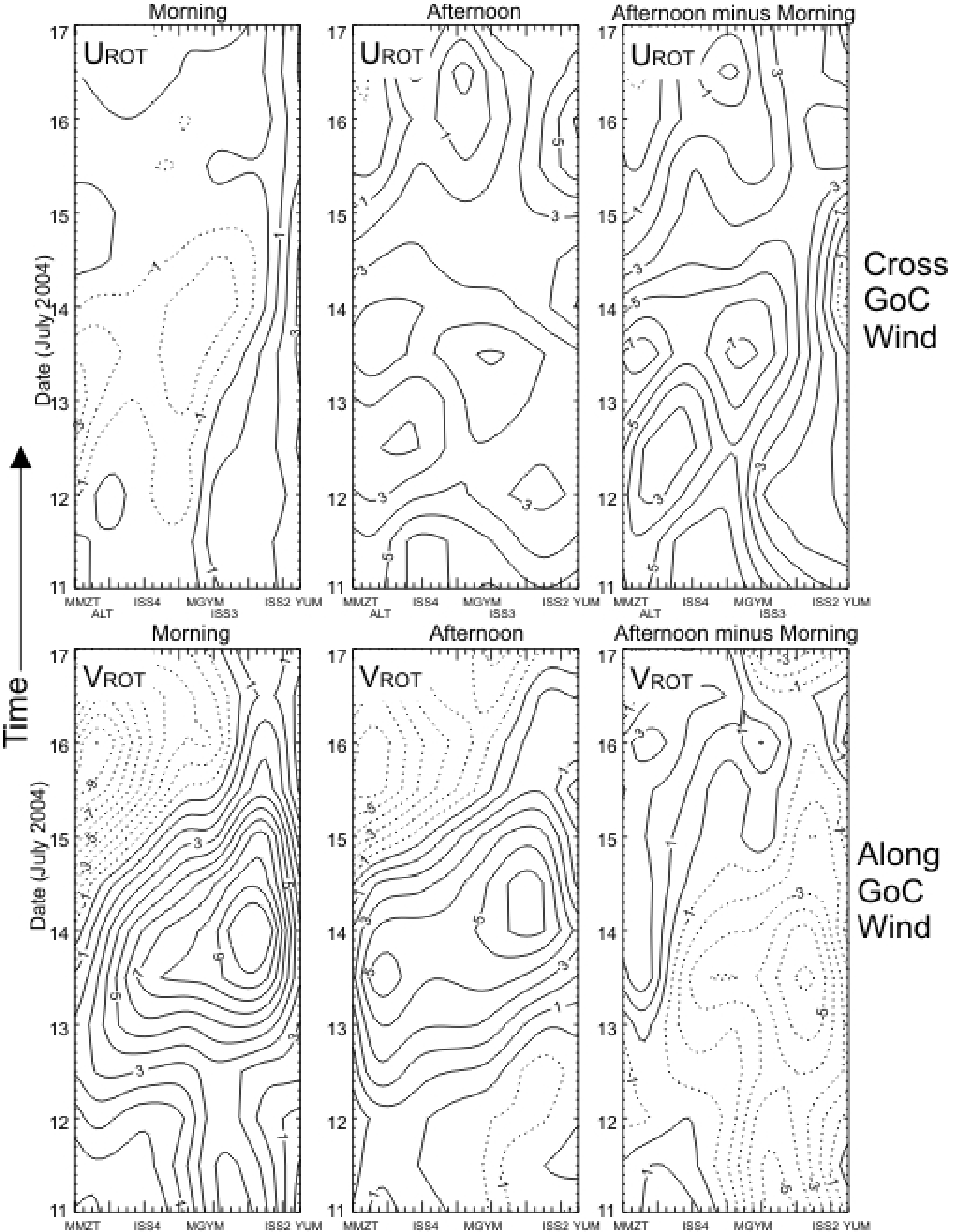

Figure 23. Eastern GoC coast time-latitude cross-section of cross-GoC (top panels) and along-GoC (bottom panels) wind components (m s^{-1}) averaged between 1000 and 900 hPa during NAME-IOP2. Soundings are separately interpolated for morning (left), afternoon (middle), and afternoon minus morning (right). The horizontal axis in each plot shows the relative location of the rawinsonde stations available during NAME-IOP2 (see station locations in Figure 5), southern Gulf region to the left and northern Gulf region to the right. Contours are plotted every 1 m s^{-1} with solid (dashed) isotachs indicating positive (negative) values. Notice the surge northward progression mostly evident in the along-GoC wind, and the relatively strong southerly flow in the northern GoC. Some systematic changes in the diurnal cycle low-level flow are evident during the surge passage, see text for more details.

3.6 Summary and Concluding Remarks

The moisture surge of July 12-15, 2004, represents a good example of a surge event associated with a tropical disturbance. TS Blas enhanced the low-level moisture flux along the GoC, which ultimately impacted northwestern Mexico and the southwesthern United States by increasing rainfall amounts. NAME observations were studied to elucidate the role of MCSs during the surge's lifetime.

The spatially dense and high frequency surface data obtained during NAME proved to be of great value in helping identify the moisture surge evolution, provided the relatively strong diurnal variability associated with local circulations in the coastal areas is removed from the time series. The surface network it made possible to show the surge variability associated with localized convective activity. This allowed for tracking surges associated with density currents that are mainly associated with MCSs over the coastal plains and the central GoC. The surge passage has different effects along the GoC coastal plain, with a large impact in the northern GoC.

The aircraft observations allowed for a unique description of the vertical structure and kinematics of the surge leading edge during its initial phase in the lower GoC, which better compares with a solitary Kelvin wave; however, the origin of the disturbance is still unclear. Further investigation is needed to determine the importance of the MCS's outflows in the surge initiation when synoptic disturbances are present. Although the NAME observational evidence presented here does not permit us to drawn generalized conclusions about the surge initiation mechanisms and the role that enhanced convective activity plays within the GoC region during the surge passage, it provides motivation for the following chapter regarding the climatological aspects of the role of convective activity in the moisture surge lifetime.

4 RELATIONSHIPS BETWEEN MOISTURE SURGES AND MESOSCALE CONVECTION OBTAINED FROM MULTI-YEAR SETS OF SATELLITE IMAGERY AND NORTH AMERICAN REGIONAL REANALYSIS DATA

The July 12-15, 2004, moisture surge presented in the previous chapter suggested the possible role of organized convective systems in modulating the surge initiation, intensity, and diurnal variability under forced synoptic conditions (TS Blas). This chapter therefore investigates further the influence of organized convective activity in modulating the surge evolution using a multiyear set of surge events. Understanding the role that synoptic-scale forcing and MCSs play in modifying moisture surges is crucial to improve short-term and intraseasonal forecasting in the region. No previous studies have systematically diagnosed the effect of convective activity in the eastern Pacific and GoC area on GoC moisture surges.

To address the first hypothesis (Section 1.2), a surge classification technique is developed to discriminate surge events based on their triggering mechanisms and their convective activity signature along the GoC. The surge forcings are identified from independent data sets. TEW events emanating from the Gulf of Mexico and Caribbean Sea are identified using NARR 700 hPa meridional wind component variations over the eastern Pacific; significant eastern Pacific TSs/TCs (named storms) associated with surge events are tracked using National Hurricane Center data; and the occurrence of organized convection in the form of MCSs are identified by using cloud top temperature thresholds from International Satellite Cloud Climatology Project (ISCCP) products (Section 4.1). Surges are stratified according to their synoptic forcing type, by MJO phase, TEWs or TSs/TCs, and also by their relationship with organized convective activity over the onset region (Section 4.2). Mean surge environments are composited by surge type using NARR products. Difference fields of convective characteristics are computed to compare the strength and evolution of surges with and without pre-surge MCSs (hereafter called MCS and non-MCS onset-related) in the southern GoC domain (Section 4.6).

The dynamical and thermodynamical features leading to enhanced convective activity are examined throughout in order to address the third hypothesis (Section 1.2) for different forcing mechanisms (Section 4.7). The second hypothesis (Section 1.2) is tested by stratifying surges according to the occurrence of MCSs in the northern half of the GoC. Mean and difference composite fields also are created for days without surge and MCS occurrence; this will identify the overall effect of MCSs relative to undisturbed synoptic environments. Overall, the focus is on timing of the MCSs relative to the diurnal low-level circulation, surge lifetime and location of the synoptic forcing.

4.1 Identification of Mesoscale Convective Systems

The identification of MCS events is based on GOES 7, 9, and 10 ISCCP infrared (IR) satellite data (Knapp, 2008: ISCCP B1U http://www.ncdc.noaa.gov/oa/rsad/gibbs/gibbs.html). The temporal resolution of the radiance data is 3-hourly (available since 1983), and the spatial resolution is ~10 km at nadir. The MCS identification procedure, a modified version of the Maddox (1980) approach, requires first finding detectable deep convection based on a minimum cloud-top temperature threshold. An IR cloud-top temperature threshold of −52°C is used in order to detect high, potentially precipitating clouds. This procedure cannot guarantee non-precipitating cirrus cloud. An MCS is identified when the area of this cold region exceeds ~50,000 km^2. The center of the cold cloud mass is identified as the location of the MCS. Tracking of the MCS was performed following Machado's et al. (1998) technique, which consists in a simple automatic method that follows cloud clusters using consecutive imagery. Figure 24 shows all of the MCS event centers identified during the June 15-September 15 periods from 1990 to 2006. Although the available observations eventually will permit the research to cover the period from 1983 to the present, only preliminary results for 1990-2006 are shown here. The present report does not include years 1983-1989, 1993, and 1994 due to suspicious satellite navigation errors that are currently under quality control testing (personal communication with Dr. Knapp).

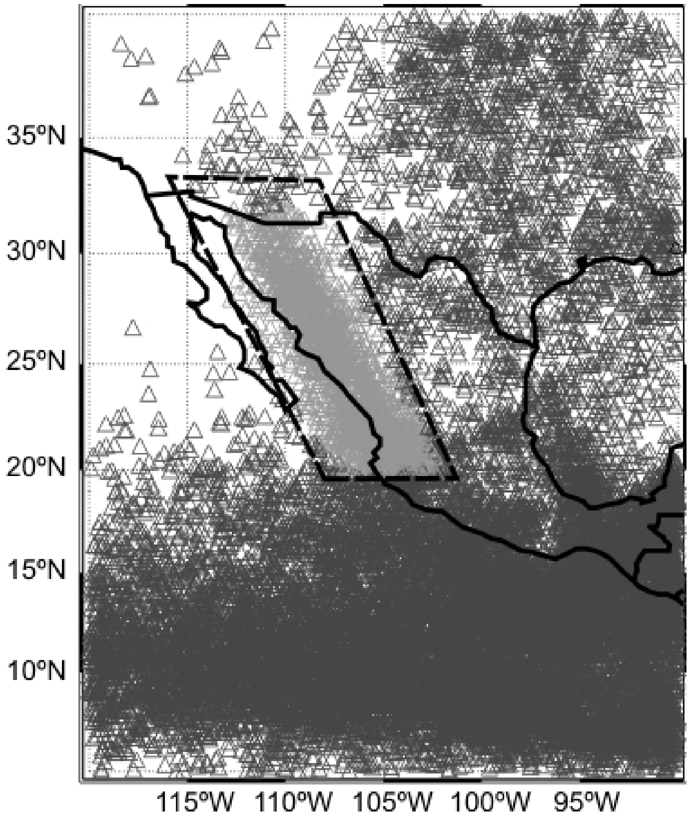

Figure 24. Spatial distribution of MCS locations when their cloud-top temperature first reached -52°C threshold during the summer (June 15-Sept 15) for 1990-2006. Dashed box encloses the MCS events used in the analysis in this chapter.

Since the actual occurrence of MCSs based only on cold cloud-top criteria may contain large uncertainties (overestimation of rainfall events due to cold cirrus), a systematic verification procedure was performed based on the NERN raingauges observations (Gochis et al., 2004) and other rainfall products based on TRMM multiplatform satellite data set (TRMM 3B-42 precipitation products). The overlapping period is only for the summers of 2002-2004. The TRMM 3B42 data set is expected to provide better rainfall observation than ISCCP GOES-IR because not only does it incorporate GOES-IR imagery, but also microwave sensors and a raingauge-based calibration procedure. We used the TRMM 3B42 to validate the occurrence of maritime MCSs over the eastern Pacific and GoC surrounding areas.

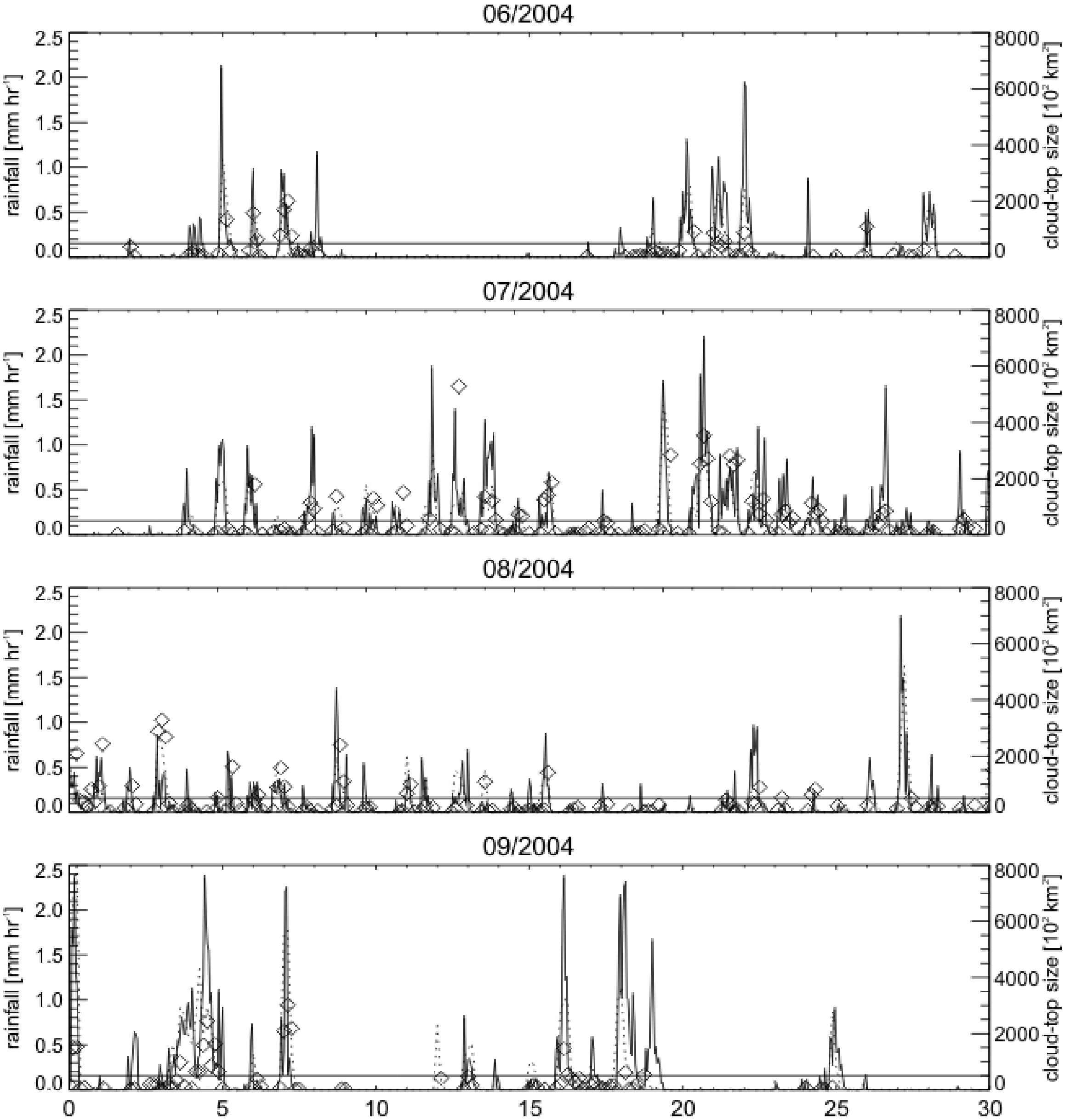

Figure 25. Areal average rainfall (mm hr^{-1}) using NERN (solid), TRMM (dotted) and cold cloud-top size based on GOES IR reflectivity (diamonds). Horizontal line at 50000 km^2 indicates the threshold above which a cloud cluster is classified as MCS.

Over the GoC coastal region, areal averages of NERN and TRMM compare reasonably well with GOES-IR cluster events (Figure 25). A simple contingency analysis between NERN and GOES, and between TRMM and GOES indicates that the success percentages are 66% and 73%, respectively. However, when comparing only between times associated with MCS events, their contingency analyses improve to 93%

and 97%, respectively. The analysis over the GoC entrance indicates that TRMM and MCSs agree 96% of the time. These results indicate that the procedure to capture MCS events, based on the GOES-IR cloud cluster retrieval mentioned earlier, is very robust and reliably captures larger rainfall events.

Figure 24 shows that in the GoC region most MCSs are preferentially located inland, along the western SMO foothills and over the GoC coastal plain. The lower GoC and the eastern Pacific region also show a high density of MCSs. As will be shown later (Section 4.4), easterly propagating disturbances such as TEWs are closely associated with MCSs developing in this region. Some studies suggest that the less frequent MCSs that are unrelated to TEWs may propagate with the easterly flow, and provide the disturbances that sometimes trigger tropical cyclogenesis over warm oceans (Elsberry at al., 1987; Zhang and Bao, 1996; Bister and Emanuel, 1997).

4.2 Identification of Major Moisture Surges

Moisture surges are identified using Yuma surface observations. As mentioned in Chapter 3, this station, located in the southwestern corner of Arizona, provides the most reliable observations for the identification of surges at high-temporal resolution (hourly). However, the surge identification technique involved has several problems, which stem especially from describing a propagating phenomenon from a single surface station. For the identification procedure, the meridional wind, temperature, dew point temperature, and sea-level pressure first are filtered using a 24-hr running mean, which removes the diurnal variability from the records and retains variability mainly associated with synoptic disturbances. Fluctuations of short period (less than a day) are damped by this procedure. A surge onset is defined as the time when the along-GoC diurnally filtered wind component exceeds the 20-day running mean of the above filtered time series. Capturing surges that are synoptically driven was further achieved by constraining the search to those surges with lifetimes of 2-5 days given by the above procedure. This approach reduced the possibility of detecting minor surges (which span about ~24 hours or less) induced by convective outflows or similar structures (Brenner, 1974; Fuller and

Stensrud, 2000) most likely created in the central GoC region. We claim that this approach increases the possibility of identifying surges that propagate and affect the entire GoC region. The dew point temperature must also exceed 15.7 ºC within 24 hours after the first southerly wind is observed (Fuller and Stensrud, 2000). Hereafter, the surges selected by this procedure are called "Control Surges." Other surge classification techniques also were considered but presented some complications. For example, Bordoni and Stevens (2006) created different surge identification procedures based on Empirical Orthogonal Functions analysis using 10-m ocean wind measurements by the Quick Scatterometer (QuikSCAT). In their results, they identify surge events as the leading mode of synoptic-scale variability in the region. However, this procedure is unable to provide a large sample of surge events due to the relatively short-length of the records (available since 1999), and due to its coarse spatial resolution, their procedure is also unable to detect surges that may have developed in the northern half of the GoC. Later in this chapter (section 4.7.2), we performed a detailed evaluation of the QSCAT as a diagnostic tool for identification of surges in the region.

Control Surges are further classified by their associated synoptic-scale feature, such as TS/TC and TEW. Some TSs/TCs may develop from an intensifying TEW crossing over Central America or Mexico, in which case the surge is referred to as "TS/TC-related surge", whereas "TEW-related surges" were carefully selected only where TS/TC events were absent in the region (at least not closer than 1000 km from the GoC entrance).

In addition to stratifying surges by the above synoptic forcing, surges also can be further disaggregated according to whether or not they are associated with MCSs. The same surge events were classified as to whether MCSs were present over the lower GoC region (20ºN-25ºN, see Figure 24). For the surge to be classified as MCS-related, the MCS must also have occurred from 48 to 18 hrs before the surge arrival at Yuma. A Yuma surge that did not have an MCS satisfying these criteria was classified as a non-MCS surge. This taxonomic organization of moisture surges includes overlapping cases since MCS occurrence in the NAM core region also is linked to TS/TC and TEW occurrences as will be shown in Section 4.4.

The co-occurrence of TSs/TCs with moisture surges is evaluated using U.S. National Hurricane Center data, which provide 6-hourly position information on TSs/TCs. A procedure similar to Higgins and Shi (2005) is adopted with slight modifications to classify TS/TC-related surges. In this research, only TS/TC events that directly affect the surges from the eastern Pacific are considered, and their centers of rotation must have drifted to the north or northwest within 500 km from the GoC entrance. Landfalling TSs/TCs were not considered in this analysis.

TEWs were automatically tracked by following clusters of relative vertical vorticity maxima using daily NARR wind data at 650 hPa. A verification procedure was performed using visual inspection of longitude-time Hovmoller diagrams at different latitudes (10ºN, 18ºN, and 25ºN) using the NARR 650hPa meridional wind. These procedures help to track TEWs coming from the Caribbean and others that develop over the eastern coast of Mexico. This technique does not capture all TEW disturbances. For example, multiple centers of vorticity maximum also were tracked westward from the Gulf of Mexico (GoM) but they did not show coherent spatial structure. Therefore, the automatic TEW selection technique filters these features out while preserving the strongest and most coherent vorticity structures.

Table 4 and Figure 26 summarize the number of cases obtained using the procedures explained above. For background comparison purposes, averages of surge environments are estimated by selecting all the surges observed at Yuma (called “Control Surges”) that meet the criteria without stratification by the type of synoptic disturbance that triggered them. A total of 112 Control Surges were selected from the 17-year record. Among the Control surges, 40 and 50 surges were identified to be TS/TC-related and TEW-related surges, respectively. The remaining 22 surges were not related to either of these synoptic disturbances. Two-thirds (73) of the Control surges were associated with active MCS convective environments over the lower GoC region. There are 78 TEW surge-related events, but some of them ended up being TS/TC, which moved them out of the TEW category. Of note is that 10 out of 42 TS/TC are not related with TEW events.

Table 4. Number of surge events for different tropical synoptic disturbance and convective activity categories during the summer (June 15-Sept 15) for 1990-2006. Control cases are all the surges that met the Yuma surge criteria without further classification. Tropical synoptic disturbance categories involved are TS/TC-related and TEW-related surges. Convective activity amount categories: surges with at least one (no) MCS developing before the surge onset over the lower GoC region are categorized as MCS-related (non MCS-related). See Figure 26 for organizational structure.

Category	Control	TS/TC	TEW	MCS	Non-MCS
# surges	112	40	50	73 (TS/TC 26; TEW 33, other 14)	39 (TS/TC 14, TEW 17; Other 8)
# surges /year	6.6	2.4	3.0	4.3	2.3
% of Control	100	36	45	65	35

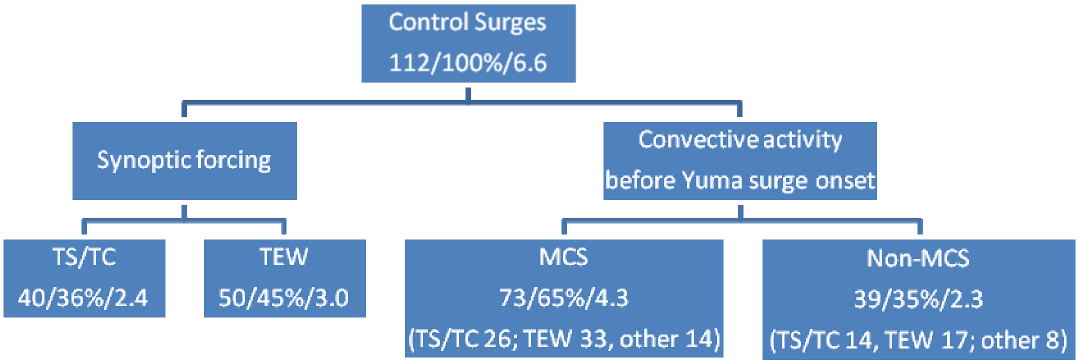

Figure 26. Organization chart of surge-related events during the summer (June 15-Sept 15) for 1990-2006 for different tropical synoptic disturbance and convective activity categories. Number of surges, percentage relative to control surges, and average number of surges per year are displayed in left/center/right format.

4.3 Relationships between the MJO and Major Surges

This section describes relationships between intraseasonal variations in the eastern Pacific associated with low frequency (30-60 day) synoptic-scale disturbances called the Madden-Julian Oscillation (MJO; Madden and Julian, 1971, 1994; Hendon and Salby, 1994) and higher frequency perturbations associated with TSs/TCs, TEWs, and GoC moisture surges. As noted in Section 1.1, several studies (Lorenz and Hartmann, 2006; Higgins and Shi, 2001) have suggested that some enhanced rainfall events (lagged by ~

10 days) in the NAMS core region tend to occur during the MJO active phase. Lorenz and Hartmann (2006) suggested that enhanced moisture surge activity may be one physical mechanism explaining enhanced rainfall over the NAMS core region. They argued that amplification of TEWs (Maloney and Hartmann, 2001) and an increase in TS/TC activity (Maloney and Hartmann, 2000; Higgins and Shi, 2001; Barrett and Leslie, 2008) during the MJO active phase may increase the likelihood for moisture surges. This section explores these relationships by stratifying the occurrence of moisture surges, TEWs, and TSs/TCs relative to the phase of the MJO events.

4.3.1 MJO local phase space

The evolution of the MJO is evaluated in local phase space rather than in time space. This procedure provides less smoothing when compositing events with a wide range of wavenumbers and periodicities (e.g., wavenumber 1-5 and periodicities of 30-60 days). The local phase (φ) is calculated for each of the MJO indices (I) using the same procedure as in Barlow and Salstein (2006). The analysis in the local phase space assumes that each MJO event can be mapped into a sine function in the domain [$-\pi$, π] with average frequency ($\overline{\varpi}$) of 46 days such as

$$\varphi = sin^{-1}\left\{\left(I\left(I + \left(\frac{\frac{dI}{dt}}{\overline{\varpi}}\right)^{2}\right)\right)^{-\frac{1}{2}}\right\}. \qquad (4.1)$$

The selection of $\overline{\varpi}=46$ days minimizes biases in the local phase. Chi square test with confidence level of 95% was performed to verify that φ fits a uniform distribution with negligible seasonal biases during the June-September period (not shown). However, only MJO events within one standard deviation from zero were chosen in the compositing analysis. Figure 27 shows the average normalized MJO indices in the phase space for all significant events during the 1990-2006 summer seasons (June-September period). A total of 44 significant events were identified in the 17-year period, or about two to three MJO significant events per year during the summer season. The index values associated with φ = –π/2 and φ =π/2 correspond to the minima (defined as the MJO active phase) and maxima (defined as the MJO inactive phase), respectively.

4.3.2 Spatial OLR patterns associated with the MJO

Figures 28-29 show composites of OLR fields during active and inactive MJO phases for both MJO CHI200- and OLR-based indices, respectively. Not surprisingly, the MJO OLR-based index shows a maximum (minimum) in convective activity associated with the MJO active (inactive) phase. The similarity between these two figures confirms the aforementioned connection between the MJO upper-level large-scale dynamical signal and convective activity. A remarkable dipole in OLR anomalies between the EPAC and the NAMS region accompanies the MJO extreme polarities. Suppressed (enhanced) convective activity over the NAMS core region is associated with enhanced (suppressed) convective activity in the EPAC region. This rather meridional dipole agrees with results shown in Barlow and Salstein (2006), who used daily rainfall data over southern Mexico and Central America to do compositing analysis about the MJO evolution. Barlow and Salstein concluded that the NAMS core region shows a weak negative rainfall anomaly during the MJO active phase.

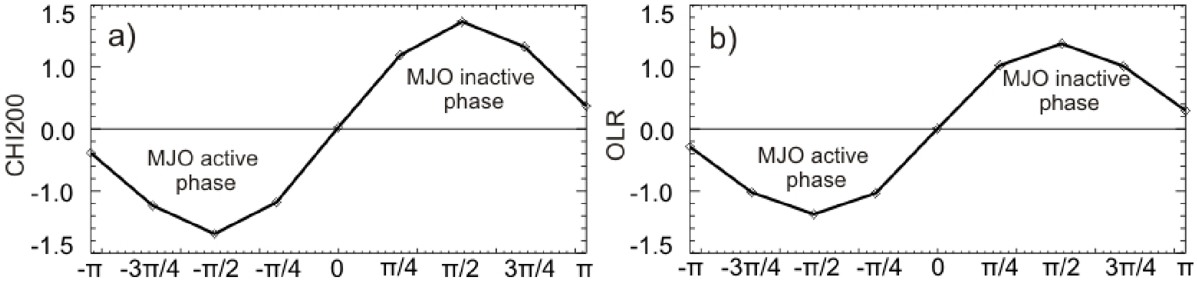

Figure 27. Average normalized a) MJO CHI200 and b) OLR indices in the phase space for a complete cycle [-π, π] of all significant events during the 1990-2006, June-September period. Abscissa resolution is π/4 (~ 5 days).

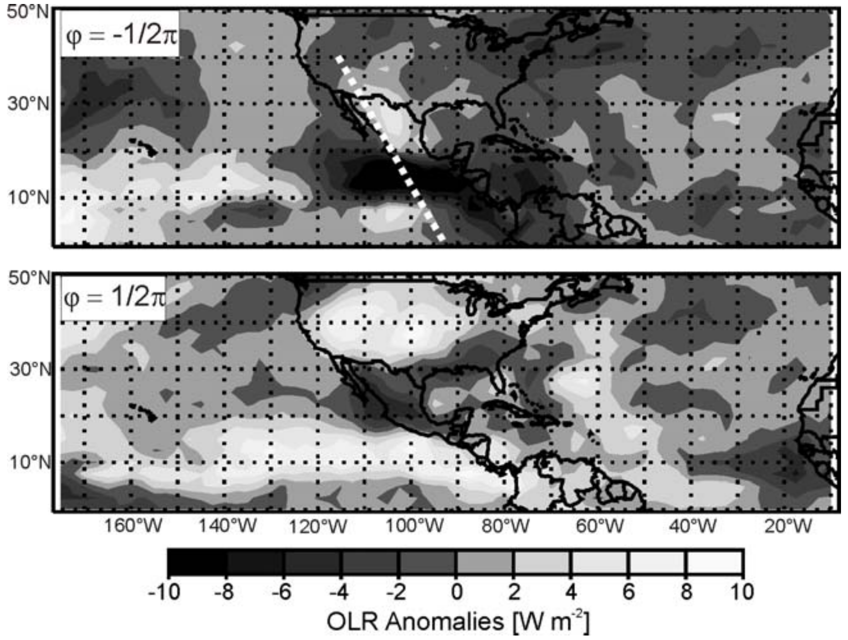

Figure 28. Composite OLR anomalies using MJO CHI200-based index for φ=–π/2 (top) and φ =π/2 (bottom). Negative (positive) OLR anomalies represent more (less) high, cold clouds which may be interpreted as regions of active (suppressed) convection. Dashed white line shows location of the SE-NW oriented Hovmoller shown in Figure 30a and Figure 31b.

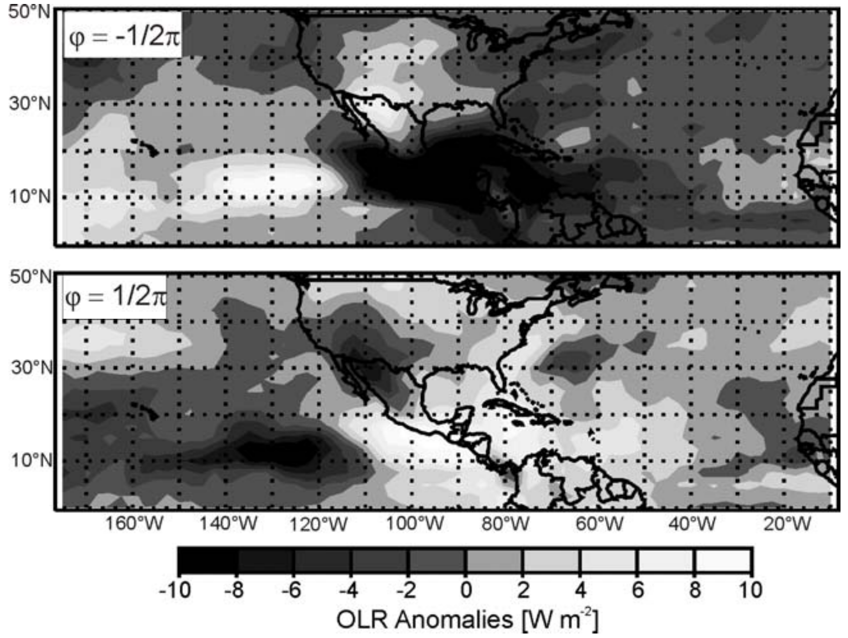

Figure 29. Same as Figure 28 but for the MJO OLR-based index.

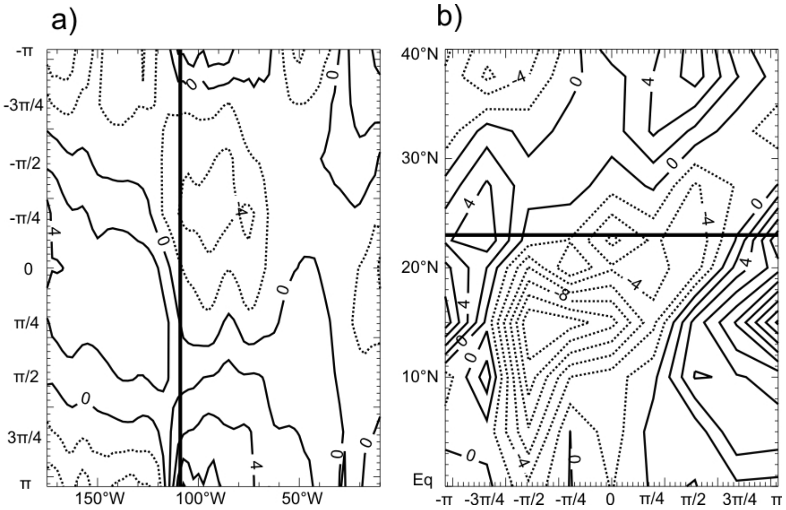

Figure 30. Phase space evolution composite for the MJO CHI200 based index of a) zonal (averaged over Eq-20°N) and b) meridional OLR anomalies for transect shown in Figure 28. For geographical reference, solid lines in both panels show the a) longitude and b) latitude of the of GoC entrance. Contours are plotted every 2 W m^{-2}. Solid (dotted) contours show positive (negative) OLR anomalies.

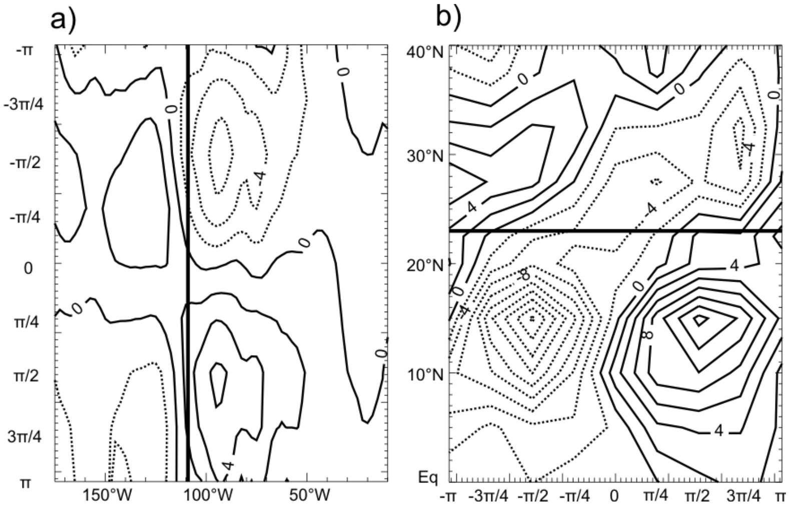

Figure 31. Same as Figure 30 but for the MJO OLR based index.

4.3.3 Evolution of OLR and MJO

Figures 30 and 31 show the phase evolution composite of OLR anomalies along a zonal tropical transect for the MJO CHI200 and OLR based index, respectively. An eastward moving negative OLR anomaly, associated with the MJO active phase, is evident in the MJO CHI200-based composite (Fig. 30a), while the MJO OLR-based composite shows a feature that resembles better a stationary mode (Fig. 31a). This latter mode may be influenced by the climatological signal associated with the mid-summer drought mentioned earlier. However, over the EPAC region (110-80°W), the transition from negative OLR to positive OLR is prominent. The phase of the maximum amplitude of OLR anomalies for the MJO CHI200-based index (Figure 30a) lead those of the MJO OLR-based index (Figure 31a) by $\pi/4$ (~ 5 days). This result is consistent if we assume that the Kevin wave associated with the MJO CHI200 upper-level signature propagates at 10m s^{-1} (Krishnamurti, et al., 1992). Thus, an eastward moving wave would take about 4 days to propagate from 120°W (location where the CHI200 index was extracted) to 90°W (mid-EPAC region). On the other hand, the most striking feature of the OLR composites shown in Figures 30 and 31b, is a northward progression of negative OLR anomalies associated with the MJO active phase, which arrive over NW Mexico and SW United States after $3/4\pi$ (~ 15 days). These results show finer structures regarding the phase of the MJO and its effect on convective activity over the NAMS region when compared with previous studies (e.g., Higgins and Shi, 2001; Lorenz and Hartmann, 2006; Barlow and Salstein, 2006). However, they differ slightly from the Lorenz and Hartmann (2006) regression analysis which showed that EPAC 850 hPa westerly winds anomalies precede maximum enhancement of rainfall in the NAMS regions by nearly 10 days. Although a difference of 5 days may be significant, we stress that the analysis may be sensitive to the selection of the MJO index.

In summary, the northward progression of negative OLR anomalies associated with the MJO active phase, has the strongest impact over the NAMS region, while concurrently the EPAC region experiences the MJO inactive phase. The next section shows the connection between this near out-of-phase (dipole) relationship in OLR anomalies between the EPAC and NAMS regions and other synoptic scale disturbances occurring in the region, such as TSs/TCs, TEWs, and surges.

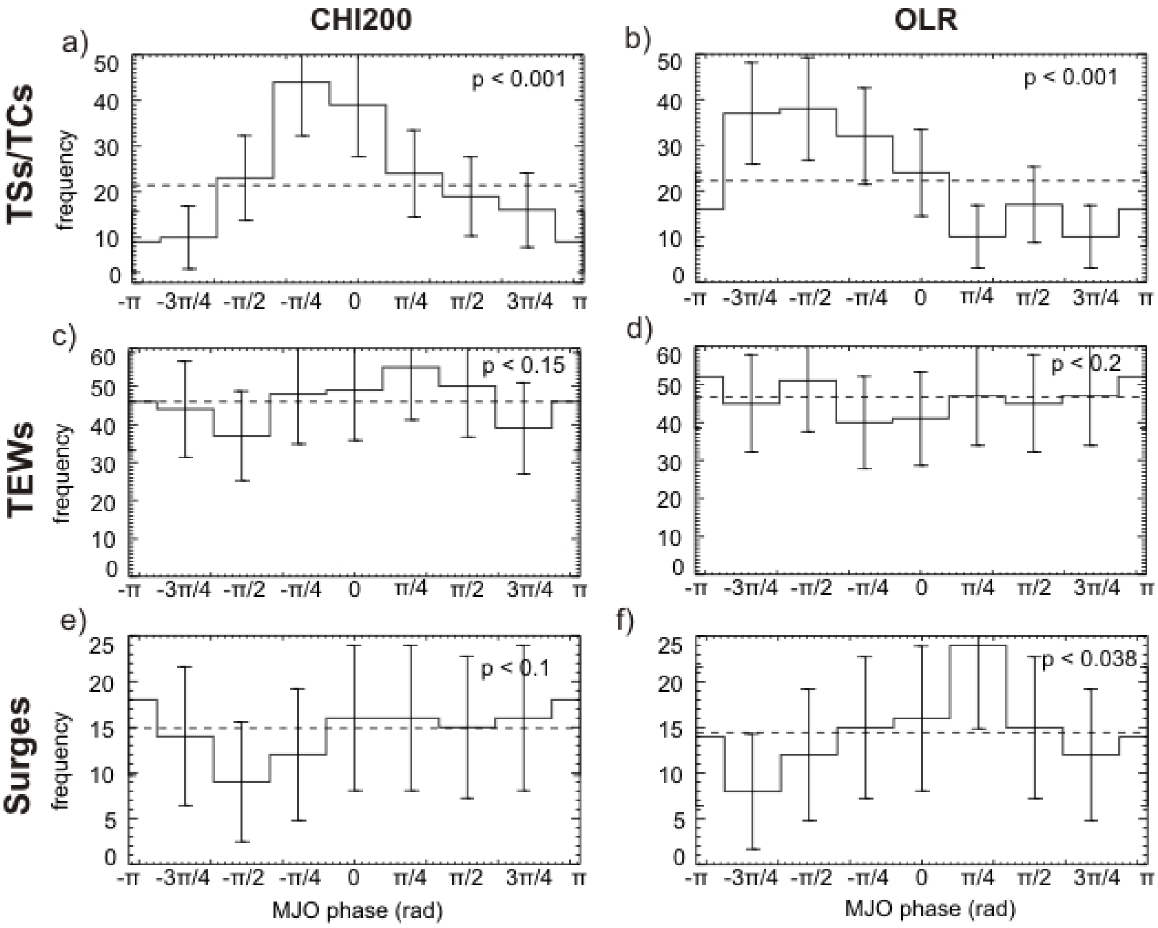

Figure 32. Frequency of TSs/TCs, TEWs, and surges as a function of local phase of the MJO CHI200- (left panels) and OLR-based indices (right panels). Bin size for each histogram is π/4. Error bars are calculated using the Student's t statistics for a 95% confidence level. The upper right corners in each panel show the probability of having the observed frequency distribution (solid line) approaching an uniform distribution (dashed line).

4.3.4 TSs/TCs, TEWs, and Surges versus MJO Phase

The relationships between the TSs/TCs, TEWs, moisture surges and the MJO CHI200- and OLR-based indices are shown in Figure 32. Student's t statistics were used to determine the 95% confidence level and a Chi-square test was performed to determine whether the observed frequencies differ significantly from a random uniform distribution ($p<0.05$). In general, Figure 32 shows that the MJO activity in the EPAC region is more closely associated with changes in frequency of eastern Pacific TSs/TCs activity (Figure 32a and b) than in frequency of TEWs (Figure 32c and d) and moisture surges (Figure 32e and f). The modulation of the frequency of TSs/TCs associated with either MJO index is statistically significant and agrees with previous findings (Maloney and

Hartmann, 2000; Higgins and Shi, 2001; Barrett and Leslie, 2008). Hence, more TSs/TCs are expected over the EPAC region during the MJO active phase. However, this relationship seems stronger and offset by π/4 for the MJO CHI200-based index than for the MJO OLR-based index. TSs/TCs nearly quadruple during the MJO CH200-based active phase (Figure 32a), while they only double to triple for the MJO OLR-based active phase (Figure 32b). Both indices show that the maximum frequency in TS/TC activity is in phase with their OLR negative anomalies composites (Figures 30, 31)

In contrast with TS/TC frequencies, the TEWs do not seem to be sensitive to any of the MJO indices (Figure 32c, d). Previous studies noted that the MJO active phase may affect TEW growth in the region that subsequently leads to an increase in tropical cyclogenesis (Molinary and Vollaro, 2000; Maloney and Hartmann, 2001). Interestingly, moisture surges are affected by the MJO phase (Figure 32e, f), although the statistical significance of surge distribution for the MJO CHI200-based index (Figure 32e) is rather small compared to the MJO OLR-based index (Figure 32f). Furthermore, some striking features are noted in terms of the amplitude of the distribution and the phase of the maximum amplitude. For example, there are surge frecuency increases of nearly 50% and 120% for the MJO CHI200- and OLR-based indices, respectively, whereas the timing of the maximum in surge frequency occurs around 0-π/4 and π/4 for MJO CHI200- and OLR-based indices, respectively. On average, the timing of the maximum frequency of surges leads by 10-15 days the maximum TS/TC activity, while the maximum frequency of surges appears to be in-phase with the negative OLR anomalies over the NAMS region (Figures 30-31). Thus, although the relationship between the MJO active phase and TS/TC activity is very clear, the increase in TS/TC activity (during the genesis stage) does not appear to directly impact the moisture surge distribution. However, it is possible that surges are better connected with TSs/TCs during advanced stages rather that during the early genesis stage. For example, this 10-15 day gap is reduced to 5-10 day (not shown) when we only consider TSs/TCs. This gap is even smaller if we account for the time it takes from surge genesis to propagation to the SW United States (e.g. Yuma).

4.3.5 MJO influence over the NAMS core region

It is expected that the predictability associated with the MJO (of the order of weeks) may potentially be extended to the NAMS through a better understanding of the moisture surge phenomenon and other components responsible for the synoptic-to-intraseasonal variability of the NAMS. Both indices used here to describe MJO variability have shown good performance for near-real time diagnostics and intraseasonal timescale forecasting (Wheeler and Weickmann, 2001; Xue et al., 2002). However, MJO and convective activity in the EPAC and NAMS are sensitive to the selection of the MJO index (geographical definition of MJO). The MJO OLR-based index shows a significant stationary component mode rather than a clear eastward propagation mode as one would expect from the MJO related wavenumbers (typically wavenumber 1). Relationships of the eastward-propagating MJO are not only observed with the MJO upper-atmospheric response (CHI200) but also with the enhanced convective activity signal that is presumably connected to it.

Lorenz and Hartmann (2006) suggested that rainfall over the NAMS region during MJO events may be enhanced by processes that lead to an increase in surge activity. In their study, they argued that the MJO active phase provided favorable conditions for TEW growth, enhanced TS/TC activity or even directly favored MCS developments over the NAMS region. In a statistical sense, we believe that the progression of events agrees, with some limitations, with those proposed by Lorenz and Hartmann (2006).

In summary, the MJO active phase is associated with negative OLR anomalies in the EPAC, while it exhibits coherent positive OLR anomalies in the NAMS region. Negative OLR anomalies move eastward and northward and overturn the OLR regional anomaly pattern in ~15 days. Results show that enhanced convection in the NAMS core region seems to be statistically connected with an increase in surge frequency (up to 120% increase). However, the connection between surge and TS/TC frequency is not clear since there is a 5-10 day gap in the progression of the events.

4.4 Relationship between TEW Occurrence and MCSs in the NAMS Core Region

Figure 33 shows a 15-year analysis of MCS events associated with TEW passage over the NAMS core region. The NAMS core region was divided in “northern” and “southern” subregions at 25ºN, to separate the western hills of the Sierra Madre Occidental (SMO) mountains and GoC coastal plains into two domains. The concurrence of MCSs with TEWs is quantified using the information on trough passages over western Mexico obtained from the NARR daily meridional wind signal at 650 hPa along 105ºW. Figure 33a shows a time-lagged analysis of the mean meridional wind anomaly associated with the 650 hPa trough axis passage over 105ºW for different latitudinal bands (centered at 15, 20, 25, 30ºN, with 5º width). This analysis extends from –3 days to +3 days, lag zero indicating the trough axis passage over the 105ºW meridian. Not surprisingly, the meridional wind composites show that anomalies change from northerly to southerly with the trough passage with a relatively large meridional extension. Figure 33a also shows a time-lagged analysis of MCS occurrence about the TEW trough passage. The striking feature here is that a significant changes in the number of MCS are observed during the TEW passage. The number of MCSs in the southern domain doubles, from an average of 9 MCSs on day -3 to 18 MCSs on day +1, whereas the northern domain only shows an increase of ~60% in the number of MCSs from 8 MCSs on day -1 to 13 MCSs on day +1. The maximum number of MCS events occurs one day after the trough axis passage (day +1), with relatively more MCS events taking place over the southern domain.

Figures 33b, c show the mean seasonal cycle and interannual variability of the TEW activity and how these are related to MCS activity. The very marked seasonal cycle of MCS activity contrasts with the lesser, though still evident, seasonal change in TEW activity. While the mean MCS activity doubles in the southern domain and quadruples in the northern domain from June to July, the mean number of TEWs only changes from 3 to 4-4.5 during the same period. This suggests that there are other large-scale features that modulate MCS activity besides TEWs, such as the mean environment – which markedly changes during the late June monsoon onset.

Our results also show considerable interannual variability in both the TEW and MCS activity (Figure 33c). For both NAMS core subregions, Figure 33c shows some level of correspondence between TEW and MCS activity for much of the time series. However, the average linear correlation between these time series for 15 summers is only +0.29 and +0.43 for the southern and northern subregions, respectively. Therefore, the analysis presented here, based on the ISCCP satellite imagery and the TEW classification technique using NARR wind data, suggests that large-scale forcings associated with TEWs play an important role in the organized convective activity in the region. This was reflected in the surge classification technique implemented in Section 4.2, which included surge events that were associated with both synoptic environment (TS/TC- and TEW-related surges) and with convective activity in the southern GoC (MCS and non-MCS onset-related surges).

4.5 Role of MCS during Minor Surges

The analysis of surface observations during the Yuma surge event of July 12-15, 2004 (Section 3.3) highlighted the possible role of convective outflows in enhancing up-GoC low-level flow. Rogers and Johnson (2007) also attributed the observed amplification of the surge to the nocturnal GCLLJ together with convective outflows disturbing the inversion layer over the GoC. Apart from the intrinsic importance of predicting MCS events over the region for water resources management, understanding MCS variability is important for explaining the diurnal variability of low-level flow over the northern GoC. In this section, we examine the role of satellite-identified MCSs (Section 4.1) in modulating the diurnal cycle of the GoC low-level circulation during Yuma surge and non-surge environments. Yuma surges were defined earlier as major surges lasting 2-3 days, which are more likely to extend over the entire GoC. In particular, these surge environments will be composited, based on the occurrence (or absence) of MCSs, to study their impact in the initiation of minor surges. Recall that minor surges are defined as short lasting surges (~hours to a day) confined to the central and northern GoC (Section 1.1).

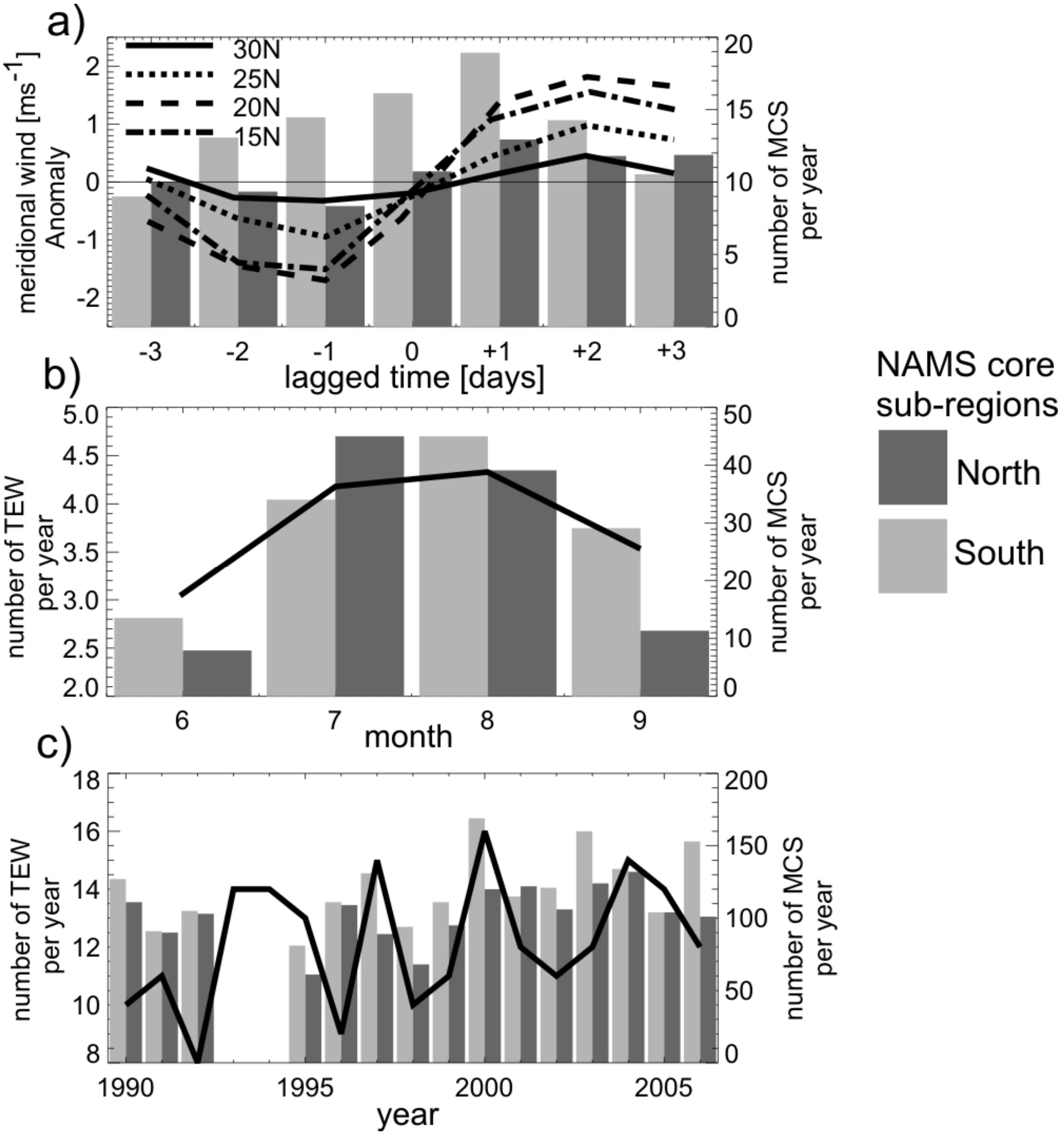

Figure 33. Relationship between TEW activity and MCS events over the NAMS core regions, dark (light) grey for southern (northern) regions (see Figure 2a). a) time-lagged analysis about TEW passage of meridional wind anomaly at 650 hPa (105ºW) for different latitudinal bands (centered at 15, 20, 25, and 30ºW with 5º width) (lines; left ordinate) and MCS number for regions 1 and 2 (bars; right ordinate). b) monthly mean TEW number (solid line; left ordinate) and MCS number (bars; right ordinate). c) annual numbers of TEWs (solid line; left ordinate) and MCSs (bars; right ordinate) for the June-September period.

Figure 34 shows the diurnal cycle of MCS genesis activity over the central and northern GoC coastal plain (CP) and western foothills of the SMO, for surge and non-surge environments. While we defined surge days (29% of the time) based on Yuma observations (Section 4.2), the non-surge days (71%) are just those days 24 hours before and 24 hours after Yuma surges. In general, MCS activity at any time during surge days exceeds those of the non-surge days, but the MCS phase remains nearly unchanged (Figure 34). It has been assumed in this research that this remarkable diurnal cycle of MCSs activity, which extends from late afternoon until early in the morning, influences the nocturnal GCLLJ intensity partly through convective outflows that are channeled northward along the GoC.

Figure 35 shows the vertical structure of along-GoC wind composited using 6 years of routine pilot balloon observations at Puerto Peñasco (located over the northern end of the GoC, see station 76061 in Figure 5) for surge and non-surge conditions, and whether they were associated with MCS and non-MCS events over the GoC CP. We further stratified the soundings based on time relative to the MCS occurrence into "before" (Figure 35a) the MCS started during the afternoon and "after" (Figure 35b) the MCS decaying stage early during the morning. The composites show the nocturnal development of the LLJ-type profile regardless of the environment, confirming this is a feature of the time-mean flow (Douglas at el., 1993). Some striking differences stand out when comparing surge and non-surge days at all times of the day (before and after). In agreement with previous studies (Anderson et al., 2001), the northern GoC exhibits stronger up-GoC low-level flow during surge days, differences that extend up to 2500 m compared to the non-surge days. Early in the morning (Figure 35b), there are also differences in the altitude of the maximum winds, with surge days having a deeper wind maxima (500 m), compared to the shallower maxima (350 m) during non-surge days. The occurrence of MCSs also appears to affect the mean wind profiles at this site. During the afternoon and morning hours, MCS-days exhibit stronger low-level southeasterly flow during both surge and non-surge days when compared with non-MCS days.

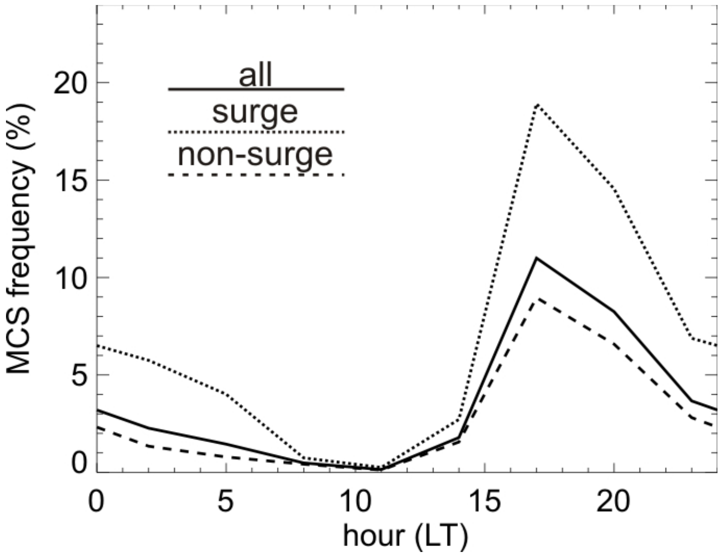

Figure 34. Diurnal cycle of MCS frequency for all MCS events (solid line) and for MCSs events during surge (dotted line) and non-surge (dashed lines) conditions in the northern GoC coastal plain region for the summers of 1990-2006. Time shown is local time (+0700 during the summer time from UTC) and indicates when the cloud-top clusters first met the MCS's criteria described in Section 4.1.

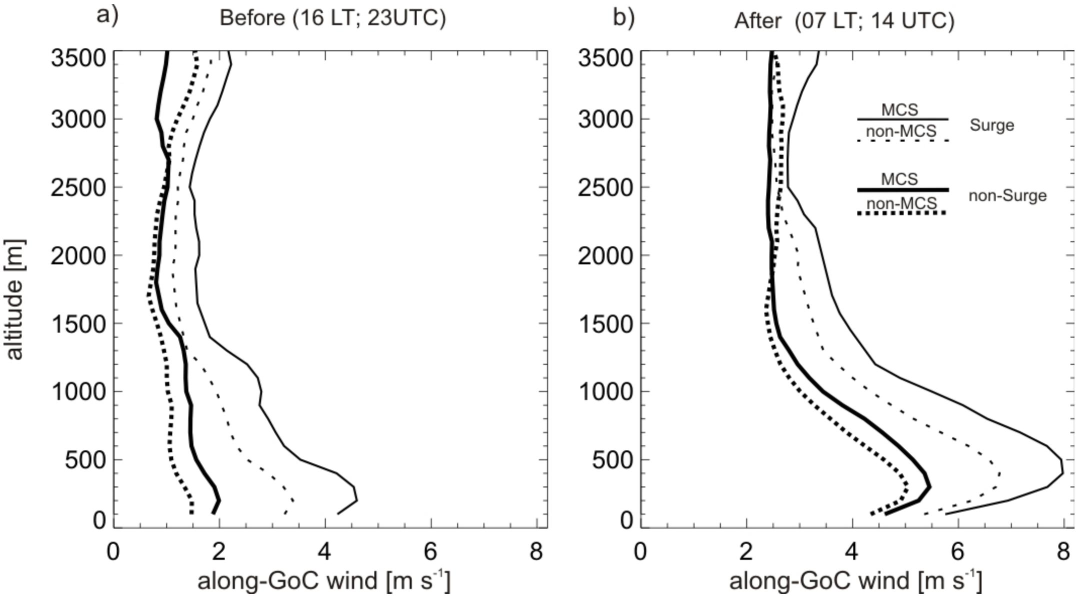

Figure 35. Along GoC wind using Puerto Peñasco pibal observations (1999-2005). This pibal site is collocated with station 76061 in Figure 5. Wind soundings are stratified based on surge (thin lines) and non-surge (bold lines) days and whether they are associated with an MCS (solid lines) or non-MCS (dotted lines) event in the northern half of the GoC coastal plain. Soundings are also averaged during (a) afternoon hours (~16 LT; 00 UTC) typically before the MCS genesis time and (b) early morning (~07 LT; 14UTC) typically after the MCS's decaying stage.

We extended the analysis shown in Figure 35b for different stations (pilot balloon and radiosonde winds) over the GoC region in order to show the spatial impact of the enhanced convective environment for MCS events relative to non-MCS events, during both surge and non-surge days (Figure 36). At low-levels (400-600 m), MCS occurrence over the CP region tends to produce enhanced southeasterly flow over the central and northern GoC region, while weakening the typical southeasterly flow over the southern GoC. This low-level diffluent pattern, which seems to be stronger for surge days compared to non-surge days, indicates that the wind field is responding to the low-level MCS pressure anomalies and the MCS's convective outflow. During surge days, this is a clear indication that MCS events, not necessarily independent of the major surge by itself, are partially responsible for the diurnal and day-to-day variability, which supports Rogers and Johnson (2007) and also the results shown in Section 3.3. At mid-levels (3000-3200 m), the MCS days for both non-surge and surge days exhibit a cyclonic vortex in the difference field over the central and southern GoC, together with an anticyclonic vortex over the northern GoC and SW USA. Enhanced southeasterly flow over the southern GoC and easterly to northeasterly flow over the central and northern GoC seem to favor MCS development. This cyclonic vortex in the difference fields has been associated with westward propagating disturbances originating in southern Texas or tropical waves propagating from over central and southern Mexico (Douglas and Leal, 2003). The vortex intensity might provide predictive value for MCS development over the central and northern GoC domain. This result is consistent with the relationship found between the MCS's frequency and TEW passage over Mexico discussed earlier in Section 4.4. The enhanced horizontal shear (not shown) seems to be a crucial ingredient for long-lived MCSs to develop in the region (Jirak and Cotton, 2007).

The analyses above represent few sites and rather infrequent and relatively short (~ 6 years) historical records over the GoC domain. Therefore, we also used 3-hourly NARR observations to provide a better spatial - temporal evolution of the influence of MCSs over the GoC domain and to explore how well the NARR captures the flow perturbation likely induced by convective activity. Such use of the NARR is justifiable, since previous research showed that NARR wind field diurnal cycle and various mesoscale flow patterns in the GoC domain seem to compare favorably with observations (Mo et al., 2005).

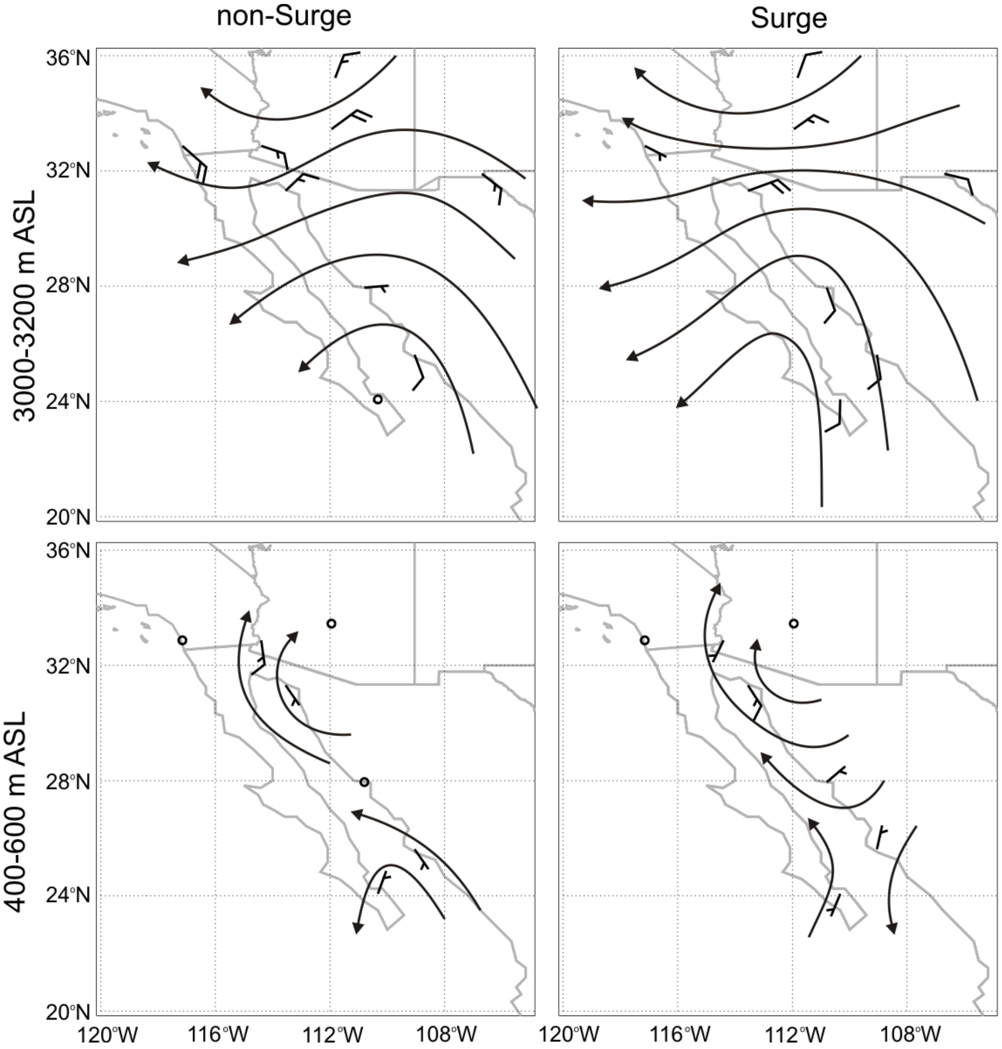

Figure 36. MCS minus non-MCS wind analyses at 1200 UTC for non-surge (left panels) and surge (right panels) days at different sites located along the GoC. Top (bottom) panels show the analyses averaged over the 3000-3200m (400-600m) layer. Half barb represents 0.5 m s^{-1}, while a whole barb represents 1.0 m s^{-1}.

Pre-MCS low-level flow (00UTC) is characterized by slightly stronger southeasterly wind compared to non-MCS days, not only over the GoC basin but also in the eastern Pacific (Figure 37). This feature, as mentioned above, is not necessarily independent of the occurrence of MCSs over the coastal plains and the western flank of the SMO. However, in a pattern that is stronger from 06UTC to 15UTC, MCS events are associated with enhanced up-GoC flow in the northern GoC half and down-GoC over the southern half. Although the NARR composites for surge days show a slightly weaker structure (Figure 38), they also show a zone of diffluent flow in the central GoC during early morning hours (09-15UTC). These features are consistent with the composite results based on upper-air observations shown in Figure 36. Thus, the mean MCS effect (combining surge and non-surge days) is to enhance up-GoC flow over northern GoC and down-Gulf flow over southern GoC. At mid-levels (not shown), consistent with the results presented earlier in Section 4.4, difference fields show that MCS events are associated with enhanced easterly flow over the central and northern SMO.

The GCLLJ and minor surges

Some aspects of the dynamical mode of the GCLLJ still are unclear. The GCLLJ is a persistent component of the time mean flow (Douglas et al., 1993). Results presented in this section showed that different synoptic conditions, such as those associated with surge and non-surge days, produce diurnal and day-to-day variability on the mean jet in agreement with numerical simulation studies (Stensrud et al., 1997; Anderson at al., 2000, 2001). We also showed that MCSs in the vicinity and upstream of the GCLLJ core region, play a slight to moderate role in such variability. Within the preexisting up-GoC channeled flow, MCSs may be capable of producing short-lasting (~6-12 hr) positive pressure gradient anomalies that strengthen southerly winds over the northern GoC and weaken the southerly flow over the southern GoC (see Figure 39).

There are important forecasting issues associated with the convective activity in the NAMS core region. In particular, MCS development seems to require specific ingredients, which include enhanced moist southeasterly low-level flow combined with enhanced mid-level easterly flow. These conditions reinforce the already strong diurnal forcings induced by the sea-breeze convergence and upslope flow over the western foothills of the SMO. Conversely, the correct simulation of MCSs (their timing and intensity) in the NAM core region may have an upscale effect in the correct simulation of the GoC low-level flow with a significant impact on the transient components of the NAMS.

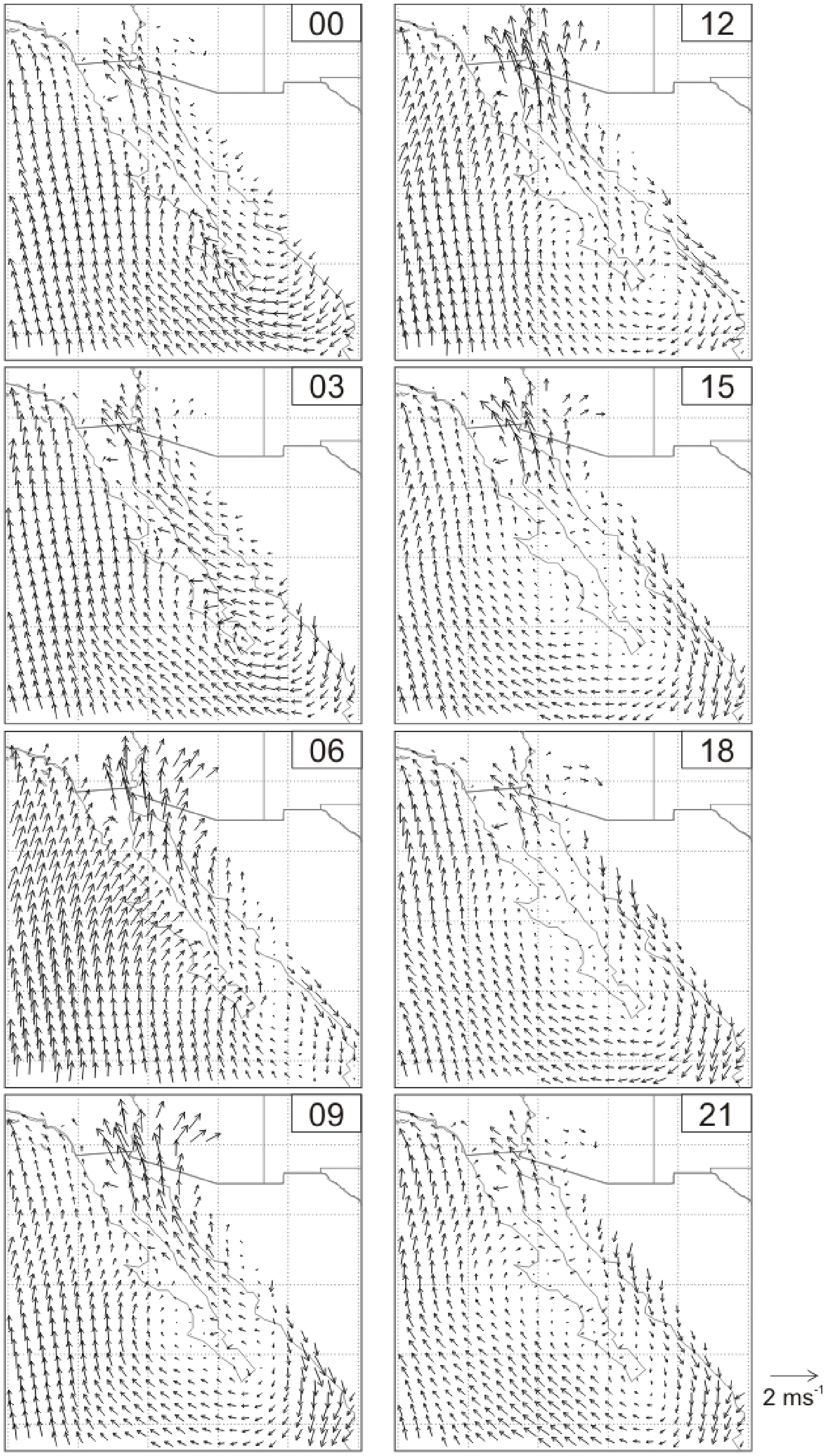

Figure 37. Evolution of MCS event minus non-MCS event NARR wind field at 950 hPa for non-surge days from 00 UTC (17LT) to 21 UTC (14LT). Wind vectors are shown only every other grid point to avoid cluttering.

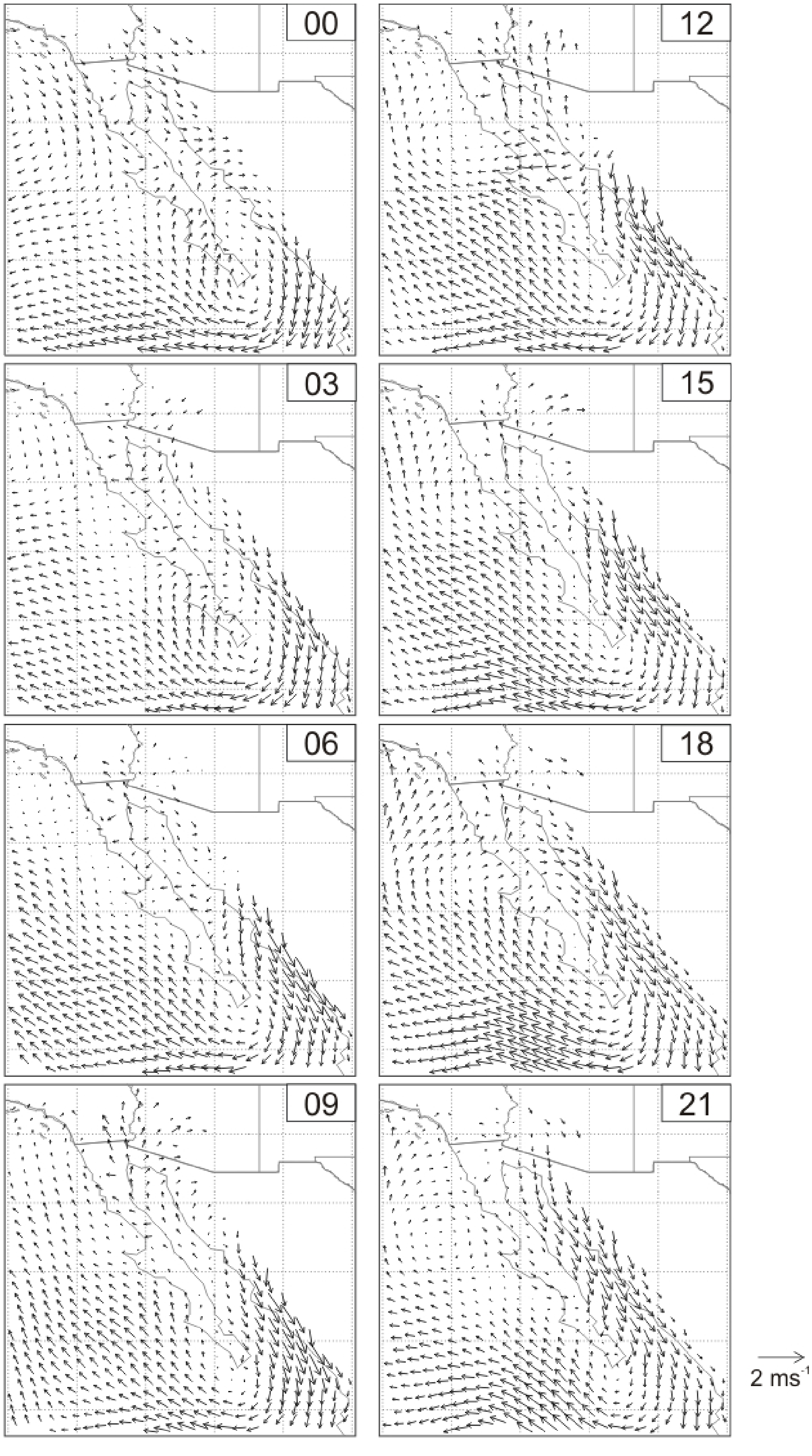

Figure 38. Same as in Figure 37 but for surge days.

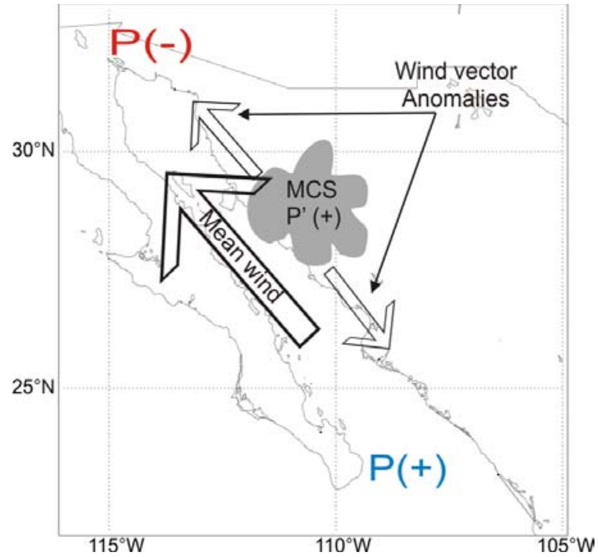

Figure 39. Conceptual model illustrating the effect of an MCS event acting upon the GoC low-level flow. Arrows indicate the direction of the mean flow (bold arrow) and wind anomalies (thin arrows). The net effect of the MCSs is to intensify (weaken) the wind speed over the northern (southern) end of the GoC.

4.6 Satellite Composites for Major Surges

Figure 40 shows composited cloud frequency differences (for cloud-tops with brightness temperatures colder than -38ºC (235.15ºK)) with respect to the average for all Control Surges. Over the eastern Pacific, all categories display a westward propagating pattern of relatively high frequency of cold cloud-tops, with a higher frequency of cloud-tops obtained for the TS/TC-related surges. These satellite composites of TS/TC-related surges show a similar pattern of convective activity to that previously presented for the surge event of July 12-15, 2004, using IR radiances (Figure 7). Of note in Figure 40 are the relatively high frequencies of cold cloud-tops to the south of the GoC entrance at days -2 to -1 for each surge category; not surprisingly, the non-MCS onset-related surges contain the weakest cold cloud-top signal. Some differences in the evolution of cloud frequencies between TS/TC- and TEW-related surges also are evident. TS/TC-related surges show a better-defined cold cloud mass, with the cloudiness of the TEW-related surges being less-well defined and confined to the GoC domain. The composites for all surge categories also reveal a northward-propagating feature along the eastern GoC, starting on day -2 over the Sinaloa-Nayarit coast, and moving to over northern Sonora by day zero and to over Arizona-New Mexico (AZNM) by day +1. This feature is consistent with the results of previous studies that relate the occurrence of surges to enhanced convective activity over AZNM region (Douglas and Leal, 2003; Higgins et al., 2004). Thus, there is a close relationship between the northward propagation of surges and the anomalies of convective cloudiness, with more accentuated anomalies during TS/TC- and MCS onset-related surges.

Not surprisingly, MCS onset-related surges and non-MCS onset-related surges show differences associated with the surge onset (Figure 40). In the case of MCS onset-related surges, the convective activity evolution seems to resemble those of the TS/TC-related surges. However, only 35% of the MCS onset-related cases also were associated with TS/TC-related surges. Even though the non-MCS onset-related surge events lack convective activity during early stages of the surge, the mean cloud frequency composites (Figure 40) show some convective activity occurring around day zero in the upper-GoC and SW United States. For the non-MCS-related surges, 35% of the cases were associated with TS/TC-related cases, 45% with TEW related cases, and the remaining 22% of the cases were unrelated to any type of aforementioned synoptic-scale tropical disturbance. The lack of an active convective environment during non-MCS onset-related surges suggests the existence of different surge triggering mechanisms, unrelated to MCS convective outflows, for these events. Other plausible triggering mechanisms were discussed in Section 3.3.

The overall difference between surge types can be seen by averaging the satellite composites from days -2 to -1 (“before” Yuma surge onset) and days +1 to +2 (“after’ Yuma surge onset). Figure 41 contrasts the “before” and “after” mean frequency differences of cloud-top brightness temperature (Tb) < -38ºC between the MCS and non-MCS onset-related surges for the Control Surges, and the TS/TC- and TEW-related surges. These results suggest that the pre-surge convective activity is associated with significant changes in the convective environment over the NAM region. Not surprisingly, before the Yuma surge onset, MCS onset-related surges show more cold cloud-tops to the south of the GoC entrance. The MCS onset-related

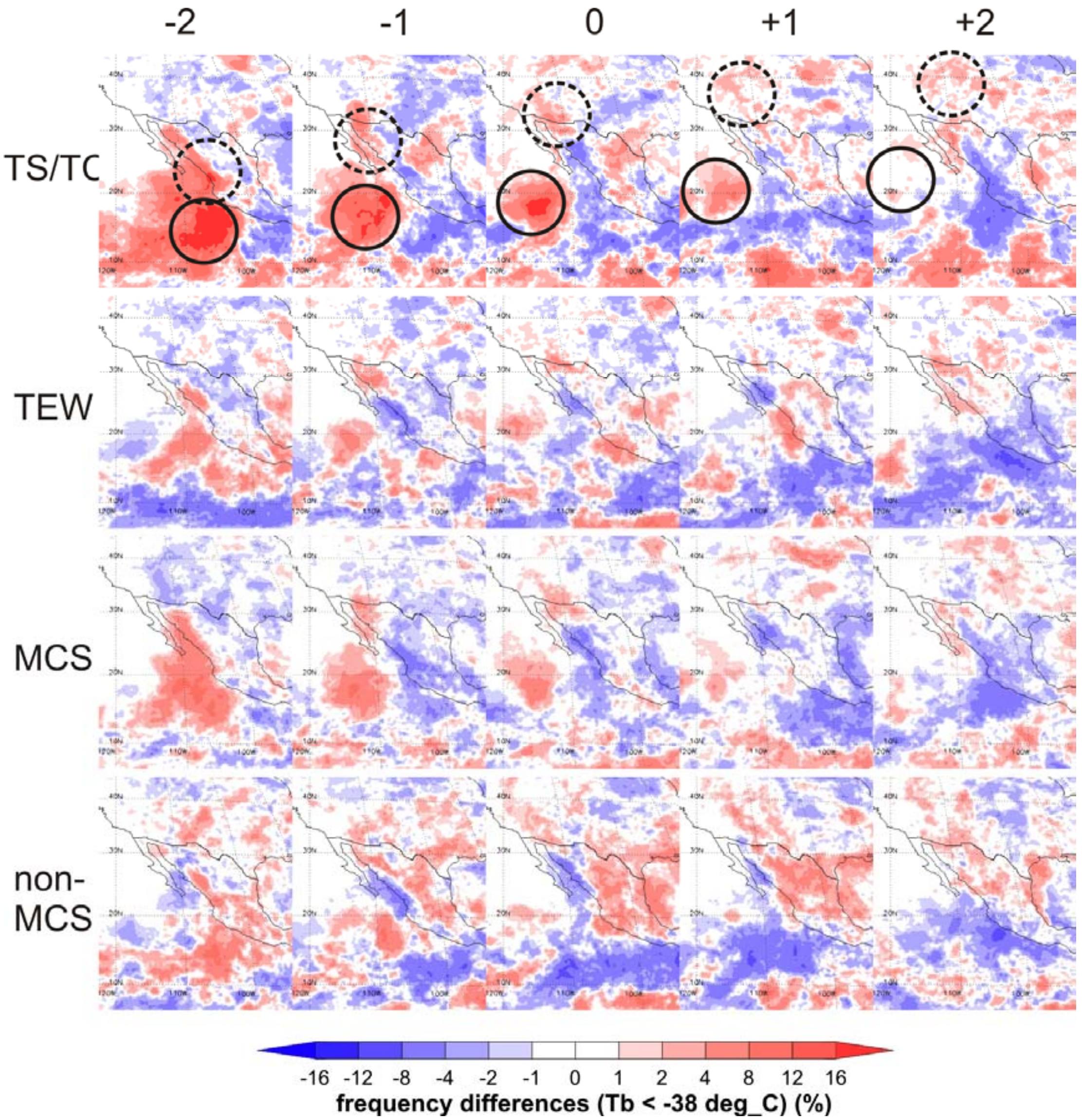

Figure 40. Composites of satellite cloud frequency differences for cloud-top brightness temperature (Tb) < -38°C for TS/TC, TEW, MCS, and non-MCS related surge evolutions extending from 2 days before (-2) to 2 days after (+2) surge onset at Yuma, AZ. Cloud frequency differences are with respect to Control Surge average Tb. Solid (dashed) line circle for TS/TC composites show the location of the westward (northward) moving high cloud frequency core mentioned in Section 4.6.

surges for all categories show striking differences in the convective fields, with less cold cloud-tops over the SMO foothills and more cold cloud-tops over Sonora. This contrast is more accentuated for TS/TC-related surges. Additionally, there are noticeably less cold cloud-tops over the AZNM region for all categories. After the Yuma surge onset, the SMO foothills and GoC coastal plain show less cold cloud-tops for MCS onset-related surges than for the non-MCS onset-related surges. Significant differences also are observed over the Southern Great Plains of the United States and SW United States (Figure 41). MCS onset-related surges seem to have decreased convective activity over the AZNM region that contrasts with enhanced convection over the Southern Great Plains. Surprisingly, these results contrast with Higgins et al. (2004) who showed that the overall impact of surges over SW United States was significantly modulated by the relative location of the upper-level monsoon anticyclone during the surges. Nevertheless, this condition could still hold since we have not assessed the occurrence of enhanced convective activity over the GoC as a function of the relative location of the upper-level monsoon anticyclone.

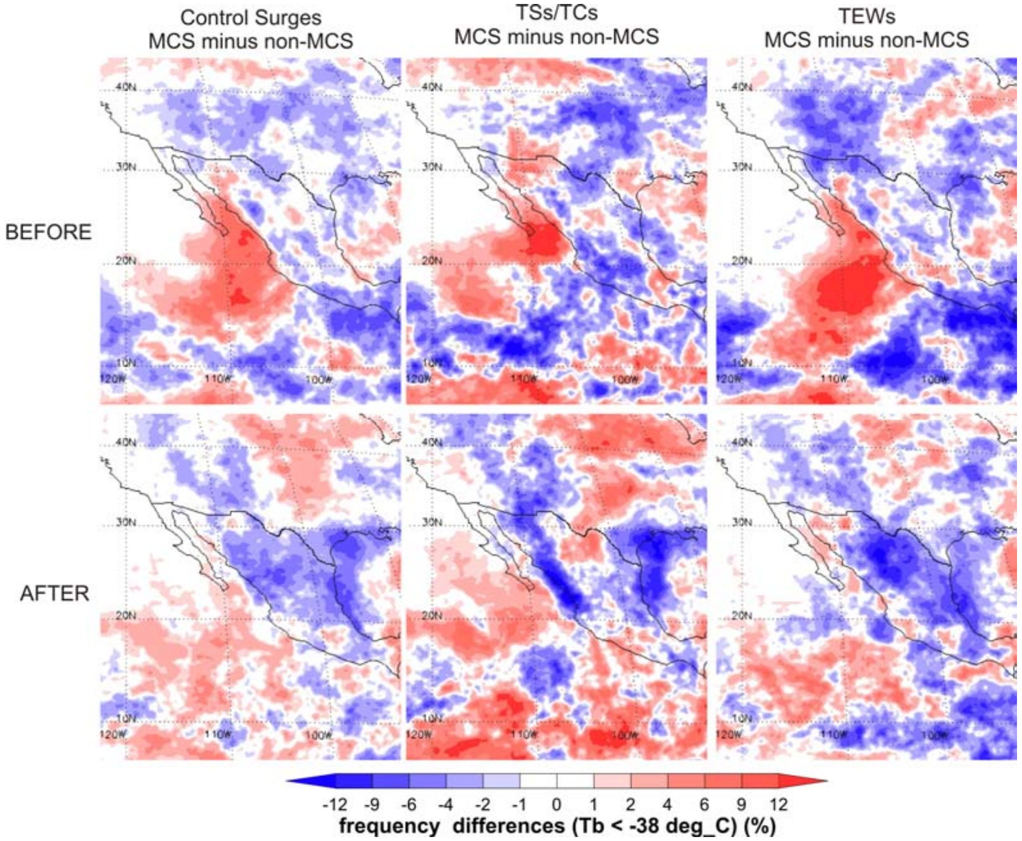

Figure 41. Mean cold cloud-top frequency differences (for brightness temperatures colder than -38 ºC) between MCS onset-related surges and non-MCS onset related surges for Control Surges (left panels), TS/TC related surges (center), and TEW related surges (right). Differences are calculated relative to Yuma surge onset from days -2 to -1 ("before"; top panels) and days +1 to +2 ("after"; bottom panels). Positive frequency differences (shades of red) indicate the areas where the MCS onset-related surges are more convectively active, and negative differences (shades of blue) indicate the areas where the non-MCS onset-related surges are more convectively active.

The next section further explores the possible physical mechanisms that could explain the observed evolution of convective activity and the relatively large impact that the pre-surge convective activity has over surge evolution in the NAM region.

4.7 Wind and Moisture Composites for Major Surges using NARR

4.7.1 Yuma surges from NARR

The mean wind and humidity fields of the major moisture surges are composited using the NARR products according to the organized convective activity (as categorized in Section 4.1) and their triggering mechanisms (categorized in Section 4.2) detected in the region during each surge's lifetime.

Figure 42 shows the evolution of key atmospheric anomalies during the Control Surges, to highlight the mean low- and mid-tropospheric features during surge genesis. The composite evolution was from two days prior to the Yuma surge onset to two days after the Yuma surge onset, and the anomalies are relative to the average quantities during this evolution period. The main feature in the evolution of the 925 hPa anomaly wind field is the surge-related structure (anomalous southeasterly winds) along the GoC. Enhanced southeasterly winds and positive specific humidity anomalies are evident at the GoC entrance at day -1 over the southern GoC region, with northward propagation along the GoC during subsequent days. Using 3-hourly analyses (not shown), these southeasterly winds propagate up the Gulf at an average speed of 10 m s^{-1}. Higgins and Shi (2005) found a similar speed, regardless of the surge type, in a study that treated TS/TC- and non-TS/TC-related surges. Low-level northwesterly winds to the west of Baja California weaken as the mean surge leading edge advances. This propagating pattern shows that the horizontal distribution of the surge extends beyond the GoC, to over Baja California and into the eastern Pacific. During days +1 to +3, a significant increase in specific humidity is evident over the SW United States. Meanwhile the amplitude of southeasterly wind anomalies decays noticeably along the GoC, until reversing to northwesterly wind anomalies by day +3.

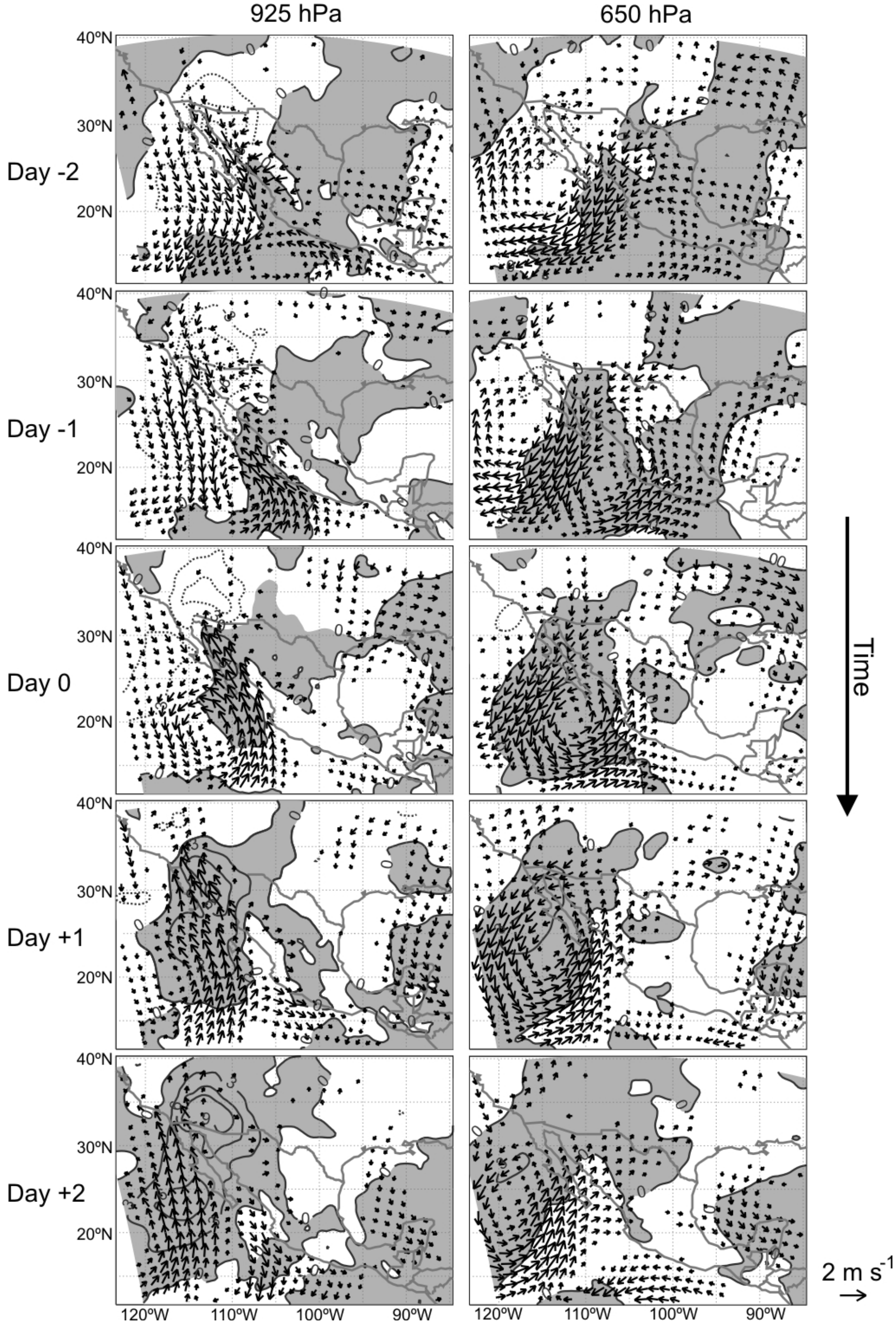

Figure 42. Evolution of average wind vector and relative humidity anomalies during Control Surge lifetime (relative to lifetime mean) at 925 hPa (left panels) and 650 hPa (right panels). From top to bottom, the panels present average anomaly patterns for -2, -1, 0, +1, and +2 days relative to Yuma surge onset. Shaded (dotted) contours show regions of positive (negative) specific humidity anomalies at 3 g kg^{-1} intervals. For clarity, only every fourth wind vector anomaly with magnitude grater that 0.5 m s^{-1} is displayed.

Figure 42 shows a clear link between the low-level surge-related structure and the mid-level westward propagating trough. At 650 hPa, a westward propagating trough is indicated by the anomalous cyclonic vortex throughout the composite evolution, which is associated with positive specific humidity anomalies. At day -2, this feature is located over central Mexico, after which it moves to about 120°W over the eastern Pacific by day +2. This feature shows a northeast to southwest orientation with its circulation center tilting slightly to the east with height of the low-level vortex center (not shown).

4.7.2 Composites from NARR surface and QuikSCAT winds

We now assess the quality of the NARR surface wind products as a tool to diagnose the surge characteristics over the ocean by comparing NARR 10m winds against the QuikSCAT winds. QuikSCAT winds constitute an independent data set, even though its quality still is under continuous testing, to evaluate the average environmental conditions associated with surge genesis over the eastern Pacific such as these associated with TS/TC and TEW environments (Chelton et al, 2006). Figure 43 shows the evolution of the along-GoC surface wind components for Control Surges averaged over three different sites distributed along the GoC. Although this is not a thoroughly assessment of the quality of either data set, systematic differences clearly stand out. During the surge lifetime, NARR surface winds appear to be greater than QuikSCAT by 2-3 ms^{-1}. However, the variations about Yuma surge onset (Day 0) associated with the surge passage over the GoC seem to be well-represented in either data set, with the QuikSCAT winds showing slightly larger amplitude compared to the NARR surface winds. The differences between these two datasets may reflect: the deficiencies of the QuikSCAT data over the GoC such as spatial resolution problems over the GoC (with characteristic width of ~ 150km), the twice-daily sampling strategy, or rainfall contamination in the estimation of the QuikSCAT surface winds that may be associated with moisture surge environments. Also, the results obtained agree with different studies showing that NARR overestimates the up-GoC low-level winds over the northern GoC (Mo et al., 2005; Ciesielski and Johnson, 2008). In particular, Ciesielski and Johnson (2008) found that,

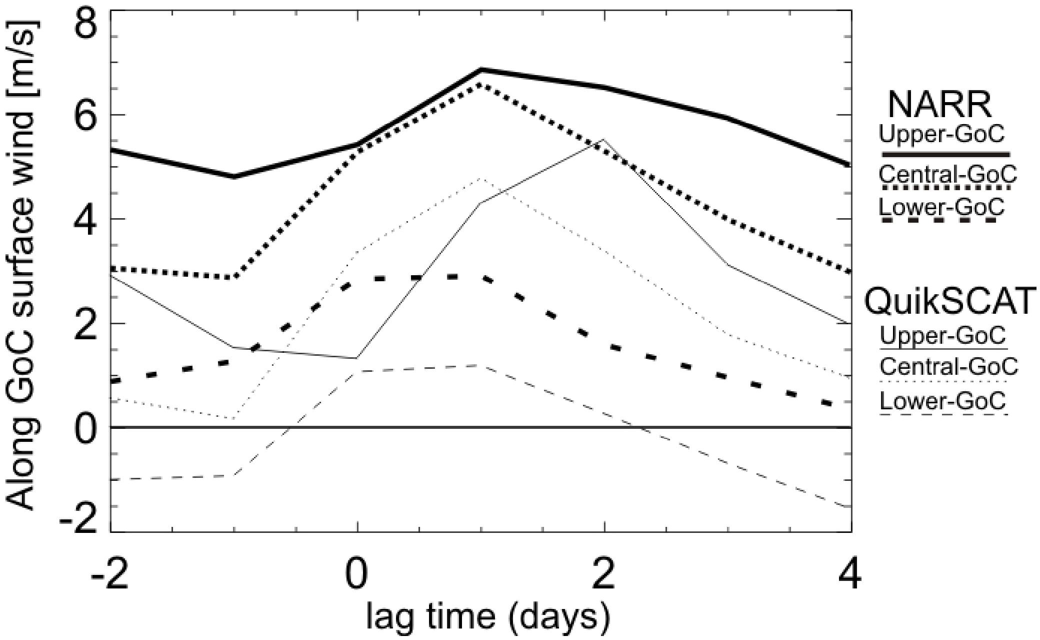

Figure 43. Evolution of the along-GoC surface wind component about Yuma surge onset (day 0) using NARR (heavy lines) and QuikSCAT (thin lines) winds. Surface winds are average over a circle domain of radius 0.5° located along the central axis of the GoC at three different sites: Upper- (solid), Central- (dotted), and Lower- (dashed) GoC.

even when NARR assimilates the special upper-air and surface observations made during the NAME EOP, the mean up-GoC flow is systematically stronger when compared with QuikSCAT surface winds.

Figure 44 shows the spatial-temporal characteristics of Yuma surges based on NARR surface wind and QuikSCAT winds. In general, these composites show the same low-tropospheric features mentioned earlier in this section (Figure 42). The composites developed using both data sets are in good overall agreement for the spatial-temporal characteristics of ocean surface wind anomalies. A significant shift from northwesterly to southeasterly surface wind anomalies is observed during the evolution of the surge events over both the eastern Pacific and the GoC. The GoC region shows a striking enhanced southeasterly wind associated with the surge onset (Figure 44). These composites show that the Control Surges are associated with coherent structures that extend to the south of the GoC entrance, which further illustrates the synoptic-scale of the

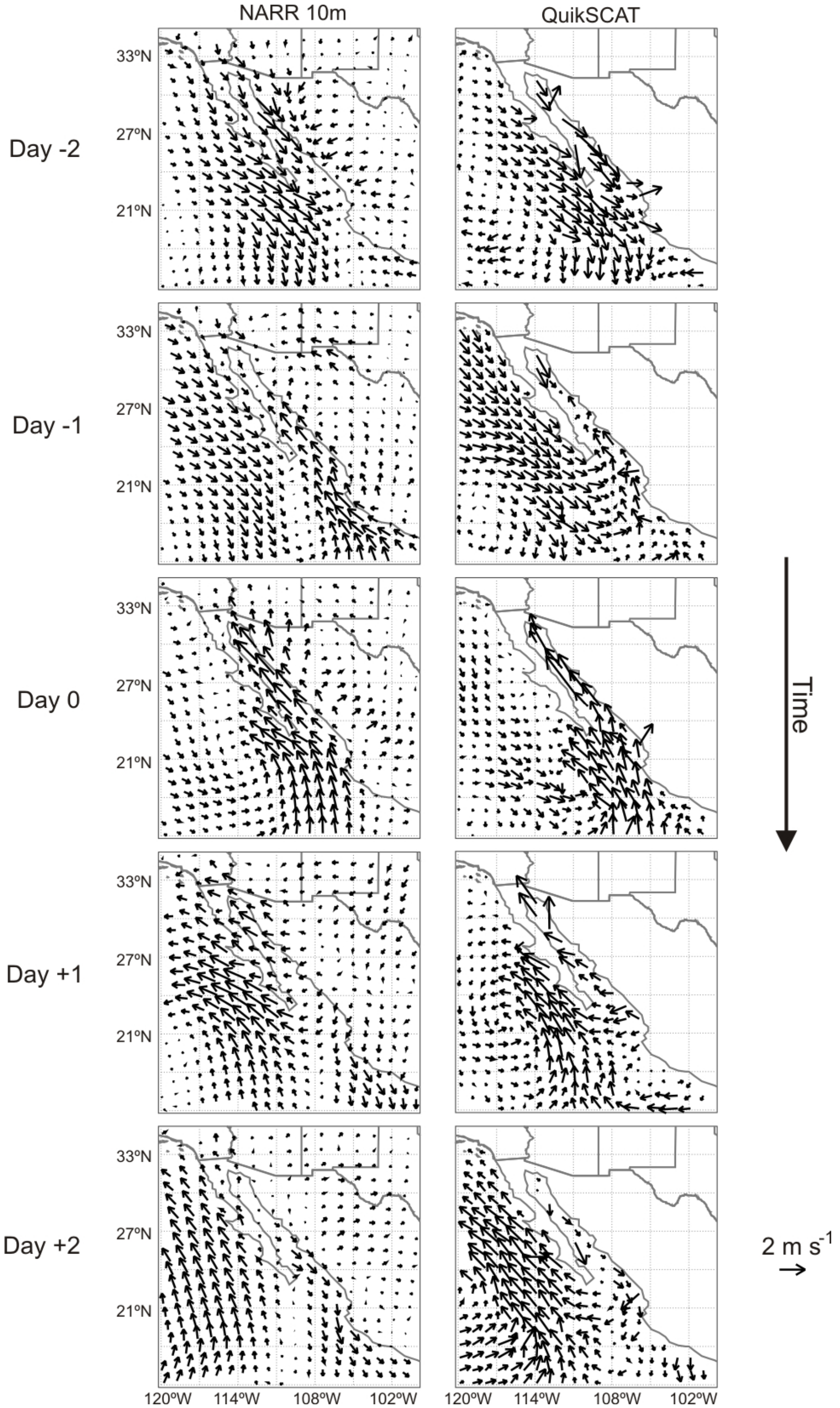

Figure 44. Evolution of average surface wind vector anomalies during Control Surge lifetime (relative to lifetime mean) using NARR wind data (left panels) and QuikSCAT SeaWinds retrievals (right panels). From top to bottom, the panels present average anomaly patterns for -2, -1, 0, +1, and +2 days relative to Yuma surge onset. For clarity, only every fourth wind vector anomaly is displayed.

surface perturbations observed at Yuma. We emphasize that the definition of Control Surges used here does not guarantee that all moisture surges were triggered south of the GoC entrance. However, the timescale constraint imposed in our definition of Control Surges (lifetimes of 2-5 days, Section 4.2) and the spatial-temporal coherence of their composited surface wind field anomalies (Figure 44) confirm that the surges are mainly associated with synoptic disturbances moving westward to the south of the GoC entrance (Figures 43 and 44).

4.7.3 Effect of convective activity during moisture surge onset

We now narrow the focus to the main goal of this chapter, which is to determine the effect of convective activity on surge evolution. Figure 45 shows results for the wind and specific humidity based on mean evolution composites of MCS minus non-MCS onset-related surges. At 925 hPa, more humid and stronger early surge conditions are associated with MCS onset-related events. The wind differences are stronger for early stages of the surge, from -2 to 0 days relative to Yuma surge onset, compared to the differences after the surge onset. On the other hand, moisture differences remain positive over the GoC and AZNM regions throughout the evolution composite. This enhanced low-level moisture during MCS onset-related surges is associated with a decrease in convective activity (section 4.6) over the AZNM region. Although these may appear to be counterintuitive, the situation agrees with Wallace et al. (1999) who noted that Phoenix forecasters have observed that strong moisture surges reduce the likelihood of thunderstorms in the short term. They argued that even though a surge brings in more humid air that may increase potential instability, its coolness at the lowest levels may require more daytime heating and deeper lifting (hence more work) to release this instability. The exact mechanisms associated with this feature are explored later in this chapter.

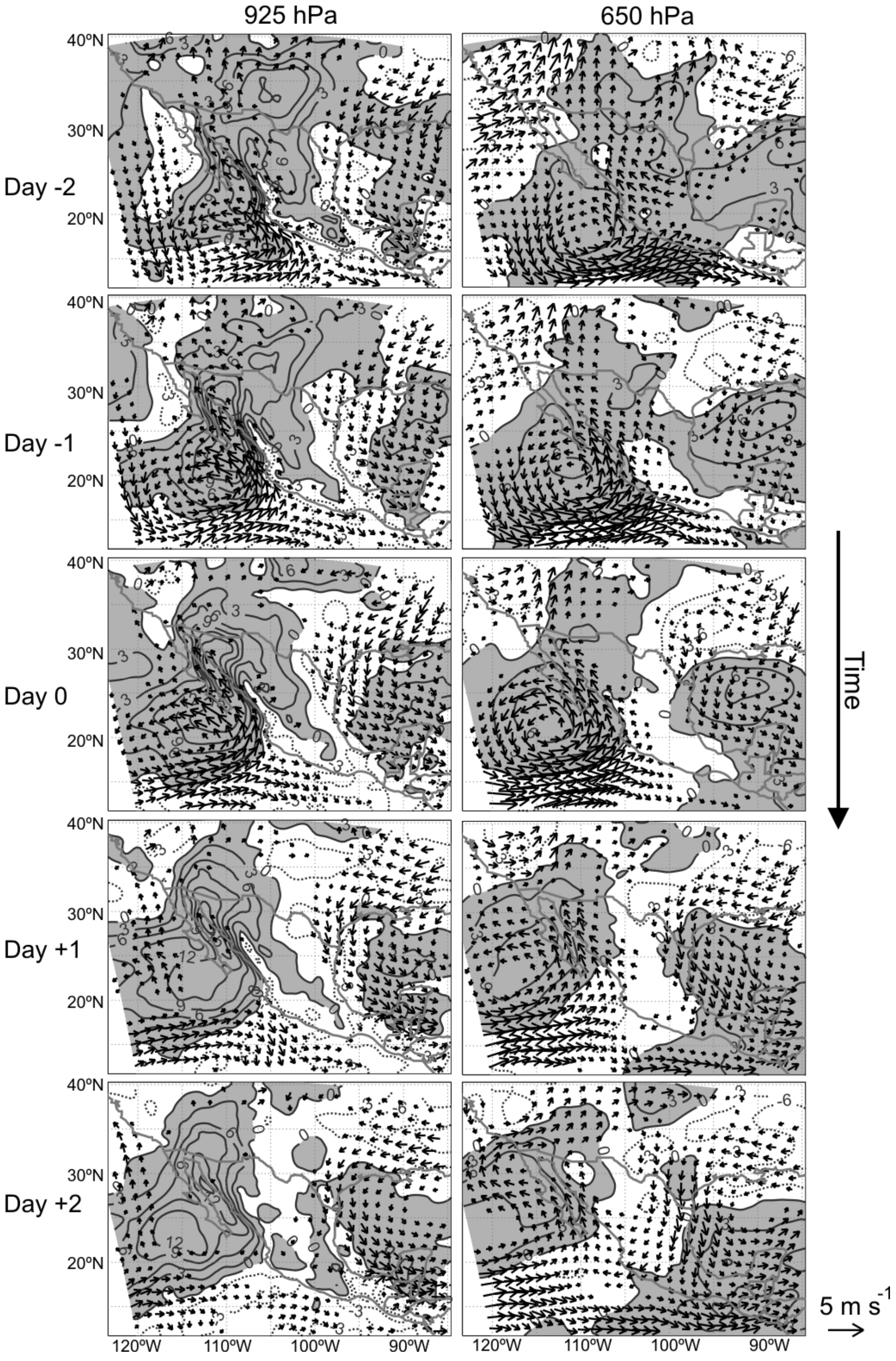

Figure 45. Evolution of average wind vector and relative humidity differences between MCS onset-related and non-MCS onset-related surges at 925 hPa (left panels) and 650 hPa (right panels). From top to bottom, the panels present average difference patterns for -2, -1, 0, +1, and +2 days relative to Yuma surge onset. Shaded (dotted) contours show regions of positive (negative) specific humidity differences at 3 g kg^{-1} intervals. Wind vector differences only are plotted where the differences between MCS onset-related and non-MCS onset-related surges exceed the 95% confidence level using the Student's t-test. For clarity, only every fourth vector difference is displayed.

The westward moving enhanced cyclonic vortex to the south of the GoC entrance at low- and mid-levels (Figure 45), associated with MCS onset-related surges, suggests that these surges also are associated with the intensity of the cyclonic rotation of TSs/TCs and TEWs. However, the number of TS/TC- (or TEW-) related surge events in the MCS onset-related surge sample (Table 4) is greater than the number for non-MCS onset-related surges. Such differences in the sample sizes for the composites may cause the enhanced cyclonic vortex to the south of the GoC entrance associated with the wave development. Therefore, we performed a simple test involving random selection of an equal number of TS/TC and TEW events associated with each sample of MCS and non-MCS onset-related surges (not shown). This test revealed that the results in Figure 45 are consistent and independent of the number of TSs/TCs or TEWs used in the composites. It confirms that the convective environment in this region (southern GoC and E. Pacific) does affect the surge response as initially suggested by Hales (1972) and Brenner (1974), making the surge more intense by increasing up-GoC low-level moisture flux. The physical mechanisms responsible for the surge enhancement could include an increase of the north-south thermal gradients, superposition of convective outflows and subsequent gravity currents on the mean flow, or the enhanced anomalous cyclonic vortex interacting with topography in western Mexico. The characteristics and the possible impact of these physical mechanisms on the enhanced southeasterly flow are discussed below.

4.7.4 Lower tropospheric thermal structure before Yuma surges onset

Figure 46 shows the 950 hPa potential temperature and 1000-700hPa thickness structures before the surge onset (day -1) for MCS minus non-MCS onset-related surges. The relatively colder/thinner feature along the southern Sinaloa and Nayarit coast to the south of the GoC entrance illustrates the effect of the enhanced convective activity associated with MCS onset-related surges. This thermal structure may be explained by cold pools (produced by diabatic cooling associated with the evaporation/sublimation within the unsaturated PBL) commonly observed during MCS environments (Zhang and Fritsch, 1988; Knievel and Johnson, 1998) or reduced incoming shortwave radiation due to enhanced cloudiness (Brenner, 1974). Thus, MCS onset-related surges are associated with stronger southeasterly flow (Figure 45) partially due to the pressure gradient that builds up in response to convectively generated thermal contrast (Figure 46). Other factors possibly contributing to this enhanced southeasterly flow may be associated with the low- to mid-level cyclonic rotation located to the south of the GoC entrance, which in turn are presumably driven and controlled by tropical cyclogenesis processes. It is therefore of interest to understand the dynamical factors controlling such differences in the surge response, which is done next.

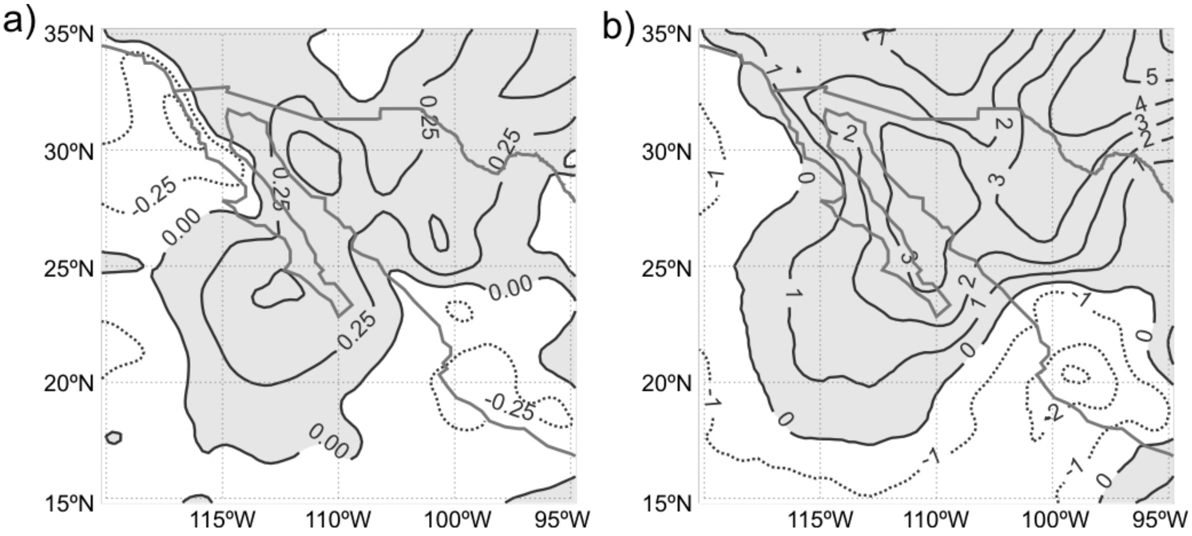

Figure 46. Average difference fields between MCS minus non-MCS onset-related surges at day -1 for a) potential temperature at 950 hPa [°K] and b) 1000-700 hPa thickness [gpm]. Solid (dotted) contours show regions of positive (negative) differences.

4.7.5 Momentum budget

A momentum budget analysis is performed to identify the dynamical forcings that enhance the southeasterly flow during the MCS onset-related surges. First, we consider the zonal and meridional components of the momentum budget equation written as

$$\frac{du}{dt} = \frac{\partial u}{\partial t} + u\frac{\partial u}{\partial x} + v\frac{\partial u}{\partial y} + w\frac{\partial u}{\partial z} = fv - \frac{1}{\rho}\frac{\partial p}{\partial x} - D_x \tag{4.2a}$$

$$\frac{dv}{dt} = \underbrace{\frac{\partial v}{\partial t}}_{LTC} + \underbrace{u\frac{\partial v}{\partial x} + v\frac{\partial v}{\partial y} + w\frac{\partial v}{\partial z}}_{ADV} = \underbrace{-fu}_{CO} \underbrace{-\frac{1}{\rho}\frac{\partial p}{\partial y}}_{PGF} \underbrace{-D_y}_{D} \tag{4.2b}$$

.

Here *u*, *v,* and *w* are the zonal, meridional, and vertical wind components, respectively; ρ is the air density; *p* is the pressure field at a fixed height; and D_x and D_y represent the diffusion of momentum through horizontal and vertical mixing, including turbulent friction. The terms on the expanded left side of the equations are the local time change (LTC) and advective (ADV) accelerations; the terms on the right side represent the Coriolis (CO) and pressure gradient (PGF) forces, and diffusion (D). To evaluate numerically the different terms in these equations, all variables were first interpolated to a constant-height grid at ~ 500m. The spatial gradients were calculated using a centered finite-difference scheme and the time differencing was performed using a forward differencing scheme. Finally, the diffusion terms (D_x and D_y) were estimated as residuals after calculating all other terms.

Figure 47 documents the evolution of the low-level (~500m) momentum budget terms (in Eqs. 4.2a and 4.2b) for a point located to the south (22.7°N, 108°W) of the GoC entrance for MCS and non-MCS onset-related surges. For both surge categories the flow approaches an Ekman balance (LTC + ADV = CO + PGF + D ≈ 0) in the zonal component (Tan and Wu, 1993), while the flow approaches geostrophic balance (CO ≈ PGF) in the meridional component. Around day 0, the low-level flow is dominated by the Ekman balance in the zonal direction, which involves at least ~200 km of cross-flow from the orographic barrier produced by the SMO (Figure 2). Thus, the pressure gradient terms tend to dominate the flow associated with both of these synoptic-convective patterns. However, Figure 48 highlights some differences in the pressure gradient terms observed in both surge categories that may help to explain, heuristically at least, the wind field differences observed earlier in Figure 45. A striking feature of Figure 48 is that the pre-surge (days -3 to -1) meridional PGF component is substantially larger for MCS onset-related surges than for non-MCS onset-related surges. This finding is consistent with the relatively colder (higher pressure) environment identified to the south of the GoC entrance during MCS onset-related events in Figure 46. The enhanced northward pressure gradient, in conjunction with the presence of the SMO barrier to the east, channels and accelerates the wind in the up the GoC direction. Meanwhile, the zonal PGF component associated the MCS onset-related events also is stronger on day -1 and supports stronger southerly near-geostrophic winds. These wind field differences are not sustained after day 0 (Figure 45), which also is reflected in the pressure gradient fields (Figure 48).

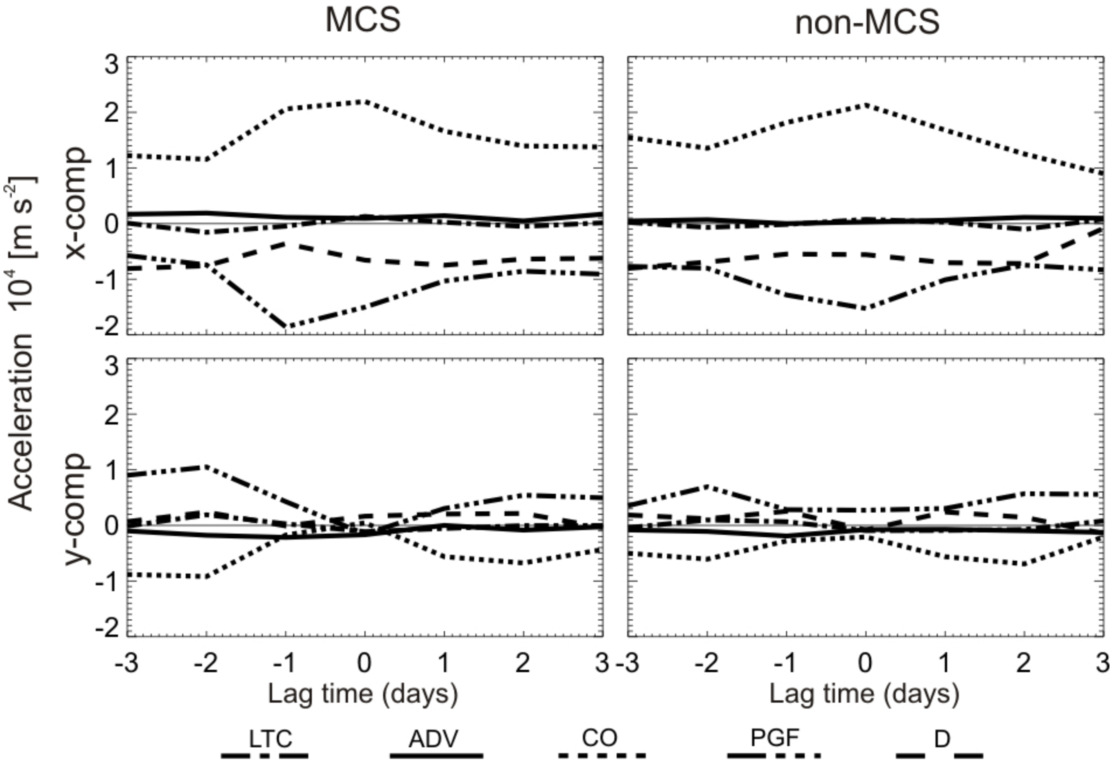

Figure 47. Evolution of low-level (~500m) momentum budget terms (zonal components in upper panels, meridional components in lower panels) for a point located to the south (22.7°N, 108°W) of the GoC entrance for MCS (left panels) and non-MCS (right panels) onset-related surge categories.

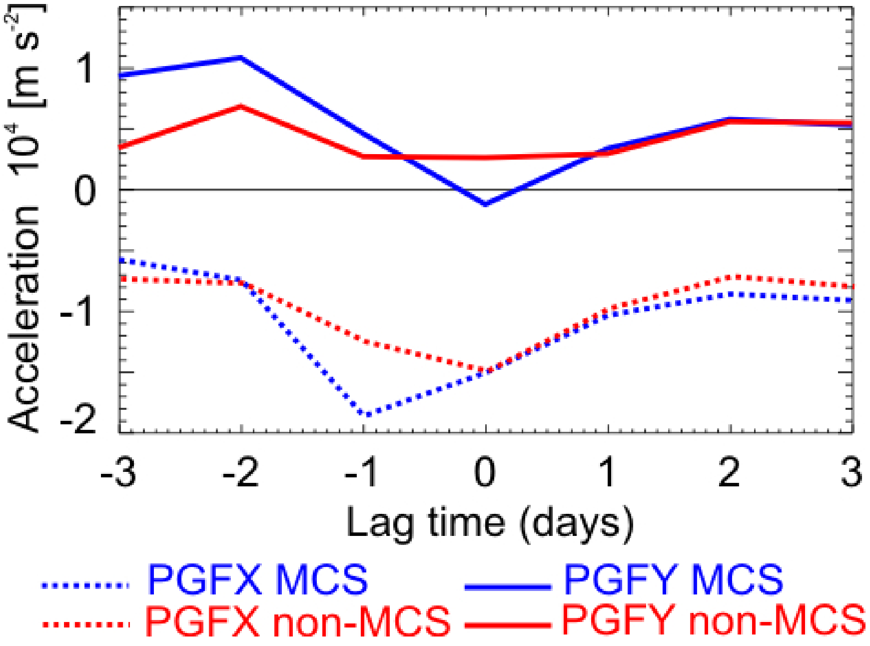

Figure 48. Comparison of PGF terms shown in Figure 47. Zonal (meridional) PGF components are givent by dotted (solid) lines. MCS and non-MCS onset-related surge categories are indicated by blue and red, respectively.

4.8 Concluding Remarks

The previous chapter highlighted the importance of convective activity in modulating the surge response during individual surge lifetimes. Consequently, this chapter has sought to elucidate further this importance of convective activity in a multiyear compositing framework. In this part of the research, NARR products were used to investigate the response of moisture surges to MCSs along the GoC and northeastern Pacific Ocean, to westward propagating disturbances such as TSs/TCs and TEWs, and to eastward propagating intraseasonal disturbances, such as MJOs. The result has been further documention of the intricate relationships of the multiscale processes associated with the NAMS rainfall variability.

Satellite composites showed that surges are associated with an enhanced convective activity signal that propagates northward along the GoC coast. This cloudiness seems to be tied to the northward propagation of the surge along the Gulf but the precise mechanisms for initiating the convection were beyond the scope of this research.

Wind composites based on upper-air data and the NARR suggest that MCSs over the GoC coastal plains play a noticeable role in the diurnal and day-to-day variability of the GCLLJ. For both surge and non-surge days, it appears that MCSs over the northern GoC coastal plains produce offshore convective outflows that directly accelerate the GCLLJ by advection of momentum and by increasing the offshore pressure gradient, which in turn enhances the up- (down-) GoC wind over the northern (southern) GoC. However, these relationships also are tied to another key finding of this research, which highlights the important role of synoptic disturbances (e.g. TEWs) in increasing the likelihood for MCS development within the GoC domain. Interestingly, MCSs over the GoC core region significantly increase during TEW passages, enhancing up-GoC low-level moisture flux. Regardless of these complex relationships, composite results for non-surge days (as defined in this research) document more clearly the relative role of MCSs in enhancing GCLLJ and up-GoC low-level moisture flux.

Higgins et al. (2004) found that the impact of surges on the southwestern US region, even when associated with TSs/TCs, depends highly on the location of the upper-tropospheric monsoon anticyclone. They concluded that wet and active convective environments over the southwestern US are to be expected when the axis of this anticyclone moves to the east of the core monsoon region, because the time-mean southeasterly flow at low-levels then complements a surge. Conversely, dry surges are expected when the ridge axis is to the west of the core monsoon region. However, the methodology implemented here suggests that a surge's response over northwestern Mexico and southwestern US also is sensitive to the presence of an easterly propagating disturbance (TS/TC or TEW) in conjunction with the amount of convective activity over the surge onset region. The most important feature of these results is that MCS activity in the lower GoC region tends to be associated with stronger surges. These findings stemmed from use of satellite imagery to identify MCS events, which identified rainfall events over oceans as well as land.

The observed surge frequency undergoes moderate changes as a function of intraseasonal variations related to the MJO. Results showed that surge frequency increases nearly 50% and 120% after the MJO active phase based on MJO CHI200- and OLR-based indices, respectively. Evidence of enhanced convective activity and increase in TS/TC numbers also were suggested to be associated with intraseasonal variations related to the MJO.

5 SENSITIVITY ANALYSIS OF SURGES USING THE ADVANCED RESEARCH WRF

Numerical simulations over the NAM core domain are described in this section. The objective is to investigate the sensitivity of the model to those physical representations associated with convective processes for surge and non-surge synoptic-scale environments. In sections 4.5 and 4.7, we showed that the effect of convective outflows induced by MCSs can have a significant effect on the low-level flow, even when the synoptic forcing is strong. In mesoscale modeling, is difficult to directly simulate the correct location and timing of organized convective activity (such as an MCS) and their associated convective outflow structures and other mesoscale characteristics (Stensrud et al. 2000). As discussed earlier, numerous studies have shown the strong impact that convective parameterization schemes can have on simulating organized convective events (e.g. Wang and Seaman, 1997; Jankov et al., 2005), rainfall patterns (Gochis et al., 2002), and timing and intensity of the diurnal cycle of convection (Gochis et al., 2002). Additionally, the multiscale interaction of the atmospheric processes within the NAMS core region poses an extreme challenge for mesoscale/regional models (Higgins and Gochis, 2006). With such extreme sensitivity to the parameterization of convection and precipitation alone, it is challenguing to evaluate the effect of convective activity on the low-level flow of the GoC domain.

The Advanced Research Weather and Forecasting model (known as ARW) version 3 was used in an idealized simulation mode. Near-idealized numerical simulations were performed to evaluate the sensitivity of various synoptic forcings to convective activity in the ARW model. We evaluated the model's response to realistic synoptic forcing and to imposed MCSs. Following descriptions of the model and the experimental design used, this chapter is divided in two sections. In the first section, simulations of the NAME surge event of July 12-15 are presented and compared with the observations presented in Section 2.1. This is intended to evaluate the model skill using different physical parameterizations.

The second section describes simulations using different initial and boundary conditions, representing surge and non-surge synoptic forcings, and without parameterization of the convective and precipitation physics. These simulations were designed to determine the extent to which the surge evolution and GCLLJ structure are “phase-locked” with the convective diurnal cycle along the GoC. To address the challenge of reproducing realistic organized convective activity, this part of the research employed a simple technique to represent MCS effects. The approach involved directly prescribing convective outflows in the model simulations at different times and over regions where MCSs are climatologically observed. These convective outflows were forced in the simulation by prescribing “cold pool” temperature perturbations. Use of this procedure helped elucidate the physical processes responsible for the moisture transport variability from the diurnal to day-to-day timescales. None of the previous numerical simulation studies mentioned in Chapter 1 examined individual surge initiation mechanisms associated with different synoptic environments, or the relative contributions that convective outflows make to the low-level GoC flow.

5.1 Model Description and Experiment Design

5.1.1 Model overview

The ARW (currently in version 3) is a mesoscale model developed by a large number of individuals at different research centers (Skamarock et al., 2005). The ARW dynamic core is a fully compressible, three-dimensional non-hydrostatic (with option of run-time hydrostatic) model with governing equations written in flux form. The general model configuration is set to contain 48 terrain-following vertical levels distributed log-linearly, and keeps at least 25 vertical levels below 700 hPa over the ocean. The finer resolution at lower levels is intended to better represent surface layer and PBL processes which, in the present case, are expected to account for possible nonlinear effects in the propagation of surges (Zehnder, 2004). The model's default time and space integration are performed in the Arakawa-C grid, which uses a third-order Runge-Kutta (RK) time-integration scheme and a fifth order RK advection scheme, respectively. These integration schemes are expected to provide realistic treatment and less smoothing of the moisture surges' leading edges and convective outflows. Although the ARW model hitherto has not been used for modeling GoC moisture surges, it has been applied in a variety of dynamical situations that are consistent with moisture surge processes, including convective outflows (Knopfmeier et al., 2006), MCSs (Done et al., 2003), and convectively-induced disturbances (Koch et al., 2005).

5.1.2 Numerical simulation tests

Different experiments (Table 5) were performed to quantify the impact of the model physical parameterizations on reproducing the moisture surges under large-scale forced conditions. The experiments involved turning on and off different physical schemes in the model. These experiments included: (i) idealized simulations retaining only dynamics and excluding all physical schemes, which assesses whether downscaling the initial and boundary conditions alone could support the surge; (ii) including all physical schemes related to boundary-layer processes, to better represent the stable layer observed over the GoC during the associated disturbance produced by surges (as shown in Chapter 3); and (iii) the same as in (ii) but including cloud microphysics and precipitation representations to better simulate convective processes, which are expected to improve treatment of the possible effects of convective outflows and gravity currents. Since model runs with convective processes are carried out only for grid spacing less than 10 km and the moist convection is expected to be strongly forced, cumulus parameterization schemes are not included in (iii). Simulations were performed using NCEP final analyses (FNL; 1 degree resolution; every 6 hours) as initial and boundary conditions. Simulations were integrated over 120 (96) hours for runs initialized on July 11 (12), with lateral boundary conditions updated every 3 hours. These model tests were systematically evaluated and compared against the NARR and NAME observations.

Table 5. ARW model configurations employed in the different experiments.

Experiment	Initial/Boundary Conditions	Physical Schemes	Special settings	Resolution
i) No Physics	FNL	No surface layer (SL), no land surface model (LSM), no planetary boundary-layer (PBL), no shortwave (SW) and longwave (LW) radiation, no microphysics and precipitation, no cumulus.	Hydrostatic	20, 10, 5 km horizontal grid spacing; 48 vertical levels
ii) PBL+LSM	FNL	PBL: nonlocal turbulent mixing coefficient Yonsei University (YSU, Hong et al., 2006) LSM: Thermal diffusion SL: Monin-Obukhov: Including the RRTM (LW) and Dudhia (SW) radiation schemes every 5 minutes.	Non-hydrostatic	5 km horizontal grid; 48 vertical levels
iii) PBL+LSM+C (full physics)	FNL	Same as ii) but including cloud microphysics and precipitation schemes: C1: Kessler C2: Lin et al.	Non-hydrostatic	5 km horizontal grid; 48 vertical levels

5.1.3 Cold bubble experiments

The most straightforward way to evaluate the effects of convective environments on the low-level flow over the GoC was by directly prescribing convective outflows in the ARW model simulations. Therefore, convective outflows were forced in the simulations through initial state temperature perturbations (cold bubbles, CBs) following Straka et al. (1993) and Janjic et al. (2001). The CBs consisted of a temperature perturbation ($T^{'}$) of the form

$$T^{'}(x,y,z,t) = \Delta T(t)\cos^2\left[\frac{\pi}{2}\sqrt{\left(\frac{x-x_c}{x_r}\right)^2+\left(\frac{y-y_c}{y_r}\right)^2+\left(\frac{z-z_c}{z_r}\right)^2}\right], \quad (5.1)$$

which was applied only where

$$\sqrt{\left(\frac{x-x_c}{x_r}\right)^2+\left(\frac{y-y_c}{y_r}\right)^2+\left(\frac{z-z_c}{z_r}\right)^2}\leq 1. \qquad (5.2)$$

The parameters x_c ,y_c and z_c in (4) and (5) determine the location where the bubble's center was applied, and $x_r = y_r = 150\ km$, and $z_r = 1000\ m$ are the radii from the bubble's center, which determine the size of the CB. The location and size of the CB were assumed to be constant (i.e. the CB was not advected or deformed by the background flow) during each simulation run. The intensity of the bubble is defined by

$$\Delta T(t)=\begin{cases} 7°K, & t=t_i \\ \Delta t\times 3°K/hr, & t_i<t\leq t_f \end{cases} \qquad (5.3)$$

with $\Delta T(t_i<t\leq t_f)$ being used to keep the CB cool during the simulation, and t_i and t_f defining the time when the CB was activated and deactivated, respectively, where t_f-t_i was assumed to be 5 hours. Figure 49 shows an example of the temperature and sea-level pressure evolution induced by inserting a CB over the GoC entrance. While the CB is active, the density and geopotential are hydrostatically adjusted in order to preserve mass in the column where it is located. For $t > t_f$, the CB is turned off and the mass and wind fields are relaxed accordingly (i.e. via a geostrophic adjustment) towards the environmental conditions. This relaxation in the lower atmosphere occurs rapidly and creates a rather large increase in temperature that seems to resemble what has been termed "heat burst." Although heat bursts sometimes are associated with decaying areas of convective precipitation (Johnson et al., 1989; Knievel and Johnson, 1998), in these experiments they are essentially compressing downbursts that heat the surface when the CB cooling function is turn off.

In the CB experiments, ΔT is applied using the same parameters regardless of the time of the day when the CB is forced. By doing so, we are assuming that the intensity of convection is the same throughout the day and independent of the synoptic background forcings. Furthermore, the upscale effect that convective processes (here mimicked by the CB) may have on the background fields are considered negligible. For example, MCSs in the region may work to increase mid-level cyclonic vorticity (Farfan and Zenhder, 1994). Furthermore, by turning off convective processes we are simplifying radiative processes with potential impact on the surface and planetary boundary layers. We are aware of the complex dynamics of the MCSs but at this point, these simplifications were necessary and important.

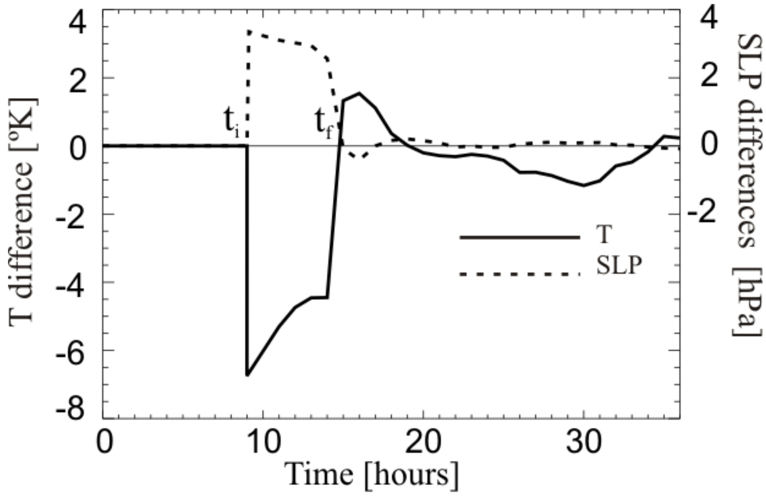

Figure 49. Surface temperature (T) and sea level pressure (SLP) differences evaluated at the bubble centroid (x_c ,y_c, *10m*) when comparing a CB simulation run (starting at tf= 09 hours, lasting for 5 hours) minus its control simulation run (no CB simulation run).

In summary, the CB approach employed isolates the representation of convection in the ARW by directly emulating the convective outflows to help determine their cumulative effect on the GoC low-level flow. However, we performed the numerical simulations with realistic background conditions, such as for the strong synoptically-forced event (associated with TS Blas) (hereafter called "surge") of July 12-15, 2004, and for a weak synoptically-forced event (hereafter called "non-surge") for which we selected the period of July 18-21, 2004. Although these surge and non-surge events do not necessarily represent the extremes of the possible synoptic conditions, their synoptic forcings (or the lack of them) are well-described from enhanced observations obtained during NAME. Note that the surge case was thoroughly analyzed in Chapter 3 of this research. For the selection of the non-surge case, we reviewed Yuma surface station and upper-air observations for a set of days with relatively weak southeasterly low-level wind conditions.

The model configuration used in this part of the research corresponded to experiment (ii) in Table 5. Some minor effects were investigated by changing the horizontal resolution between 2.5, 5, and 10km. Although a higher horizontal resolution often is desirable for regions with complex terrain, we chose to work with a 5 km horizontal resolution due to limitations in computational resources. As noted in Table 5, this model configuration does not include either convective or cloud microphysics and precipitation schemes to simulate the effect of convective processes. Instead, the effects of convective activity on the low-level flow were represented by inserting CBs at different places over the GoC region. In these experiments, all runs were initialized at the same time for each synoptic background condition, July 12 00Z for the surge event and July 18 00Z for the non-surge event. In each run, the cold bubble was inserted at a different t_i (with t_i varying every 3 hours), starting at time +3:00 hours until +48:00 hours in the simulation run. The CBs also were inserted separately at two different sites within the NAMS core region: a first set of simulations with the CBs located to the south of the GoC entrance (GE) centered over [22.3°N, 107.2°W]; and a second set with the CBs located over the GoC coastal plain (CP) centered over [29.2°N, 110.2°W]. Thus, a set of 17 WRF runs was performed for each synoptic condition and for each site. A summary of the experiments is presented in Table 6. Results are limited to hourly data extracted from the simulations, which then are compared against the Control Run.

Table 6. Summary of CB experiments conducted using model configuration (ii) in Table 5. Simulations were run for 72 hours. The cold bubbles are forced at two different sites: either over the GoC entrance (GE) or over the GoC coastal plain (CP). There is a simulation run for every t_i={03,06, 09, 12,…, 48 hours}, for every synoptic condition and each of the two sites where the cold bubble is inserted. A total of 17 simulation runs are performed.

Synoptic forcing	**TC/TS Surge-related**; *starting on July 12, 2004, at 00UTC*		**Non-surge related**; *starting on July 18, 2004, at 00UTC*	
Location of CB	GE	CP	GE	CP
Control run	1		1	
Number of runs with CB	16	16	16	16

Other, more sophisticated approaches for producing a controlled convective outflow were considered in this research, such as activating the triggering function in the convective parameterization schemes. However, these relied on triggering function formulations requiring the control of moisture convergence, convective available potential energy, and other measures of convective instability, which were difficult to implement and repeatedly produced numerical instabilities in the modeling system. In addition, this alternative approach did not guarantee the simulation of realistic long-lasting MCSs. For practical purposes, we used the CB approach since is it easy to implement and has produced realistic gravity currents (Straka et al., 1993; Janjic et al., 2001).

5.2 Numerical simulation of the July 12-15 surge

In this section, the performance of the ARW model simulations for the different experiments shown in Table 5 are evaluated for the NAME surge event of July 12-15, 2004. Figure 50 shows the evolution of the simulated along-GoC vertically integrated (1000-850 hPa) moisture flux for different NAME RAOBS sites located along the eastern GoC coastal plain shown in Figure 5 (Puerto Peñasco (ISS2), Kino Bay (ISS3), Guaymas (MGYM), and Los Mochis (ISS4)). When compared with the observations, all simulations in Figure 50 capture the overall surge-like structure, which consists of an increase of the southerly moisture flux between June 12 and 15. However, systematic deficiencies are observed with respect to the inclusion (or not) of physical parameterizations in the simulations. The "no-physics" runs produced earlier and more sudden surge-like conditions, featuring problematic behavior of the surge onset (Figure 50) without an evident northward progression from the southern GoC (ISS4) to the northern GoC (ISS2). Although the reasons for this behavior are unknown at this time, it is speculated that this likely is due to the lack of a well-defined stably stratified PBL over the GoC, and the missing diffusion and mixing processes from the PBL physical schemes. For display purposes, only simulations using horizontal resolutions of 20 and 5 km are shown. However, changing the horizontal resolution (20, 10, 5, 2km) of the "no-physics" simulation did not produce significant differences in surge onset simulations.

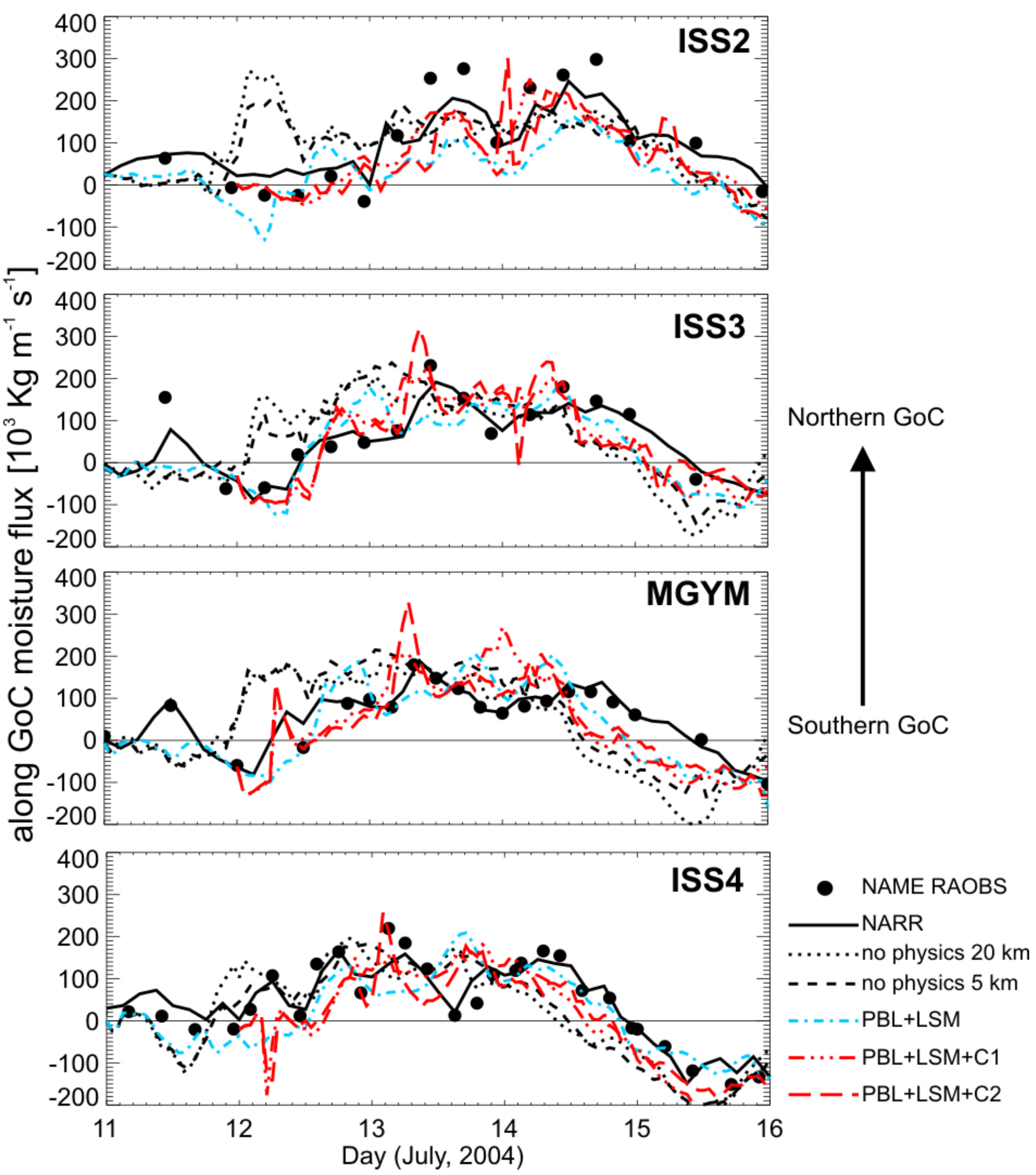

Figure 50. July 11-16, 2005, evolution of along-GoC vertically integrated (1000-850 hPa) moisture flux for different NAME RAOBS sites (solid dots) located along the eastern GoC coastal plain (from top to bottom, Puerto Peñasco (ISS2), Kino Bay (ISS3), Guaymas (MGYM), and Los Mochis (ISS4), see location in Figure 5). Different simulation experiments shown in Table 5 (see legend) are compared with NARR (solid line).

The simulations performed using the PBL+LSM and PBL+LSM+C (full physics) experiments are in closer agreement with observations (Figure 50). Both microphysics schemes capture better the surge's initial state (after July 12 00 UTC) and the overall surge evolution, although they still are somewhat inconsistent concerning day-to-day and diurnal variability. For example, the late night and early morning moisture maxima, presumably associated with the enhanced GCLLJ (Section 3.5), are poorly captured by the model simulations. The simulation results show better agreement at Los Mochis and Guaymas (southern half of GoC) than at Kino Bay and Puerto Peñasco (northern half of GoC). The NARR data seem to represent better this surge event when compared with the NAME observations, yet underestimate the strong early morning moisture flux observed over the northern Gulf (ISS2, Figure 50) on July 12 and 13.

Figure 51 shows different organized convection events with their associated convective outflows that appear well-defined and realistic. In the majority of cases MCS-like structures dominate the simulated rainfall field. In general, changes of convective treatment by altering microphysical schemes have relatively large impact on the moisture flux field. These outflows occurred both (i) during the surge onset (July 12 14UTC) to the south of the Gulf entrance, (ii) over the SMO western foothills after the surge passage across the central Gulf coastal plains (July 13 05UTC), and (iii) later over the northern GoC (July 14 01UTC). Sharp moisture flux peaks in the full physics simulation (Figure 50) are associated with these outflows, with timescales of 3-6 hours. Although ARW 5 km simulations with full physics seem to resolve adequately many storm-scale features that typically are associated with upslope forcing due to the diurnal cycle of the low-level flow, the intensity and duration of the convective outflows are sensitive to changes in the microphysics and precipitation schemes (Figure 51).

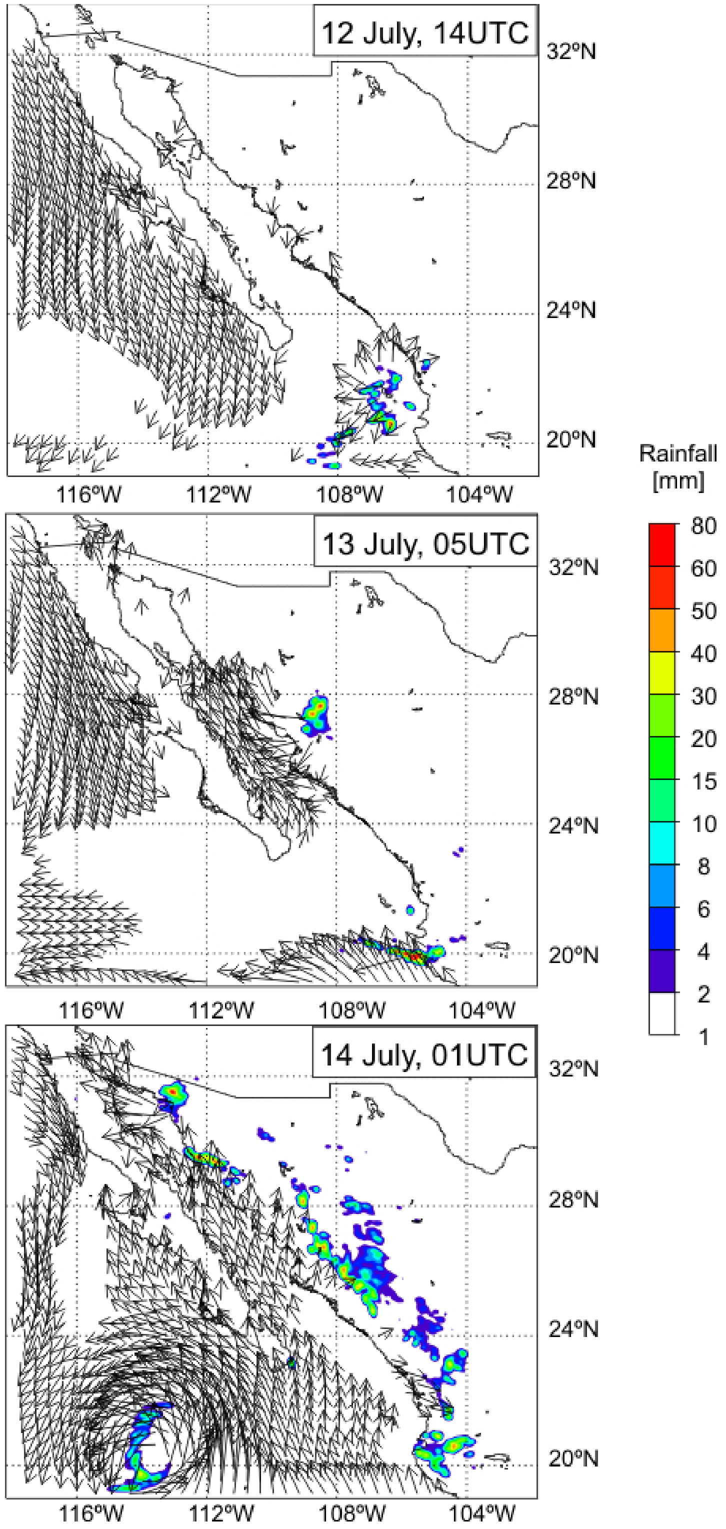

Figure 51. Wind vectors at 950 hPa and rainfall fields [mm hr^{-1}] using ARW full physics simulation (PBL+LSM+C2, see Table 5) for July 12-14, 2005. Only wind vectors with magnitude greater than 5 m s^{-1} are displayed.

Figure 52 compares a full physics simulation (PBL+LSM+C2) with WP-3D aircraft observations the along-Gulf moisture flux across the far northern Gulf for July 13 at 17UTC (transect A-B over the far northern GoC, Figure 18b). Both the observed and simulated moisture fluxes are stronger over the GoC than over the coastal plain. However, the simulated moisture flux magnitude underestimates the observed maximum value by 45%. This strong low-level southerly moisture flux, associated with the northern GCLLJ, currently is the focus of debate and its dynamical characteristics are still are unclear (e.g., Douglas et al., 1998; Fawcett et al., 2002). Previous model simulations (see Chapter 1) tended to locate the jet farther to the east, over the western foothills of the SMO. This discrepancy highlights the importance of the offshore observations obtained with the WP-3D aircraft. Furthermore, the full physics simulations show the difficulty of reproducing the mesoscale moisture field revealed in Chapter 3, even for strong synoptically-forced events.

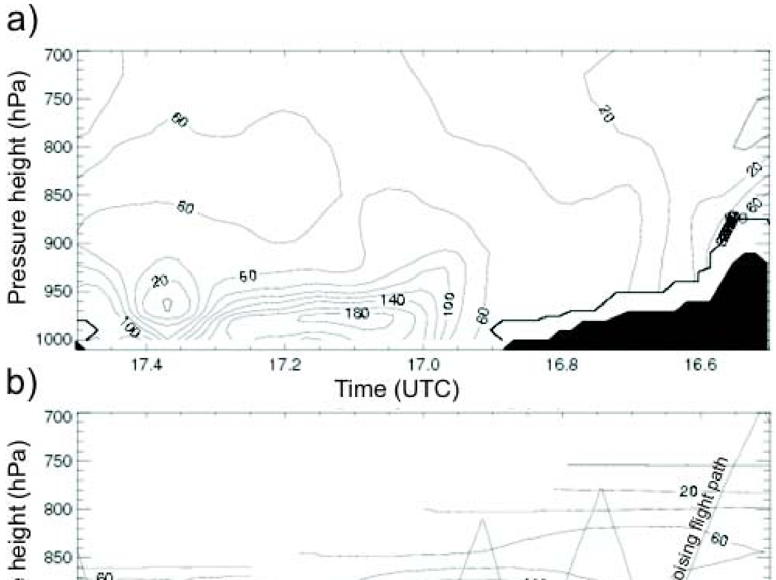

Figure 52. Vertical cross-GoC section (flight leg A-B in Figure 18b) of the along-GoC moisture flux component (g kg^{-1} m s^{-1}) for July 13 at 17 UTC using a) ARW model output with full physics (PBL+LSM+C2) and b) interpolated WP-3D aircraft observations. Porpoising flight path also is shown in b). Shaded regions represent the terrain.

A comprehensive assessment of the mesoscale features simulated during this surge case requires a separate research effort and exceeds the exploratory scope of this chapter. Although regional/mesoscale models have well-recognized limitations in reproducing MCSs (Chapter 1), such MCSs clearly affect the magnitude and timing of the flow transients within the NAMS core region (Sections 4.5 and 4.7). Therefore, in the remaining sections of this chapter, we restrict the investigation to the sensitivity of the NAMS core domain low-level flow to mesoscale temperature and pressure transients.

5.3 Effect of convective outflows during surge lifetime

This section describes the sensitivity of surges to convective activity using the ARW model and the experimental procedure described in Section 5.1.3.

5.3.1 Control runs

Surge event (Associated with TS Blas)

We first introduce the control run for the surge event, which consists of a 72 hour simulation running from July 12 00UTC to July 15 00UTC, without imposing a CB. The evolution of the simulated low-level (950 hPa) along-GoC wind and potential temperature extracted along the GoC SE-NW axis are shown in Figure 53a-b, respectively. Note that along the GoC there are enhanced low-level winds and relatively cold temperatures that are associated with the surge signal. In the northern half of the GoC the flow is predominately northwesterly right before and after the surge passage. Other details of this surge case and its relationship with TS Blass were described using observations (Section 4) and the corresponding simulation results were shown in Section 5.2.

The control run provided the background to assess whether there is a significant effect on the low-level flow when the CBs are applied at different times during the surge's evolution (Section 5.1.3). The difference between each simulation and the control run provides a way to evaluate the overall impact that the CBs have on the GoC low-level flow.

Non-surge event

Figure 54 shows the simulated non-surge control run (72 hours run from July 18 00UTC to 21 00UTC) low-level (950 hPa) along-GoC wind and potential temperature along the GoC SE-NW transect. In contrast with the surge event simulations (Figure 53), the southeasterly wind flow is much weaker with subsequent regions of persistent weak northwesterly flow that extend over almost the entire GoC.

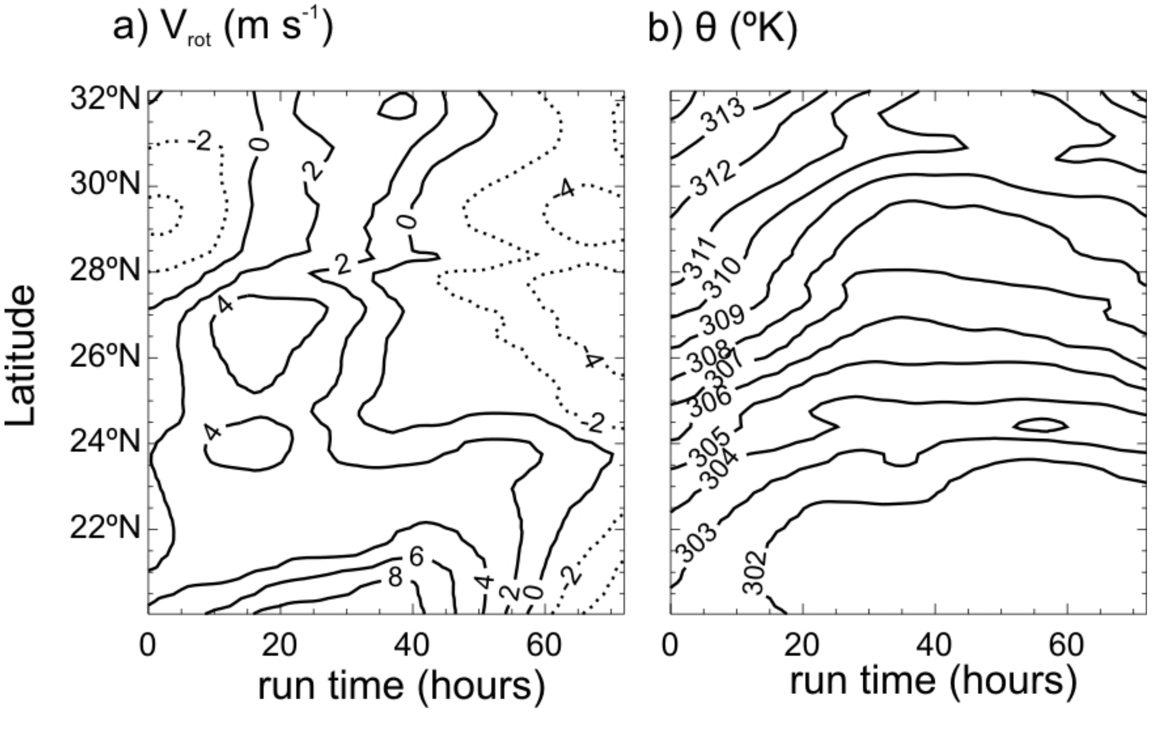

Figure 53. Evolution of along-GoC cross section (latitude) of the surge event at 950 hPa for the a) along-GoC wind component (m s^{-1}) and b) potential temperature (°K). In a) solid (dashed) contours indicate positive (negative) quantities.

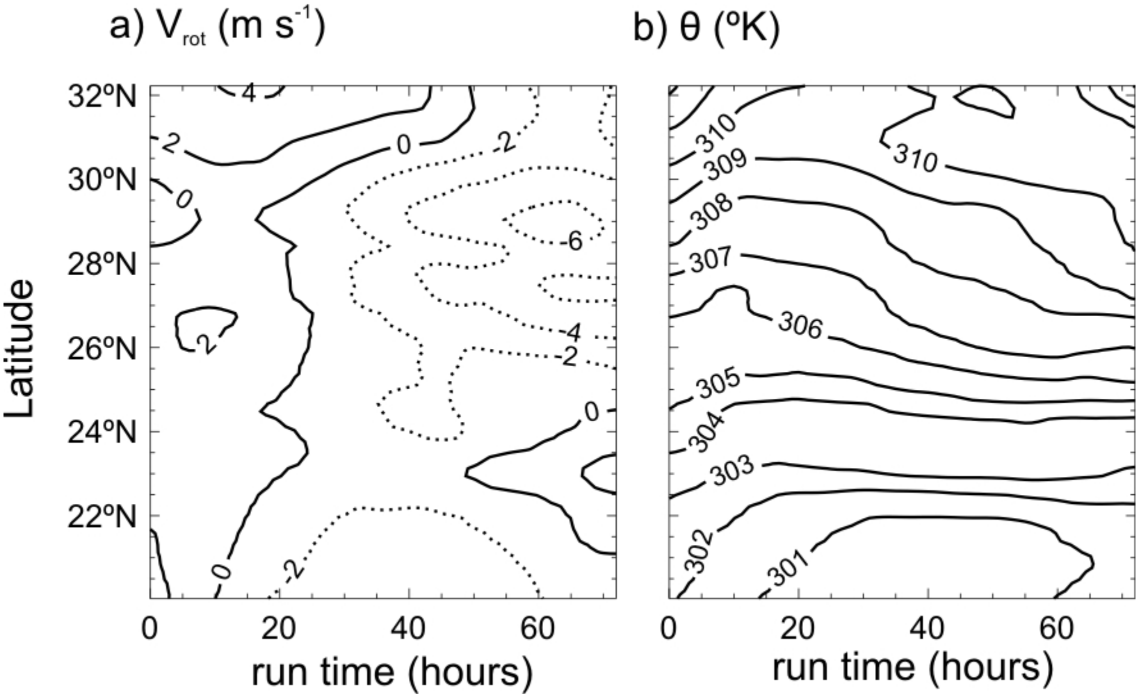

Figure 54. Same as Figure 53 but for the non-surge event.

5.3.2 CBs over the GoC entrance (GE) and over the coastal plain (CP)

For illustrative purposes, Figure 55 and 56 show an example of numerical simulations when a CB is inserted over the GE region on July 12 0900UTC. Figure 55 shows the 950 hPa wind and potential temperature fields, while Figure 56 shows the vertical cross sections along the GoC NW-SW axis. Note that the CB stands out from the background flow. The CB cooling produces a mesohigh pressure response (as illustrated earlier in Figure 49). This feature then produces a strongly diffluent wind field that is superimposed on the background wind field. This feature resembles an outflow boundary with propagation characteristics of a gravity current. This pattern persists for 5 hours while the cooling function is active.

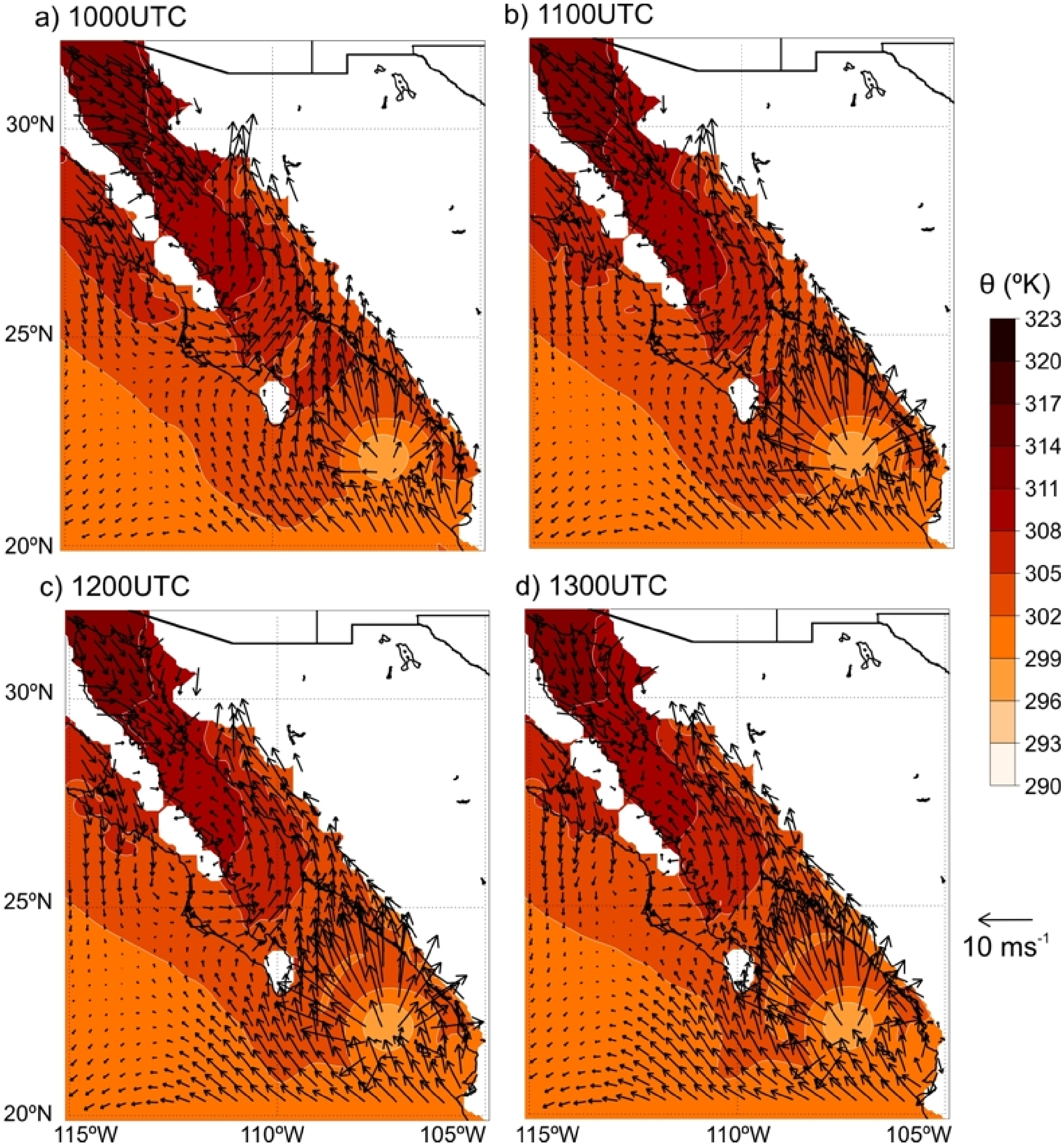

Figure 55. Simulated 950 hPa surge event potential temperature (°K, shaded) and wind vectors (ms^{-1}, arrows) on July 12 at a) 1000, b) 1100, c) 1200, and d) 1300 UTC, after inserting the CB over the GoC entrance (GE) (22.3°N, 107.2°W). Wind vectors are plotted only for every eighth grid point to ensure clarity. White areas indicate where 950 hPa surface intercepts the terrain.

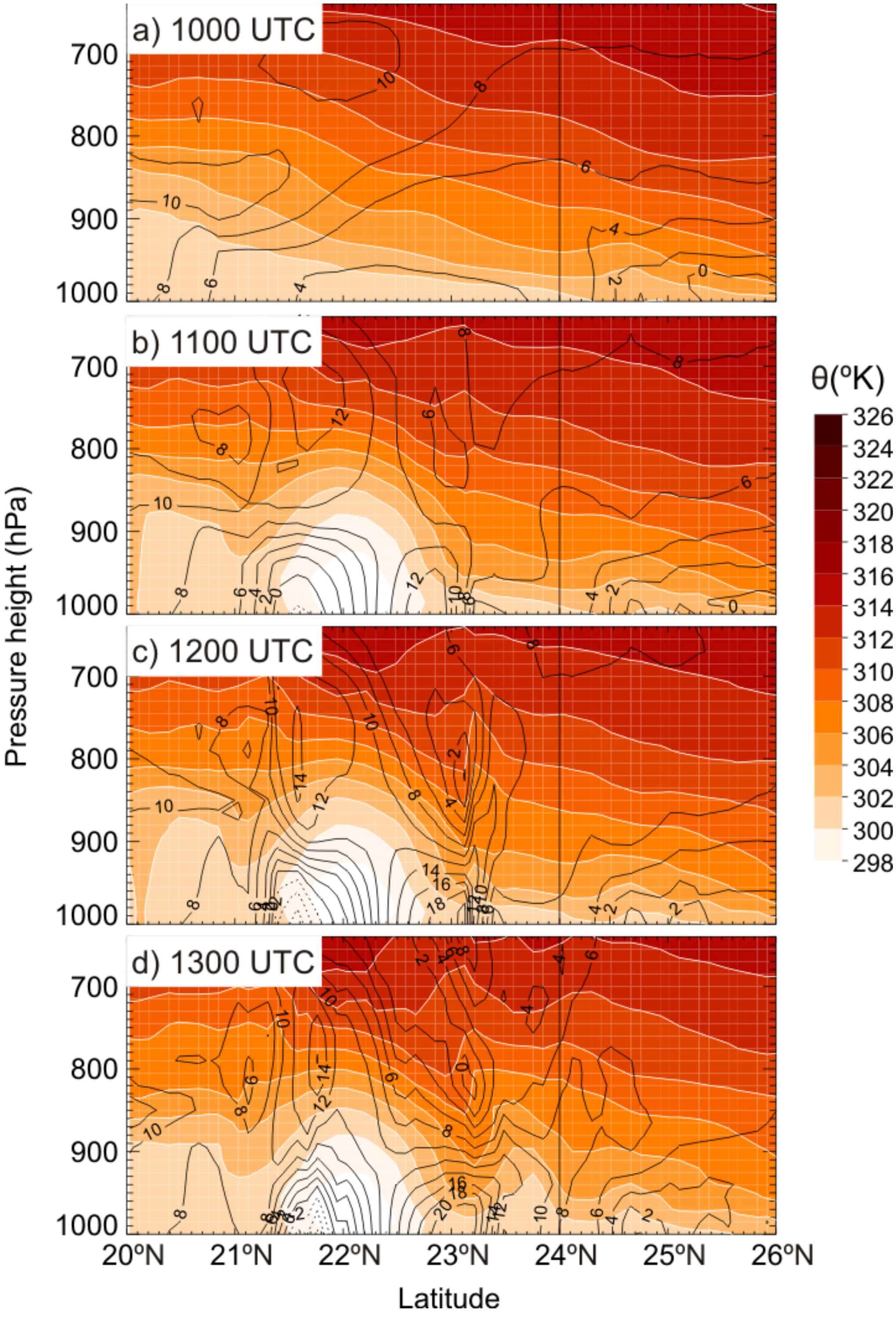

Figure 56. Simulated surge event along-GoC vertical cross sections of potential temperature (°K, shaded with white contours) and along-GoC wind component (m s^{-1}, black contours): a) right before the CB is inserted on July 12 1000UTC, and b-d) subsequently at 1100, 1200 and 1300UTC, respectively.

Figure 57 shows numerical simulation results after inserting the CB on July 12 1000UTC over the GoC coastal plain. The effect of the CB on the flow over this region is identical to that described for the GE case. In general, we argue that the model grid size (5 km), as well as the physical parameterizations implemented, appear to be sufficient to represent realistic gravity currents as commonly observed (Simpson, 1987). The use of higher horizontal and vertical resolution in the simulation runs (not shown) does not have distinguishable effects on the propagation and intensity of the surge and the propagation and intensity of the gravity currents induced by the CBs.

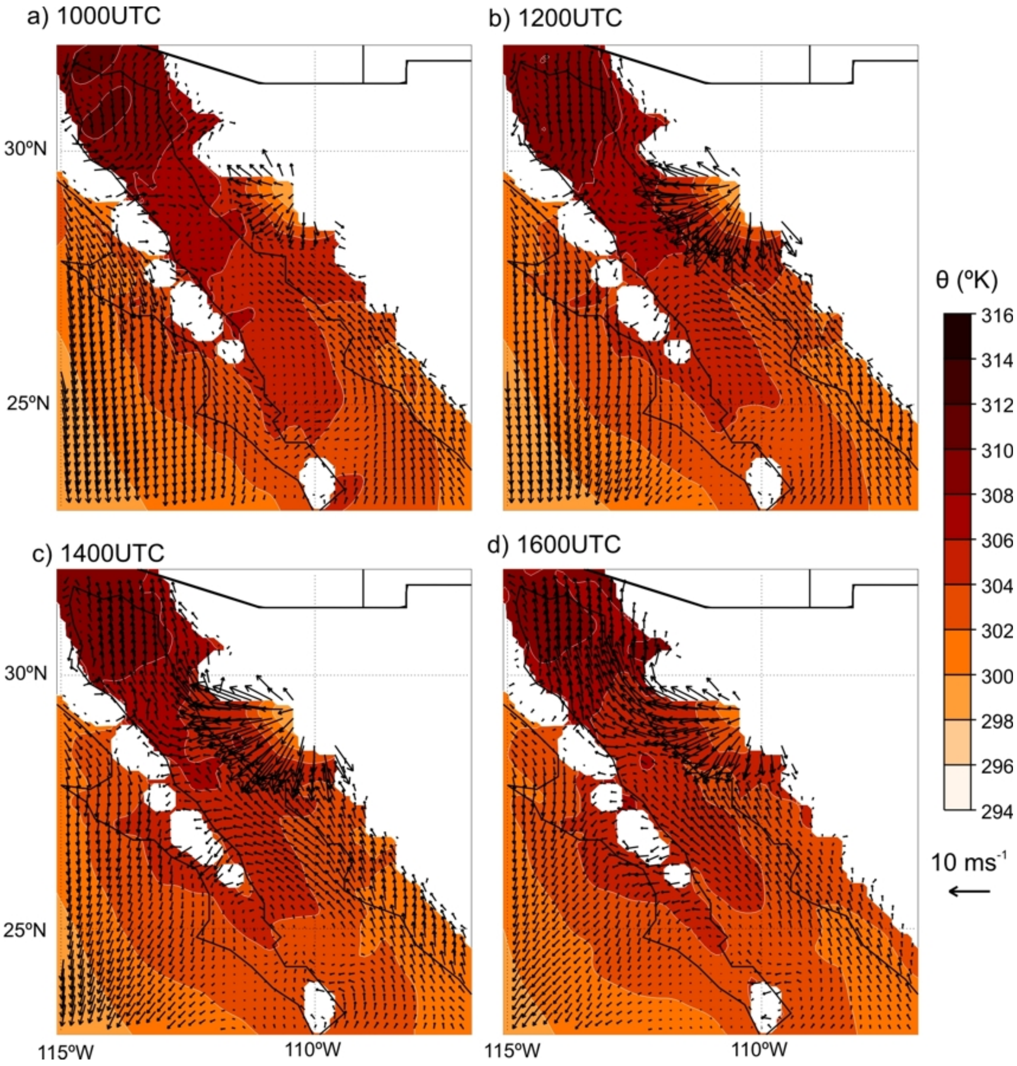

Figure 57. Simulted 950 hPa potential temperature and wind vector on July 12 a) 1000, b) 1200, c) 1400, and d) 1600 UTC after inserting the bubble over the GoC coastal plains (CP) (29.2°N, 110.2°W). Wind vectors are plotted only for every eighth grid point to ensure clarity. White areas indicate where 950 hPa surface intercepts the terrain.

5.3.3 Impact of CBs over the GoC

CBs over the GoC entrance (GE)

Figures 59 and 60 show the modeled evolution of the low-level (950 hPa) along-GoC wind speed and potential temperature anomalies for CB runs over the GE area for the surge and no-surge cases, respectively. Anomalies are calculated as differences between each of the runs when CBs are initiated at different t_i minus the control run. Note that the surge and non-surge modeled quantities are identical to their control runs before the CBs are initiated. Not surprisingly, significant differences in the low-level wind and temperature fields show that the CBs directly influence the surrounding region where they are applied when compared against the control run (Figures 59b and 60b). Specifically, enhanced flow with timescale fluctuations similar to those of the CBs (~5-8 hours) are observed just to the northwest of the CB disturbances, which applies for both surge and non-surge cases. Also noteworthy is the local reversal in the wind anomalies (shifting from southeasterly to northwesterly) observed several hours after the CBs are turned off. As mentioned earlier (Section 5.1.3), this is a feature of the CB relaxation, which is induced by diabatic heating produced when the CBs collapse.

Figures 58a and 59a indicate that the difference in wind and potential temperature propagate up-GoC with an average speed of 15 m s^{-1} (speed estimated by tracing leading edge of wind front). In the mid-GoC, the direct effect of this enhanced southeasterly flow rapidly disappears. These results agree with Zehnder's (2004) scaling analysis in terms of lifespan and extent of gravity currents as moisture surges precursors. On the other hand, the simulated differences indicate that the effects of CBs over the southern GoC appear to be related to diurnal processes. Over the southern half of the GoC, wind differences are larger during late afternoon and nighttime hours (associated with CBs initiated during the daytime) with the smallest impact during the daytime.

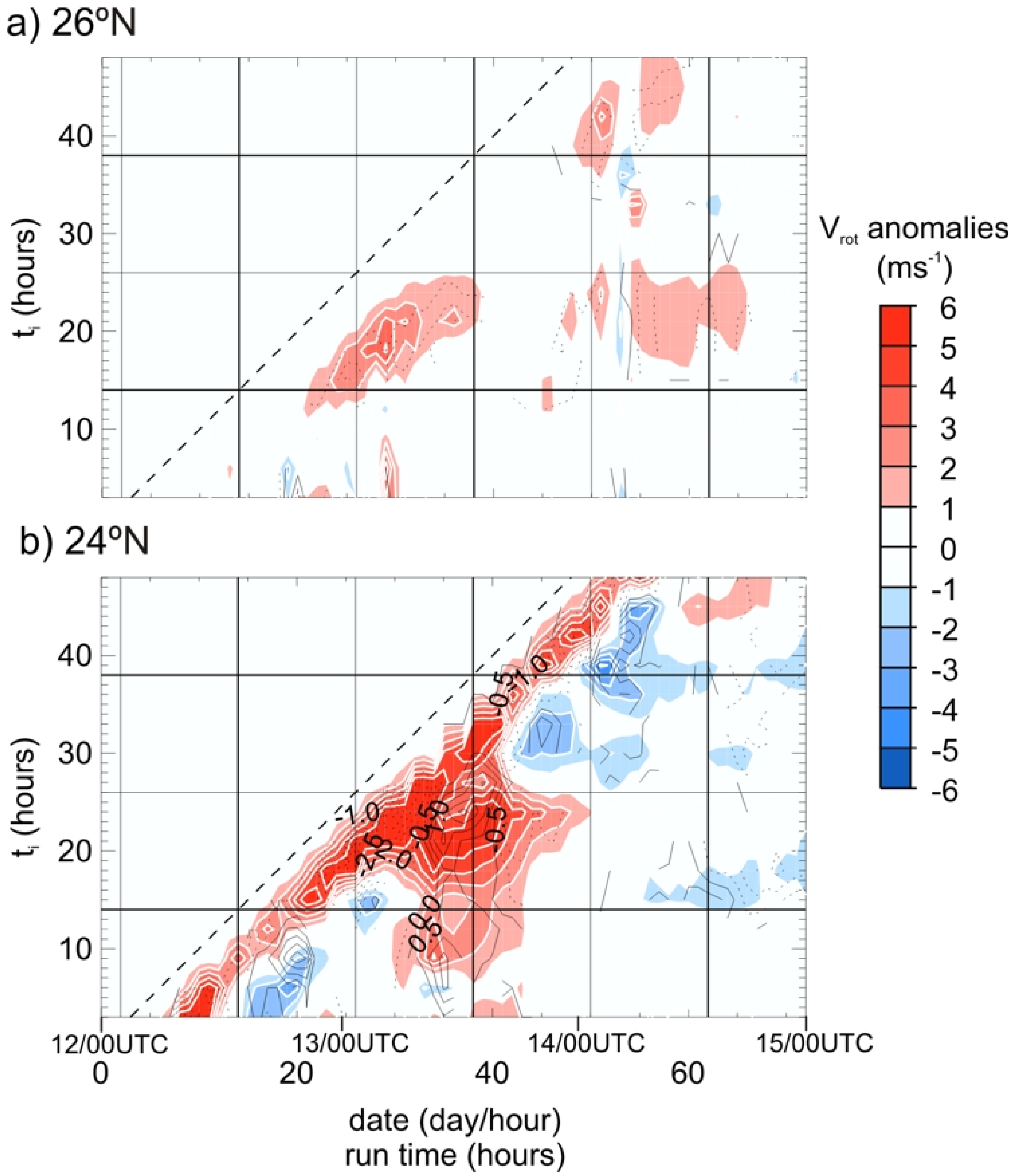

Figure 58. Simulated surge case (July 12-15, 2004) evolution as a function of time t_i (varying i from 3 to 48 hours, every 3 hours). Contours give the 950 hPa along-GoC wind speed (ms^{-1}) (filled contours) and potential temperature (°K) (unfilled contours) differences between CBs initiated over the GE area minus its control run. a) and b) show the evolution points over the center of the GoC intercepting latitudes 26°N and 24°N, respectively. 45° dashed line shows the time when CBs are initiated with respect to the run time. Solid dark (thin) grid indicates the sunrise (sunset) times for this region.

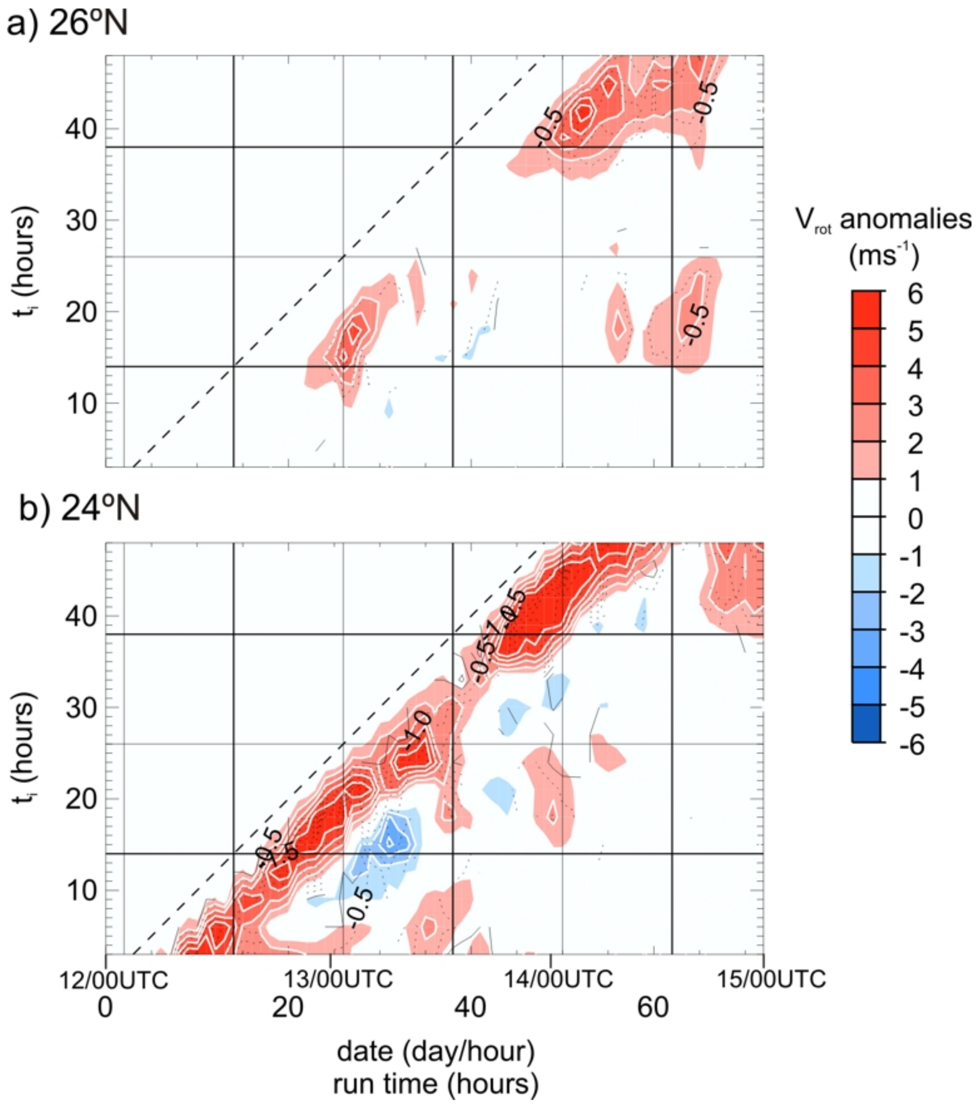

Figure 59. Same as Figure 58 but for the simulated non-surge case.

In the surge case (Figure 58b), there also is a long lasting (~ 20-24 hours) feature indirectly related to disturbances induced by the CBs. This consists of enhanced southeasterly moist flow starting in the early morning of July 13, with a timescale (> 5 hours) longer that those from the forcing. In contrast, the non-surge case (Figure 59) does not show any sign of an indirect effect induced by the CBs when compared with the control run, which suggests a possible role of the surge and CB in favoring stronger than normal southeasterly flow along the GoC. Apparently, CBs create conditions that enhance the effect of the surge signal (Figure 53). Thus, CBs appear to affect the development and intensity of surges over the region, which is consistent with the results presented in Chapter 4 based on multi-year data sets and surge events.

CBs over the GoC coastal plain (CP)

Figures 60 and 61 show counterpart results to those as in Figure 58 and 59, when the CBs are applied over the CP region. Since CBs are centered over 29.2°N/110.2°W, thus, Figure 60a and b are constructed for points located to the north of the CBs. The most striking feature in these experiments is the significant up-Gulf anomaly flow over the northern half of the GoC induced by the CBs. However, the intensity of the anomalous up-GoC flow shows strong variations in phase with the diurnal cycle. CBs initiated early in the morning produce a stronger southeasterly flow than those initiated during the late afternoon and evening hours.

There are significant differences between the effect of the CBs for surge and non-surge related cases. During surge related events, the southern (not shown) and central GoC (Figure 60c) are unaffected by the CBs, while during non-surge related cases (Figure 61) there are down-GoC wind and temperature disturbances. In the northern GoC, however, there are better-organized anomalous structures for the non-surge case (Figure 61) than for the surge case (Figure 60). During the nighttime and early morning hours, several of these long-lasting disturbances show enhanced southeasterly flow for over 15 hours. Although these features partly are produced by the direct impact of the CB boundary flows, the long lasting features over the northern GoC (during the night and early morning) appear to be indirectly induced. One can speculate that local interaction of the outflows with the topography and diurnal processes work favorably to enhanced up-GoC low-level flow. These results are consistent with the evidence presented earlier for minor surges using a composite climatology analysis (Section 4.5), and resemble the conceptual model presented in Figure 39.

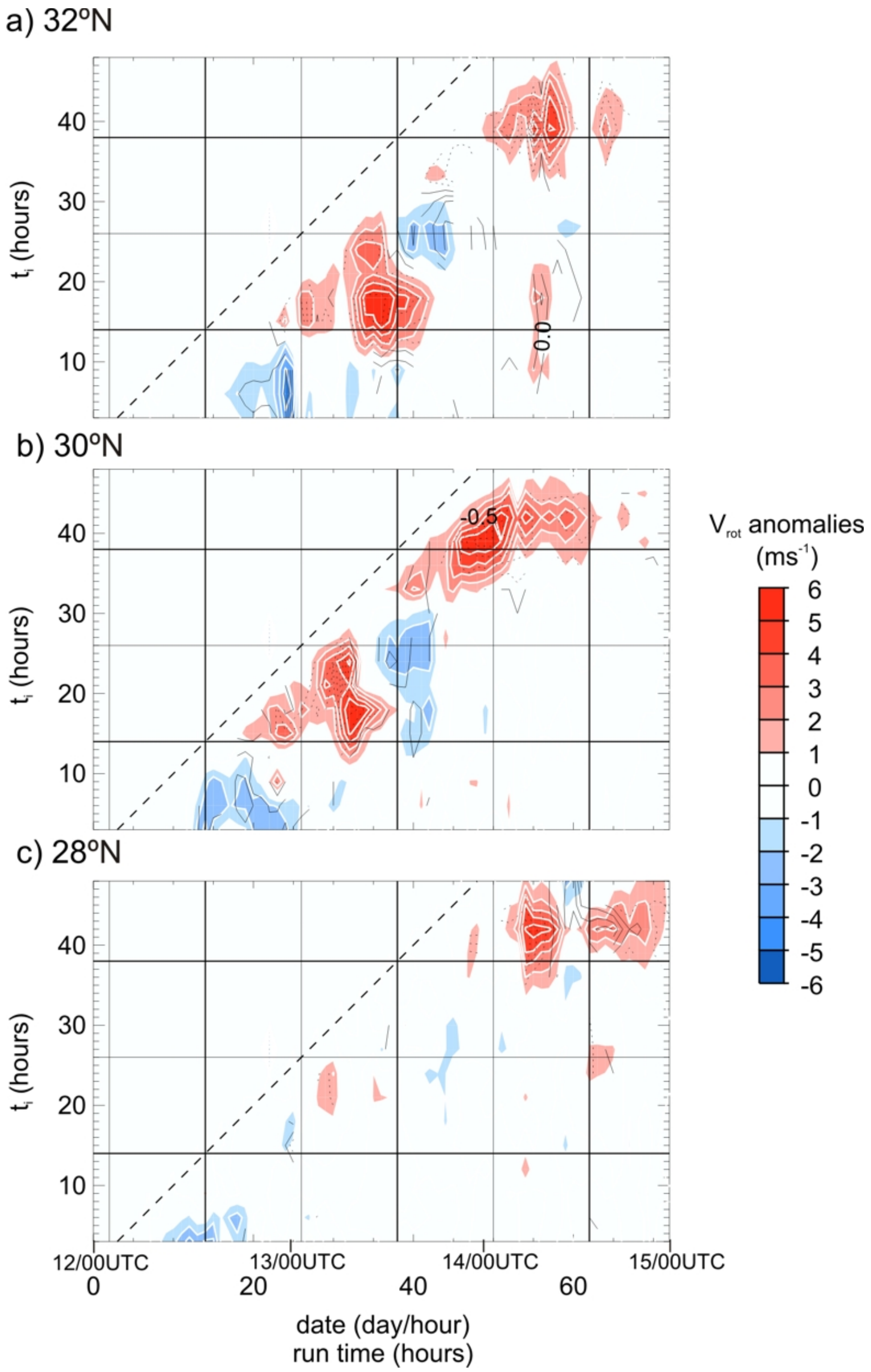

Figure 60. Simulated surge case evolution (hourly) as a function of time t_i (varying i from 3 to 48 hours, every 3 hours). Contours give the 950 hPa along-GoC wind speed (ms^{-1}) (filled contours) and potential temperature (°K) (unfilled contours) differences between CBs initiated over the CP area minus its control run. a), b), and c) show the evolution for points over the center of the GoC intercepting latitudes 32°N, 30°N, and 28°N, respectively. 45° dashed line shows the time when CBs are initiated with respect to the run time. Solid dark (thin) grid indicates the sunrise (sunset) times for this region.

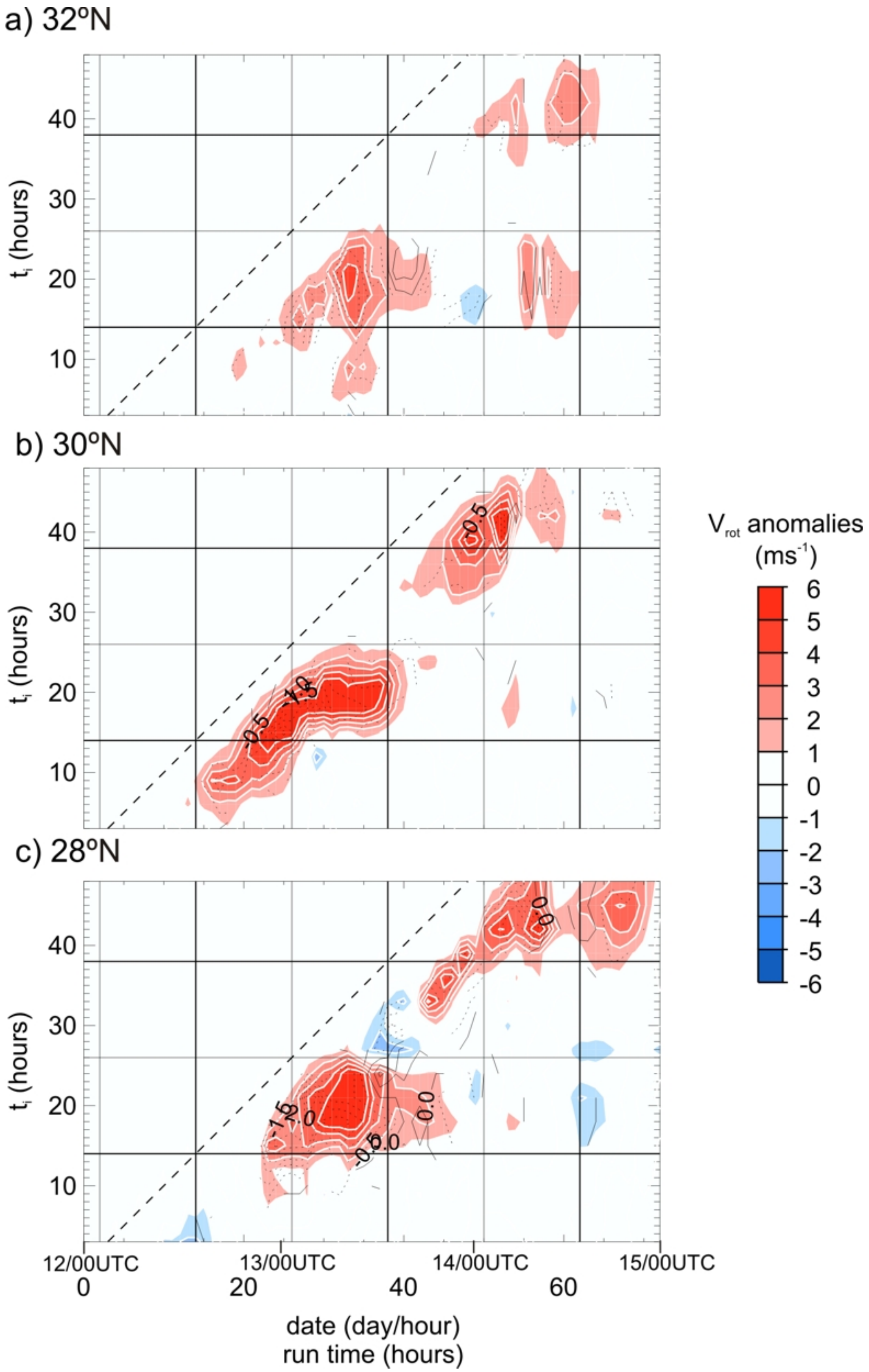

Figure 61. Same as Figure 60 but for the non-surge case.

5.4 Concluding Remarks

This chapter sought to determine the effect of simulated mesoscale processes on different synoptic-scale background flows during moisture surge and non-surge conditions. The main objective was to distinguish the MCS contribution to the GoC low-level variability attributable to MCSs from that associated with the diurnal cycle and the synoptic-scale background flow.

The ARW simulation runs, using FNL data as initial and boundary conditions, captured the main characteristics (timing, intensity, evolution) of a well-observed moisture surge (July 12-15, 2004) during the NAME. In general, the onset and evolution of the surge agreed favorably with NAME and NARR observations. However, model performance was evaluated only over the GoC coastal region. Due to the lack of observations in the mountain regions, a check for consistency was not performed there. Further, the model was sensitive to different microphysics and precipitation schemes in the full physics runs. Runs with multiple ice categories (full physics run using Lin et al. microphysics scheme) produced more realistic results than did simpler non-microphysics runs. Convective outflows in the simulated moisture flux fields have a large impact on the hourly and day-to-day variability of the surges. Random simulated rainfall events, mainly induced by diurnal processes within the GoC region, produced well-defined convective outflows affecting the moisture flux patterns during the surge lifetime.

In the interest of simplicity, this chapter also assessed the sensitivity of the surge intensity to convective activity by replacing the aggregate effect of convective outflows (typically resulting from MCS events) by CBs. The CB approach was a necessary and satisfactory approximation, however, several assumptions were made to replace the effect of actual convective activity by those of the gravity current and associated thermal and pressure perturbations. Based on this new model configuration, we found that the low-level flow within the GoC domain is sensitive to convective outflows.

Results using this model configuration further verified the impact that CBs have on the regional flow during synoptically forced conditions. The effect of CBs over the southern GoC region was sensitive to the time of the day when they were introduced, with stronger responses characterizing CBs initiated during the daytime. Additionally, during surge conditions, the CBs also had an indirect effect by enhancing up-GoC low-level flow at timescales longer than that of the CB forcing. Surges were intensified by i) the convective outflows that were directly associated with mesohigh disturbances at timescales of ~5 hours, and ii) indirectly increasing the offshore pressure gradient associated with TS Blas. This indirect feature had a long lasting (~ a day) impact over the southern GoC region.

This chapter also assessed the influence of simulated CBs over the mid-GoC coastal plain. The influence of CBs in this region was more pronounced for non-surge than surge synoptic conditions. Anomalous southeasterly low-level flow over the northern GoC mainly was associated with CBs inserted during the daytime. Thus, unusually long lasting anomalies associated with these CBs may be due to:

i) weakening of the sea-breeze due to a decreased cross-Gulf temperature contrast;

ii) less momentum extracted from the GoC into the CP associated with the development of a weaker sea-breeze;

iii) a cooler day being followed by a cooler night, which strengthens the cross-GoC temperature gradient (assuming the SSTs over the GoC remain the same); and

iv) an enhanced offshore pressure gradient resulting in enhanced up-GoC geostrophically balanced flow.

Results from these high-resolution numerical simulations show that mesoscale processes, mainly those associated with convective activity, can have a significant impact on the regional flow within the GoC. In particular, GCLLJ variability and intensity were larger when CBs were inserted. Therefore, uncertaintites in the prediction of significant rainfall events, both their timing and duration, can affect the up-GoC moisture transported into the southwestern US.

6 GENERAL CONCLUSIONS

The principal objective of this research was to determine the relative roles of synoptic-scale forcing and mesoscale convective activity in the overall variability of moisture surges along the GoC. This is important because moisture surges represent perhaps the most important source of rainfall variability in the North American Monsoon core region. The research analyzed observations and performed numerical simulations aiming at understanding the importance of MCSs throughout the surges's lifetime. Specifically, the analyses focused on the multiscale connections between major surges events- often associated with synoptic-scale tropical disturbances, and mesoscale convective processes, including their modification by the diurnal cycle.

This research was reported in three separate chapters, each of which pursued the principal objective using different approaches. Chapter 3 was dedicated to a detailed analysis of a well-observed moisture surge that occurred during the North American Monsoon Experiment (NAME-2004). In Chapter 4, multiyear data sets of upper-air and satellite observations and the North American Regional Reanalysis (NARR) products were composited with respect to intraseasonal- and synoptic-timescale circulation patterns affecting the NAM domain, and these were further stratified with respect to mesoscale rainfall variability in the NAM core region. Finally, numerical simulation experiments were performed in Chapter 5 using the Advanced Research Weather Research and Forecasting (ARW V3.0) model. The simulations investigated the sensitivity of the model to physical representations associated with convective processes during surge and non-surge synoptic-scale conditions. The most important conclusions associated with the working hypotheses are summarized and discussed next. This is followed by suggestions for future research that are derived from the present findings.

Chapter 3

One of the key contributions of this research was the comprehensive documentation of the strong surge event observed during the July 12-15, 2004, period of NAME. Previous studies (e.g., Rogers and Johnson, 2007) provided a detailed analysis of the propagation of this surge using NAME high-resolution wind profilers and enhanced upper-air observations. However, the present research was the first to analyze the NAME aircraft measurement and a set of combined radar and upper-air observations obtained during the initial stages of the surge. This analysis identified and described horizontal and vertical structures of the surge over the southern GoC. Results indicated that the kinematics of the surge's leading edge most closely resembled a solitary Kelvin wave.

NAME observations also were analyzed to elucidate the role of organized convective activity (MCSs) during the July 12-15, 2004, surge. For example, an MCS event and an associated gravity current that developed during the early stages of the surge indicatedthe potential for an MCS to either trigger the surge response or superpose the surge signal that could have originated from the interaction of TS Blas with the SMO. Additionally, the use of both surface and upper air observations permitted delineation of the impact of other MCSs that developed during subsequent days over the mid-GoC and its coastal plain. Finally, these analyses provided evidence of how the small-scale wind structures associated with the MCS's density currents can increase the diurnal variability of the surge and the GCLLJ.

Chapter 3 also established the need to determine the importance of MCSs in the overall NAMS core region through description of their diurnal and day-to-day variability in a climatological context. These findings established the focus of Chapter 4, where the role of the MCSs was documented in the context of surges and related synoptic disturbances.

Chapter 4

The research presented here employed multiple data sets in a multiyear compositing framework to identify the importance of convective activity in the development and intensity of GoC moisture surges. Specifically, NARR and QuikSCAT products were used to investigate the response of moisture surges and satellite-identified MCSs to westward propagating synoptic-scale disturbances, such as TSs/TCs and TEWs, and to eastward propagating intraseasonal disturbances, such as MJOs. Previous studies had investigated the relationships between surge occurrence and synoptic-scale atmospheric conditions. In contrast, the present research focused on improving such analyses by incorporating the effects of concurrent mesoscale convective activity in the region. The new results indicates that MCS activity in the lower GoC region is associated with stronger surges, regardless of the synoptic disturbance producing the surge. Another key contribution of this research highlighted the important role of synoptic disturbances (e.g., TEWs) in increasing the likelihood for MCS development within the GoC domain. These results further documented the multiscale processes associated with the NAMS rainfall variability.

Other results presented in Chapter 4 showed that different synoptic conditions, such as those associated with surge and non-surge days, produced diurnal and day-to-day variability of the mean GCLLJ in agreement with numerical simulation studies (e.g., Stensrud et al., 1997; Anderson at al., 2000, 2001). Additionally, the present research included extensive analyses of historical upper-air observations and NARR winds, which demonstrated that significant MCSs in the vicinity and upstream of the GCLLJ core region play a noticeable role in the GCLLJ variability. It appears that strong MCSs over the northern GoC coastal plain result in offshore convective outflows (with time scales or the order of ~6hr-12hrs) that directly accelerate the GCLLJ.

The present research investigated the connection of MJO variability in the eastern Pacific to surge event occurrence, synoptic-scale tropical disturbances, and convective activity in the NAM core region. MJO active and inactive phases were identified using two different indices: an OLR-based index and a 200 hPa velocity potential (CHI200)-based index. Previous studies (e.g, Lorenz and Hartmann, 2006) suggested that enhanced rainfall over the NAM region during MJO events may results from processes that lead to an increase in surge activity. The present research confirmed that the surge frequency varies as a function of the MJO activity. For example, it was shown that surge frequency increases by nearly 50% and 120% after the MJO CHI200- and OLR-based active phase, respectively. Using the same analysis method, it was confirmed that the MJO active phase is related to an increase in TS/TC frequency (in agreement with other authors), while the MJO active or inactive phase appears unrelated to any significant change in TEW activity. Although a precise physical explanation of these linkages requires further research, the succession of events suggests that 2-3 weeks predictability associated with the MJO (Wheeler and Weickmann, 2001) potentially may be extended to the NAMS. Confirmation of this association will require a better understanding of the moisture surge phenomenon and other NAMS components involved in the synoptic-to-intraseasonal variability of the NAMS.

Chapter 5

The observation-based results in Chapters 3 and 4 variously documented that MCSs have significant impact on diurnal and day-to-day variability within the NAM core region. These findings prompted the documentation of the sensitivity of limited area models to the occurrence of convective processes in the NAM core region. This modeling effort provided enhanced insight into the multiscale interactions that occur in the NAMS core domain and the ability of ARW model to reproduce some of the associations mentioned in Chapters 3 and 4.

In various experiments, cold bubbles (CBs) were inserted, at different times during the simulations runs, for two different synoptic environments: surge and non-surge cases. This approach mimicked convective outflow effects of “significant convective events” and their idealized responses to synoptic and diurnal processes. The simulation results highlighted the important role of convective activity over the GoC entrance and over the GoC coastal plain. Specifically, the results showed that CBs over the GoC entrance enhanced the effect of the simulated surge. And that the GCLLJ intensity was significantly modulated by changing the timing of when the convective outflows were applied. For example, daytime CBs over the central GoC coastal plain strengthened the northern GoC low-level flow regardless of the synoptic environment prevailing in the region. These results support the features highlighted in Chapter 3 and are consistent with the observational composites shown in Chapter 4.

Suggestions for future work

Ultimately, the general public should benefit from the present research through better forecasts from regional climate modeling activities. Improved understanding of the relationships between the diurnal cycle, moisture surges, and rainfall over the U.S. southwest also may help public perception and understanding of the climate and weather of "the monsoon". The scientific community will benefit from the improved awareness of the importance of the long-record of GOES imagery for climate research, and the importance of simple in-situ measurements for validation studies. However, there remain several areas in which further research is required.

NAME observations could be further exploited to analyze the influence of MCSs on the low-level flow over the GoC during various NAME IOPs. Several aircraft flights (Mejia and Douglas, 2005) captured remnant convective outflows associated with decaying MCSs over the GoC coastal plains (flight missions of July 22, 23, 24). Aircraft data could be combined with wind profiler, surface station, pibal, and rawinsonde data to analyze the impact of convective outflows during these days, which also coincide with a GCLLJ episode. One more GCLLJ flight (July 23) and one surge genesis flight (August 3) should be analyzed using the same level of detail as already carried out here for the flights described in Chapter 3.

The present research constitutes a benchmark for numerical simulations, since it has been shown that the effect of mesoscale convection has an impact on the regional low-level flow. Thus, all aspects associated with the correct simulation of MCSs (their timing and intensity) and their potential for upscaling impact on the monsoonal flow must be carefully addressed in the future. To improve the physical understanding and the analysis of the simulation results, such work should include more case studies, a better representation of convective outflows, and a methodology to accounting for the upscale effect into the background flow. For example, as mentioned in Chapter 5, idealized rainfall events could be simulated by forcing the triggering function in the convective parameterization schemes. Furthermore, a sensitivity analysis of the effect that convective outflows have on the GoC marine boundary layer is desirable and may provide physical understanding of the triggering mechanisms associated with a surge's initial stages and its propagation characteristics. Finally, a sensitivity analysis involving idealized processes related to other physical schemes (e.g., PBL, radiation, and land surface) may incraese insight in to the physical processes involved.

7 REFERENCES

Adams, D.K., and A.C. Comrie, 1997: The North American Monsoon. *Bull. Amer. Meteor. Soc.*, **78**, 2197–2213.

Adams, J.L., and D.J. Stensrud, 2007: Impact of Tropical Easterly Waves on the North American Monsoon. *J. Climate*, **20**, 1219-1238.

Anderson, B.T., J.O. Roads, and S.-C. Chen, 2000a: Large-scale Forcing of Summertime Monsoon Surges over the Gulf of California and Southwestern United States. *J. Geophys. Res.*, **105**, 24455–24467.

Anderson, B. T., J.O. Roads, S.-C. Chen, and H.-M. H. Juang, 2000b: Regional Simulation of the Low-level Monsoon Winds over the Gulf of California and Southwestern United States. *J. Geophys. Res.*, **105**, 17955–17969.

Anderson, B.T., J.O. Roads, S.-C. Chen, and H.-M. H. Juang, 2001: Model Dynamics of Summertime Low-level Jets over Northwestern Mexico. *J. Geophys. Res.*, **106**, 3401–3412.

Barlow, M., and D. Salstein (2006), Summertime Influence of the Madden-Julian Oscillation on Daily Rainfall over Mexico and Central America, *Geophys. Res. Lett.*, **33**, L21708, doi:10.1029/2006GL027738.

Barnston, A.G. and Livezey R.E., 1987: Classification, Seasonality, and Persistence of Low-frequency Atmospheric Circulation Patterns. *Mon. Wea. Rev.*, **115**, 1083–1126.

Barrett, B. and L.M. Leslie: 2008: Links Between Tropical Cyclone Activity and Madden-Julian Oscillation Phase in the North Atlantic and Northeast Pacific Basins, Accepted to *Monthly Weather Review*.

Berbery, E.H., 2001: Mesoscale Moisture Analysis of the North American Monsoon. *J. Climate*, **14**, 121–137.

Berg, W. K., D.M. Anderson, and J.J. Bates, 2000: Satellite observations of a Pacific moisture surge associated with flooding in Las Vegas. *Geophys. Res. Lett.*, **27**, 2553–2556.

Bister, M., and K.A. Emanuel, 1997: The Genesis of Hurricane Guillermo: TEXMEX Analyses and a Modeling Study. *Mon. Wea. Rev.*, **125**, 2662-2682.

Bordoni, S. and B. Stevens, 2006: Principal Component Analysis of the Summertime Winds over the Gulf of California: A Gulf Surge Index. *Mon. Wea. Rev.*, **134**, 3395-3414.

Brenner, I.S., 1974: A Surge of Maritime Tropical Air—Gulf of California to the Southwestern United States. *Mon. Wea. Rev.*, **102**, 375–389.

Carleton, A.M., D.A. Carpenter, and P.J. Weser, 1990: Mechanisms of Interannual Variability of the Southwest United States Summer Rainfall Maximum. *J. Climate*, **3**, 999–1015.

Castro, C.L., T.B. McKee, and R.A. Pielke, 2001: The Relationship of the North American Monsoon to Tropical and North Pacific Sea Surface Temperatures as Revealed by Observational Analyses. *J. Climate*, **14**, 4449–4473.

Chakraborty, A. and T.N. Krishnamurti, 2003: Numerical Simulation of the North American Monsoon System, *Meteorology and Atmospheric Physics*, **84**, 57-82.

Chelton, D.B., M.H. Freilich, J.M. Sienkiewicz, and J.M. Von Ahn, 2006: On the Use of QuikSCAT Scatterometer Measurements of Surface Winds for Marine Weather Prediction. *Mon. Wea. Rev.*, **134**, 2055–2071.

Christie, D.R., 1989: Long Nonlinear Waves in the Lower Atmosphere. *J. Atmos. Sci.*, **46**, 1462–1491.

Christie, D.R., K.J. Muirhead, and A.L. Hales, 1979: Intrusive Density Flows in the Lower Troposphere: A Source of Atmospheric Solitons. *J. Geophys. Res.*, **84**, 4959–4970.

Chu, Roland, 1994: Algorithms for the Automated Surface Observing System (ASOS). *ISL Office Note 94-4, NWS/OSD*, 106pp.

Done, J., C. Davis, and M. Weisman, 2003: The Next Generation of NWP: Explicit Forecasts of Convection Using Weather Research and Forecasting (WRF) Model. *Atmos. Sci. Lett.* , DOI: 10.1002/asl.72.

Douglas, M.W., 1995: The Summertime Low-level Jet over the Gulf of California. *Mon. Wea. Rev.*, **123**, 2334–2347.

Douglas, M.W., A. Valdez-Manzanilla, and R.G. Cueto, 1998: Diurnal Variation and Horizontal Extent of the Low-level Jet over the Northern Gulf of California. *Mon. Wea. Rev.*, **126**, 2017–2025.

Douglas, M.W. and Leal J.C., 2003: Summertime Surges over the Gulf of California: Aspects of Their Climatology, Mean Structure, and Evolution from Radiosonde, NCEP Reanalysis, and Rainfall Data. *Wea. Forecasting*, **18** (1), 55–74.

Douglas, M.W., R.A. Maddox, and K. Howard, 1993: The Mexican Monsoon. *J. Climate*, **6**, 1665-1677.

Elsberry, R.L., W.M. Frank, G.J. Holland, J.D. Jarrell and R.L. Southern, 1987: A Global View of Tropical Cyclones. *Univ. of Chicago Press, Chicago, IL*. 192 pp.

Farfán, L.M., and J.A. Zehnder, 1994: Moving and Stationary Mesoscale Convective Systems over Northwest Mexico during the Southwest Area Monsoon Project. *Wea. Forecasting*, **9**, 630–639.

Fawcett, P.J., J.R. Stalker, and D.S. Gutlzer, 2002, Multistage Moisture Transport into the Interior of Northern Mexico during the North American Summer Monsoon, *Geophys. Res. Lett.*, **29**, 2094

Feldstein S.B., 2007: The Dynamics of the North Atlantic Oscillation during the Summer Season, *Q. J. R. Meteorol. Soc.*, **133**, 1509–1518, DOI: 10.1002/qj.107.

Fuller, R.D., and D.J. Stensrud, 2000: The Relationship Between Easterly Waves and Surges over the Gulf of California during the North American Monsoon. *Mon. Wea. Rev.*, **128**, 2983–2989.

Gill, A.E., 1982: Atmosphere-Ocean Dynamics. *Academic Press, New York*, 664 pp.

Gill, A.E., 1977: Coastally-Trapped Waves in the Atmosphere, *Quart. J. Roy. Meteor. Soc.*, **103**, 431-440.

Gochis, D.J., W. J. Shuttleworth, and Z.-L. Yang, 2002: Sensitivity of Modeled North American Monsoonal Regional Climate to Convective Parameterization. *Mon. Wea. Rev.*, **130**, 1282–1298.

Gochis, D.G., A. Jimenez, C.J. Watts, J. Garatuza-Payan, and W.J. Shuttleworth, 2004: Analysis of 2002 and 2003 Warm-Season Precipitation from the North American Monsoon Experiment Event Rain Gauge Network. *Mon. Wea. Rev.* **132**, 2938-2953

Gutzler, DS, Kim HK, Higgins RW, Juang HMH, Kanamitsu M, et al., 2005: The North American Monsoon Model Assessment Project: Integrating Numerical Modeling into a Field-based Process Study. *Bull. Amer. Meteor. Soc.,* **86**, 1423–1429.

Haertel, P.T., R.H. Johnson, S.N. Tulich, 2001: Some Simple Simulations of Thunderstorm Outflows. *J. Atmos. Sci.*, **58**, 504-516.

Hales, J.E., 1972: Surges of Maritime Tropical Air Northward over the Gulf of California. *Mon. Wea. Rev.*, **100**, 298–306.

Hawkins, Timothy W., Ellis, Andrew W., Skindlov, Jon A., Reigle, Dallas, 2002: Intra-annual Analysis of the North American Snow Cover–Monsoon Teleconnection: Seasonal Forecasting Utility, *J. Climate*, **15**, 1743-1753.

Higgins, R.W., and W. Shi, 2001: Intercomparison of the Principal Modes of Interannual and Intraseasonal Variability of the North American Monsoon System. *J. Climate*, **14**, 403–417.

Higgins, R.W. and W. Shi, 2005: Relationships between Gulf of California Moisture Surges and Tropical Cyclones in the Eastern Pacific Basin. *J. Climate*, **18**, 4601–4620.

Higgins, R.W., K.C. Mo, and Y. Yao, 1998: Interannual Variability of the U.S. Summer Precipitation Regime with Emphasis on the Southwestern Monsoon. *J. Climate*, **11**, 2582–2606.

Higgins, R.W., Shi W, and Hain C, 2004: Relationships Between Gulf of California Moisture Surges and Precipitation in the Southwestern United States. *J. Climate,* **17**, 2983–2997.

Higgins, R. W. and D. J. Gochis, 2006: Multi-scale Interactions During the North American Monsoon, *Symposium on Connections Between Mesoscale Processes and Climate Variability, AMS 87th annual meeting.*

Higgins, R.W., Y. Yao, E.S. Yarosh, J.E. Janowiak, and K.C. Mo, 1997: Influence of the Great Plains Low-level Jet on Summertime Precipitation and Moisture Transport over the Central United States. *J. Climate*, **10**, 481–507.

Higgins, R.W., D. Ahijevych, J. Amador, A. Barros, E.H. Berbery, E. Caetano, R. Carbone, P. Ciesielski, R. Cifelli, M. Cortez-Vazquez, A. Douglas, M. Douglas, G. Emmanuel, C. Fairall, D. Gochis, D. Gutzler, T. Jackson, R. Johnson, C. King, T. Lang, M.I. Lee, D. Lettenmaier, R. Lobato, V. Magaña, J. Meiten, K. Mo, S. Nesbitt, F. Ocampo-Torres, E. Pytlak, P. Rogers, S. Rutledge, J. Schemm, S. Schubert, A. White, C. Williams, A. Wood, R. Zamora, and C. Zhang, 2006: The NAME 2004 Field Campaign and Modeling Strategy. *Bull. Amer. Meteor. Soc.*, **87**, 79–94.

Hoffman, R.N., and S.M. Leidner, 2005: An Introduction to the Near–Real–Time QuikSCAT Data. *Wea. Forecasting*, **20**, 476–493.

Hong, S.Y., Y. Noh, and J. Dudhia, 2006: A New Vertical Diffusion Package with an Explicit Treatment of Entrainment Processes. *Mon. Wea. Rev.*, **134**, 2318–2341.

Janjic, Z.I., J.P. Gerrity, and S. Nickovic, 2001: An Alternative Approach to Nonhydrostatic Modeling. *Mon. Wea. Rev.*, **129**, 1164–1178.

Jankov, I., W.A. Gallus, M. Segal, B. Shaw, and S.E. Koch, 2005: The Impact of Different WRF Model Physical Parameterizations and Their Interactions on Warm Season MCS Rainfall. *Wea. Forecasting*, **20**, 1048–1060.

Jirak, I.L., and W.R. Cotton, 2007: Observational Analysis of the Predictability of Mesoscale Convective Systems. *Wea. Forecasting*, **22**, 813–838.

Johnson, R.H., 2001: Surface Mesohighs and Mesolows. *Bull. Amer. Meteor. Soc.*, **82**, 13–31.

Johnson, R.H., S. Chen, and J.J. Toth, 1989: Circulations Associated with a Mature-to-Decaying Midlatitude Mesoscale Convective System. Part I: Surface Features—Heat Bursts and Mesolow Development. *Mon. Wea. Rev.*, **117**, 942–959.

Klemp, J. B., R. Rotunno, and W. C. Skamarock, 1994: On the Dynamics of Gravity Currents in a Channel. *J. Fluid Mech.*, **269**, 169–198.

Klemp, J. B., R. Rotunno, and W. C. Skamarock, 1997: On the Propagation of Internal Bores. *J. Fluid Mech.*, **331**, 81–106.

Knapp, K. R., 2008: Scientific Data Stewardship of International Satellite Cloud Climatology Project B1 global geostationary observations. *Journal of Applied Remote Sensing*, **2**, 023548, doi:10.1117/1.3043461.

Knievel, J.C., and R.H. Johnson, 1998: Pressure Transients within MCS Mesohighs and Wake Lows. *Mon. Wea. Rev.*, **126**, 1907–1930.

Knopfmeier, Kent H., R. J. Trapp, and D. M. Wheatley, 2006: Real-data and Idealized Simulations of the 4 July 2004 Bow Echo Event, *23rd Conference on Severe Local Storms, November.*

Knupp, K., 2006: Observational Analysis of a Gust Front to Bore to Solitary Wave Transition within an Evolving Nocturnal Boundary Layer. *J. Atmos. Sci.*, **63**, 2016–2035.

Koch, S.E., and W.L. Clark, 1999: A nonclassical Cold Front Observed during COPS-91: Frontal Structure and the Process of Severe Storm Initiation. *J. Atmos. Sci.*, **56**, 2862–2890.

Koch, S.E., M. Pagowski, J. W. Wilson, F. Fabry, C. Flamant, W. Feltz, G. K. Schwemmer, and B. Geerts, 2005: The Structure and Dynamics of Atmospheric Bores and Solitons as Determined from Remote Sensing and Modeling Experiments during IHOP, *11th Conference on Mesoscale Processes and 32nd Conference on Radar Meteorology. October.*

Koch, S.E., P.B. Dorian, R. Ferrare, S. Melfi, W.C. Skillman, and D. Whiteman, 1991: Structure of an Internal Bore and Dissipating Gravity Current as Revealed by Raman Lidar. *Mon. Wea. Rev.*, **119**, 857–887.

Krishnamurti, T., 1971: Tropical East-West Circulations During the Northern Summer. *J. Atmos. Sci.*, **28**, 1342–1347.

Krishnamurti, T., M. Subramaniam, G. Daughenbaugh, D. Oosterhof, and J. Xue, 1992: One-Month Forecasts of Wet and Dry Spells of the Monsoon. *Mon. Wea. Rev.*, **120**, 1191–1223.

Lau, K.M. and Weng H., 2002: Recurrent Teleconnection Patterns Linking Summertime Precipitation Variability over East Asia and North America, *J. of the Met. Soc. of Japan*, **80** (6), 1309-1324.

Leathers, D.J., and M.A. Palecki, 1992: The Pacific/North American Teleconnection Pattern and United States Climate. Part II: Temporal Characteristics and Index Specification. *J. Climate*, **5**, 707–716.

Li, J., X. Gao, K. L. Hsu, B. Imam, and S. Sorooshian, 2006: Modeling Rainfall Diurnal Variation of the North American Monsoon Core Using Different Spatial Resolutions, *27th conference on hurricanes and tropical meteorology, AMS, Monterey, California, April.*

Liebmann, B. and C.A. Smith, 1996: Description of a Complete (Interpolated) Outgoing Longwave Radiation Dataset. *Bull. Amer. Meteor. Soc.*, **77**, 1275-1277. Data available online: http://www.cdc.noaa.gov/ cdc/data.interp_OLR.html.

Livezey, R. E., and T. M. Smith, 1999: Covariability of Aspects of North American Climate with Global Sea Surface Temperatures on Interannual to Interdecadal Timescales. *J. Climate,* **12,** 289–302.

Lo, Fiona, Clark, Martyn P, 2002: Relationships between Spring Snow Mass and Summer Precipitation in the Southwestern United States Associated with the North American Monsoon System, *J. Climate*, **15**, 1378-1385.

Lorenz, D.J., and D.L. Hartmann, 2006: The Effect of the MJO on the North American Monsoon. *J. Climate*, **19**, 333–343.

Machado, L. A. T. , Rossow, W. B., R. L. Guedes and A. Walker, 1998: Life Cycle Variations of Convective Systems over the Americas. *Mon. Wea. Rev.*, **126**, 1630-1654.

Madden, R. A., and P. R. Julian, 1971: Detection of a 40-50 day Oscillation in the Zonal Wind in the Tropical Pacific. *J. Atmos. Sci.*, **28**, 702-708.

Madden, R. A., and P. R. Julian, 1994: Observations of the 40–50-Day Tropical Oscillation—a Review. *Mon. Wea. Rev.*, **122**, 814–837.

Maddox, R. A., 1980: Mesoscale Convective Complexes. *Bull. Amer. Meteor. Soc.*, **61**, 1374-1387.

Magaña, V., J.A. Amador, and S. Medina, 1999: The Midsummer Drought over Mexico and Central America. *J. Climate*,**12**, 1577–1588.

Maloney, E.D., and D.L. Hartmann, 2000: Modulation of Eastern North Pacific Hurricanes by the Madden–Julian Oscillation. *J. Climate*, **13**, 1451–1460.

Maloney, E.D., and D.L. Hartmann, 2000: Modulation of Eastern North Pacific Hurricanes by the Madden–Julian Oscillation. *J. Climate*, **13**, 1451–1460.

Mass, C.F., and M.D. Albright, 1987: Coastal Southerlies and Alongshore Surges of the West Coast of North America: Evidence of Mesoscale Topographically Trapped Response to Synoptic Forcing. *Mon. Wea. Rev.*, **115**, 1707–1738.

Matsui, T., V. Lakshmi, and E. Small, 2003: Links between Snow Cover, Surface Skin Temperature, and Rainfall Variability in the North American Monsoon System. *J. Climate*, **16**, 1821–1829.

McCollum, D.M., R.A. Maddox, and K.W. Howard, 1995: Case Study of a Severe Mesoscale Convective System in Central Arizona. *Wea. Forecasting*, **10**, 643–665.

Meitin, J., 2001: The Southwest Area Monsoon Project: Daily operations plan, *NSSL/NOAA, Bouldar, CO*, 75pp.

Mejia, J.F. and M.W. Douglas, 2005: Mean Structure and Variability of the Low-level Jet across the Central Gulf of California from NOAA WP-3D Flight Level Observations during the North American Monsoon Experiment, *Sixth Conference on Coastal Atmospheric and Oceanic Prediction and Processes (6COASTAL), 85th AMS Annual Meeting, San Diego, CA*, J5.8.

Mesinger, F, DiMego G, Kalnay E, Mitchell K, Shafran PC, et al., 2006: North American Regional Reanalysis. *Bull. Amer. Meteor. Soc.*, ***87***, 343–360.

Misra, V., 2008: Coupled Interactions of the Monsoons, *Geophys. Res. Lett.*, **35**, L12705, doi:10.1029/2008GL033562.

Mo, K.C., Chelliah M., Carrera M.L., Higgins R.W, and Ebisuzaki W., 2005: Atmospheric Moisture Transport over the United States and Mexico as Evaluated in the NCEP Regional Reanalysis, *J. Hydromet,* **6**, 710–728.

Mo, K.C., and E. H. Berbery, 2004: Low-level Jets and the Summer Precipitation Regimes over North America. *J. Geophys. Res.*, **105**, doi:10.1029/2003JD004106.

Molinary, and D. Vollaro, 2000: Planetary and Synoptic Scale Influences on Eastern Pacific Tropical Cyclogenesis. *Mon. Wea. Rev.*, **128**, 3296-3307.

Parish, T.R., 2000: Forcing of the Summertime Low-Level Jet along the California Coast. *J. Appl. Meteor.*, **39**, 2421–2433.

Ralph, F.M., L. Armi, J.M. Bane, C. Dorman, W.D. Neff, P.J. Neiman, W. Nuss, and P.O.G. Persson, 1998: Observations and Analysis of the 10–11 June 1994 Coastally Trapped Disturbance. *Mon. Wea. Rev.*, **126**, 2435–2465.

Ralph, F.M., P.J. Neiman, P.O.G. Persson, J.M. Bane, M.L. Cancillo, J.M. Wilczak, and W. Nuss, 2000: Kelvin Waves and Internal Bores in the Marine Boundary Layer Inversion and Their Relationship to Coastally Trapped Wind Reversals. *Mon. Wea. Rev.*, **128**, 283–300.

Reason, C.J.C., and D.G. Steyn, 1992: The Dynamics of Coastally Trapped Mesoscale Ridges in the Lower Atmosphere. *J. Atmos. Sci.*, **49**, 1677–1692.

Reid, H.J., and L.M. Leslie, 1999: Modeling Coastally Trapped Wind Surges over Southeastern Australia. Part I: Timing and Speed of Propagation. *Wea. Forecasting*, **14**, 53–66.

Reyes, S., M.W. Douglas, and R.A. Maddox, 1994: El Monzón del Suroeste de Norteamérica (TRAVASON/SWAMP). *Atmósfera*, **7**, 117–137.

Richman, M.B., 1986: Rotation of Principal Components. *J. Climatol*, **6**, 293–335.

Rogers, P.J., and R.H. Johnson, 2007: Analysis of the 13–14 July Gulf Surge Event during the 2004 North American Monsoon Experiment. *Mon. Wea. Rev.*, **135**, 3098–3117.

Schmitz, J.T., and S. L. Mullen, 1996: Water Vapor Transport Associated with the Summertime North American Monsoon as Depicted by ECMWF Analyses. *J. Climate*, **9**, 1621–1634.

Schreffler, J.H. and Binowski, F. S. 1981 Observations of Pressure Jump Lines in the Midwest, 10-12 August 1976. *Mon. Wea. Rew.* **109**, 1713-1725.

Simpson, J.E., 1987*:* Gravity Currents: In the Environment and the Laboratory. *John Wiley & Sons*, 244 pp.

Skamarock, W.C., J.B. Klemp, J. Dudhia, D.O. Gill, D.M. Barker, W. Wang and J. G. Powers, 2005: A Description of the Advanced Research WRF Version 2. *NCAR technical note*, NCAR/TN-468+STR.

Stensrud, D.J., R.L. Gall, and M.K. Nordquist, 1997: Surges over the Gulf of California during the Mexico Monsoon. *Mon. Wea. Rev.*, **125**, 417–437.

Stensrud, D.J., R.L. Gall, S.L. Mullen, and K.W. Howard, 1995: Model Climatology of the Mexico Monsoon. *J. Climate*, **8**, 1775–1794.

Stensrud, D.J., J.W. Bao, and T.T. Warner, 2000: Using Initial Condition and Model Physics Perturbations in Short-Range Ensemble Simulations of Mesoscale Convective Systems. *Mon. Wea. Rev.*, **128**, 2077–2107.

Straka, J.M., R.B. Wilhelmson, L.J. Wicker, J.R. Anderson, and K. K. Droegemeier, 1993: Numerical Solutions of a Non-linear Density Current: a Benchmark Solution and Comparisons. *Int. J. Numer. Meth. Fluids*, **17**, 1–22.

Tan, Z., and R. Wu, 1993: The Ekman Momentum Approximation and its Application. *Bound.-Layer Meteor.,* **68**, 193–199.

Tang, M., and E.R. Reiter, 1984: Plateau Monsoons of the Northern Hemisphere: A Comparison between North America and Tibet. *Mon. Wea. Rev.*, **112**, 617–637.

Von Karman, T. 1940: The Engineer Grapples with Nonlinear Problems, *Bull. Amer. Mathematical. Soc.* **46**, 615-683.

Wallace, C.E., R.A. Maddox, and K.W. Howard, 1999: Summertime Convective Storm Environments in Central Arizona: Local Observations. *Wea. Forecasting*, **14**, 994–1006.

Wang ,W., and N.L. Seaman, 1997: A comparison study of convective parameterization schemes in a mesoscale model. *Mon. Wea. Rev.*,**125**, 252–278.

Wheeler, M., and K. M. Weickmann, 2001: Real-time Monitoring and Prediction of Modes of Coherent Synoptic to Intraseasonal Tropical Variability. *Mon. Wea. Rev.*, **129**, 2677–2694.

Xue, Y, R. W. Higgins, H.-K. Kim and V. Kousky, 2002: Impacts of the Madden Julian Oscillation on U.S. Temperature and Precipitation during ENSO-Neutral and Weak ENSO Winters. *26th Climate Diagnostics and Prediction Workshop*, Amer. Meteor. Soc.

Zehnder J. A., 2004: Dynamic Mechanisms of the Gulf Surge. *J. Geophys. Res.*, **109**, D10107, doi:10.1029/2004JD004616.

Zhang, D.L. and Bao N., 1996: Oceanic Cyclogenesis as Induced by a Mesoscale Convective System Moving Offshore. Part I: A 90-h Real-Data Simulation. *Mon. Wea. Rev.* **124**. 1449–1469.

Zhang, D.L., and J. Fritsch, 1988: A Numerical Investigation of a Convectively Generated, Inertially Stable, Extratropical Warm-Core Mesovortex over Land. Part I: Structure and Evolution. *Mon. Wea. Rev.*, **116**, 2660–2687.

Zhu, C.M., Lettenmaier D.P., T. Cavazos, 2005. Role of Antecedent Land Surface Conditions on North American Monsoon Rainfall Variability. *J. Climate*. **18**, 3104–3121.